KU LEUVEN

ARENBERG DOCTORAL SCHOOL
Faculty of Science

^{32}Ar decay, a search for exotic current contributions in weak interactions

The WISArD Experiment

Victoria Isabel Araujo-Escalona

Supervisors:
Prof. dr. Nathal Severijns
Prof. dr. Bertram Blank
(CENBG, France)

Dissertation presented in partial fulfillment of the requirements for the degree of Doctor of Science (PhD): Physics

June 2021

^{32}Ar decay, a search for exotic current contributions in weak interactions

The WISArD Experiment

Victoria Isabel ARAUJO-ESCALONA

Examination committee:
Prof. dr. Michel Houssa, chair
Prof. dr. Nathal Severijns, supervisor
Prof. dr. Bertram Blank, supervisor
(CENBG, France)
Prof. dr. Riccardo Raabe
Prof. dr. Gerda Neyens
Prof. dr. Libertad Barrón Palos
(IF, UNAM)
Prof. dr. Oscar Naviliat Cuncic
(LPC, Caen)
Prof. dr. Alejandro Garcia
(University of Washington, USA)

Dissertation presented in partial fulfillment of the requirements for the degree of Doctor of Science (PhD): Physics

June 2021

Uitgegeven in eigen beheer, Victoria Isabel Araujo-Escalona, Celestijnenlaan 200B, B-3001 Leuven (Belgium)

Acknowledgement

During the last 4-years of my trajectory I met many people to whom I feel grateful. First and foremost, I am extremely grateful to my supervisors Professors Nathal Severijns and Bertram Blank for their invaluable advice, continuous support, and patience during my PhD study. I got lucky to learn from the perfect duo in nuclear physics for their immense knowledge and experience in both theoretical and experimental aspects. Prof. Nathal Severijns, you gave me many tools and passionate talks about why it is important to continue testing the Standard Model and Prof. Bertram Blank your expertise in the experimental area not just encouraged me in my academic research, but also in my daily life, a truly and deeply thank you to you both.

A big shout out to Vladimir Manea and Zhengyu Xu, who not only offered me their friendship but also their knowledge and their free time to answer my innumerable questions. Thank you to Lukas Nies, who was my first summer student at ISOLDE, since day one not only showed to be a good student but also an excellent person, thank you, boss!

I would like to thank all the members of the WISArD team, in particular, Phillipe Alfaurt and Laurent Daudin for their technical support on my study and for making the work more fun during the WISArD Working Weeks. To Xavier Fléchard for his always kind help and support in the data analysis procedure. Last but not least, a huge thank you to Dinko Atanasov.

A big thanks to Isabelle Boesmann and Fabienne Vanalphen who, from Leuven, always kept me up to date with all the administrative procedures. Simon Vanlangendonck, Lennert De Keukeleere and Leendert Hayen, my favorite Belgian squad! thank you for making me feel like part of the team the times that I spent at the IKS Leuven. My gratitude extends to the Centre d'Etudies Nucleaires de Bordeaux Gradignan (CENBG) who warmly welcomed me as one of them during my last year as a PhD.

My deep appreciation also goes out to my family in México that despite the distance and different time-zones, they always stayed by my side cheering me on and encourage me through my studies. In this family, I include my former supervisor Efraín Chávez, thank you very much for keeping your trust in me and in my abilities. A big thank my friends: Paris, Romana, Patrycja, they may never read my thesis, but I highly appreciate every second that they heard me talk about it without much knowing what I was saying. To Hanne Heylen, Juliana Schell, Chris Richardson, Tassos, Fredrik PG, Liss Vazquez, Jonas K., Robin Engel, and the "précaires CENBG" group (specially to Audric, Guillaume, Vincent, Antoine, and Marjut), for a cherished time we spent together in the lab, coffee-times, and in social settings.

Abstract (English)

It has been proven that high precision (such as $< 10^{-3}$) measurements in the low energy regime (few of MeV) are promising tools in the search of non-Standard-Model contributions. Among the available experimental nuclear observables, the angular correlation coefficient between the beta particle and (anti)neutrino in beta decay, $\tilde{a}_{\beta\nu}$, is a sensitive probe to search for exotic scalar type interaction terms in the electro-weak sector of the Standard Model.

A new approach based on measurements of the kinematic proton energy shift is carried out by the WISArD (**W**eak **I**nteraction **S**tudies with ^{32}**Ar** **D**ecay) project at ISOLDE/CERN carriage return. We focused on the superallowed $0^+ \rightarrow 0^+$ Fermi transition of the ^{32}Ar beta decay to a state in ^{32}Cl, which is unbound to proton emission. The results yielded a $\tilde{a}_F = 1.000 \pm 0.037_{stat} \pm 0.027_{sys}$.

In the current work, I extended the analysis to five proton lines following an allowed Gamow-Teller transition. Even though the limits on exotic tensor contributions were not restrictive, it remains useful to check systematic errors and cross-check the analysis for the superallowed Fermi transition. The result for one of the five Gamow-Teller transitions excels with respect to the others, i.e., the protons peak at 2121 keV, giving $\tilde{a}_{GT} = -0.338 \pm 0.066_{stat} \pm 0.033_{sys}$.

Both results are consistent with a pure Vector-Axial vector interaction assuming right-handed neutrinos, $C_i = -C_i'$. Despite the short beamtime allocated for this test, the collected data provides the third most precise measurement of $\tilde{a}_{\beta\nu}$ in a pure Fermi transition.

The uncertainty quoted for the Fermi and Gamow-Teller transition represents a careful evaluation of the systematic effects contributing to the uncertainty.

According to a careful GEANT4 simulation analysis of both statistical and systematic uncertainties, the use of a dedicated detection setup, a thinner mylar thickness for the source foil, and a full characterization of the positron detector allow for a precision measurement of the order of 2×10^{-3} of the $\tilde{a}_{\beta\nu}$ in the pure Fermi transition of the ^{32}Ar decay. The improved result will reduce significantly the present constraints on exotic currents of the weak interaction inferred from existing angular correlation measurements in nuclear beta decay.

Abstract (Dutch)

Metingen met hoge precisie (<10^{-3}) bij lagere energiëen (enkele MeV) zijn veelbelovende hulpmiddelen bij het zoeken naar bijdragen buiten het Standaard Model voor de fundamentele deeltjes en hun interacties. Eén van de geschikte experimentele nucleaire observabelen is de correlatiecoëfficiënt tussen het bètadeeltje en het (anti)neutrino in dit verval, $\tilde{a}_{\beta\nu}$. Deze correlatiecoëfficiënt is gevoelig aan exotische scalaire interactietermen in de elektrozwakke sector van het Standaard Model.

Een nieuwe benadering gebaseerd op metingen van de energieverschuiving van de protonen wordt uitgevoerd door het WISArD (**W**eak **I**nteraction **S**tudies with ^{32}**Ar D**ecay) project in ISOLDE/CERN.

We hebben ons geconcentreerd op het supertoegelaten (superallowed) 0+ → 0+ overgang van ^{32}Ar naar een toestand in ^{32}Cl die ongebonden is ten opzichte van protonemissie. De resultaten leveren $\tilde{a}_F = 1.000 \pm 0.037_{stat} \pm 0.027_{sys}$ op.

In het huidige werk heb ik de analyse uitgebreid met vijf protonlijnen volgend op een toegelaten Gamow-Teller-overgang. Hoewel de grenzen op de exotische tensorbijdragen niet verbeterd werden, bleek de analyse zeer nuttig om systematische fouten te controleren en zo de analyse voor de supertoegelaten Fermi overgang te valideren. Eén van de vijf Gamow-Teller-overgangen blinkt daarbij uit, namelijk de protonenpiek bij 2121 keV, met $\tilde{a}_{GT} = -0.338 \pm 0.066_{stat} \pm 0.033_{sys}$.

Beide resultaten zijn consistent met een zuivere Vector-Axiale vectorinteractie uitgaande van rechtshandige neutrino's, $C_i = -C_i{}'$. Ondanks de korte experimentele periode die voor deze test werd uitgetrokken, leveren de verzamelde gegevens de op twee na nauwkeurigste meting van $\tilde{a}_{\beta\nu}$ in een zuivere Fermi-overgang op.

In beide waarden werd de onzekerheid bekomen door middel van een zorgvuldige evaluatie van de systematische effecten die bijdragen tot de onzekerheid. Een zorgvuldige analyse van zowel de statistische als de systematische onzekerheid voorspelt dat, mits het gebruik van een speciale detectieopstelling, een dunnere mylar-dikte voor de bronfolie en een volledige karakterisering van de positronendetector, een nauwkeurigheid in de grootteorde van 2x10^{-3} voor $\tilde{a}_{\beta\nu}$ in de zuivere Fermi-overgang van ^{32}Ar mogelijk is. Dit nieuwe resultaat zou de huidige beperkingen op exotische stromen van de zwakke wisselwerking, afgeleid uit de bestaande correlatiemetingen in nucleair verval, aanzienlijk verminderen.

Content

Introduction

The main idea of many current experiments in the framework of the Standard electroweak Model (SM) is to lead us to an accurate description of this model. Even after the celebrated discovery of the Higgs boson, there remain unanswered questions like for instance: the origin of parity violation, the weak interaction between leptons and quarks, the origin and the mechanism behind the matter-antimatter asymmetry, including the existence and origin of dark matter. These questions have to be answered within a desired unified SM theory. The SM is a set of quantum theories, describing three out of the four fundamental forces of nature, electromagnetism, strong and weak interaction, using a common basis. The weak force, responsible for radioactive beta decays, has found several of its basic foundations, i.e., maximal parity violation, left-handed neutrino helicity, and Vector - Axial vector character, from the study of nuclear beta decay processes.

How the leptons and quarks interact by the weak force is explained in the SM by exchanging bosons, force-carrying particles, the properties of which are determined by the gauge-symmetry. There are two main experimental approaches to test the SM formalism: one is to perform collider experiments at very high energies; the other one relies on low-energy beta-decay experiments with high precision. Results from both energy regimes were confronted, giving us reasons to believe that the SM might still not be a complete theory and motivating scientists to keep performing precise tests of discrete symmetries and search for non-SM physics.

Since 2012, the year of discovery of the Higgs boson, the Large Hadron Collider (LHC) has not produced more evidence of new physics from high energy data. This led to an interest in the search for new and complementary information through high precision measurements at low energy, e.g., correlation measurements.

The WISArD (<u>W</u>eak <u>I</u>nteraction <u>S</u>tudies with ^{32}<u>Ar</u>gon <u>D</u>ecays) experiment took benefit of the recent developments in both detection and data-acquisition techniques and in particular of an existing superconducting magnet from the former WITCH experiment and joined the low energy experiments community pursing a new limit on scalar weak currents via angular correlation measurements with exotic nuclei.

Chapter 1 describes what is called exotic current contributions. We focus on two out of the five possible contributions to the weak interaction, i.e., scalar and tensor currents, how we can obtain information about them, and stress the importance of new precision measurements at low energies.

A brief description of nuclear beta decay observables is presented in chapter 2, with the $\beta - \nu$ angular correlation as the core of our research. Within this chapter, the subsection *state of the art*, summarizes previous experiments on the measurement of the $\beta - \nu$ angular correlation coefficient, $a_{\beta\nu}$, and its sources of systematic uncertainties pointing out the sensitivity required by new experiments aiming to improve the current limits set by those experiments.

Once the theoretical background is set, a complete description of the experimental technique of the WISArD experiment and details related to the proof-of-principle are given in chapter 3.

Chapter 4 describes the experimental setup, that was used for the proof-of-principle experiment, as well as a brief description on how the ^{32}Ar beam is produced and delivered to the WISArD experiment. Then, particular attention is given to the detection and acquisition system, and the importance of the magnetic field is stressed since is an essential part of the WISArD experiment. We conclude with a description of the data collected in the ^{32}Ar campaign at ISOLDE in November 2018 and the analysis of these.

In chapter 5, a detailed description is given of how the energy calibration was performed and of the number of energy corrections have to be implemented to the proton energy spectra before the kinematic energy shifts are obtained. The potential of WISArD to study simultaneously different proton lines is investigated. This chapter ends with the values for the proton energy shift obtained for at least five proton energies apart from the one for the Fermi transition.

Chapter 6 includes the information regarding the Monte Carlo simulations that were not only necessary to determine the final value of the angular correlation coefficient but also to weight the influence of the systematic errors present in the experimental setup.

Finally, conclusions and discussion of the results reported in chapter 6 are formulated in chapter 7.

1
Exotic currents in the Weak Interaction

In place of a unifying theory, there are islands of coherent knowledge in a sea of uncorrelated facts. -D Halliday

The global objective of this work is to search for scalar and tensor current contributions and hence to search for new physics, i.e., non-Standard Model (SM) contributions. But what are these exotic contributions? How do they relate to the standard model? How can each contribution be determined? These and further details of the physics motivation will be addressed in the current chapter.

1.1. The forbidden pleasures in the SM

Two main experimental approaches can lead us to physics beyond the standard model: one is to perform collider experiments at very high energies to find evidence of new particles. At the end of this chapter a brief discussion about this is given. The second one uses low energy experiments, often in beta decay, to determine different aspects of the weak interaction. The latter approach is currently used as a central method to provide high precision tests of the discrete symmetries in the SM and search for non-SM interactions.

The electroweak standard model contains a number of assumptions that were discovered in nuclear beta decay processes, so on the basis of low energy phenomena. Some examples are the nature and helicity-behavior of the neutrino, vector (V) and axial-vector (A) theory and parity-violation (P). The proved existence of the Higgs boson confirmed the SM's consistency along with global fits between experiments and SM-theory predictions. Nevertheless, some important questions within the SM remain unanswered such as the origin of parity violation, the mechanism behind the matter-antimatter asymmetry, the nature of dark matter, etc. [1]. These questions are expected to find explanations by means of non-SM contributions, i.e., New Physics (NP).

Important motivations to perform experiments at low energies with high precision are to search for non-SM interaction components, so-called *exotic currents*, i.e., *scalar (S), tensor (T) and pseudoscalar (P)* contributions, (in addition to the vector (V) and axial-vector (A) contributions that are well established within the SM framework), which are all three forbidden in the present SM, or right-handed currents that require hypothetical new particles heavier than the known $W^{\pm}$ and Z vector bosons.

High-precision experiments at low energy can also test the discrete (time reversal and parity) symmetries of these exotic interactions. Note that the scalar, vector, axial-vector, tensor and pseudoscalar are the five possible current forms that can be present in the weak interaction according to the general principle of Lorentz invariance. Related to each current contribution there are coupling constants C_i' with i = S, V, A, T and P, that weight the strength of each interaction and have to be determined experimentally. To get more details about these coupling constants and thus the nature of the weak interaction, a brief description of the historical evolution of the weak interaction is needed.

1.2. Brief description of weak interaction theory

The first Hamiltonian description of the weak interaction was made by Fermi in 1934 [2]. There, the interaction was expressed as a simple product of the hadronic and leptonic currents. It is known as a four-fermion point interaction (see Fig. 1.1-a). Such an interaction represents the evaluation of the wave function's amplitude of the leptonic particles (electron and neutrino) evaluated at the position of the nucleus, based on the description of the electromagnetic force well known at that time. In this first approach, Fermi concluded that the amplitude should be described by a bilinear combination of the Dirac spinors for electron and neutrino. Since Dirac spinors have four components, there are 16 independent bilinear combinations. Using the properties under Lorentz transformation of these bilinears, they can be divided into five groups.

Table 1. Combinations respecting Lorentz transformations

Bilinear combination	Relativistic transformation
$\bar{\psi}_a\psi_b$	Scalar (S)
$\bar{\psi}_a\gamma^{\mu}\psi_b$	Vector (V)
$\bar{\psi}_a\gamma^{\mu}\gamma^{\nu}\psi_b$	Tensor (T)
$\bar{\psi}_a\gamma^{\mu}\gamma^{\nu}\gamma^{\lambda}\psi_b$	Axial (A)
$\bar{\psi}_a\gamma_5\psi_b$	Pseudoscalar (P)

Using a relativistic approach, Table 1 summarizes these five possible current contributions to the weak interaction respecting Lorentz invariance transformations of the bilinear combinations [3]. Here γ_μ represents the Dirac gamma matrices and ψ_a and ψ_b are Dirac 4-spinors with $\bar{\psi}_a = \psi_a^{\dagger}\gamma^0$. The indexes μ, ν and λ range from 0 to 3 and

$\mu \neq \nu \neq \lambda$ with $\gamma^5 = i\gamma^0\gamma^1\gamma^2\gamma^3$. The Fermi interaction Hamiltonian inspired by the electromagnetic interaction, which is a vector interaction, would look as follows:

$$\mathcal{H} = g_F(\bar{\psi}_p\gamma_\nu\psi_n)(\bar{\psi}_e\gamma^\mu\psi_\nu) + h.c., \quad \textbf{(1.1)}$$

where $\psi_{p,n}$ are the wave functions of the proton (p) and neutron (n), respectively. The Fermi constant, g_F, determines, as an analog to the electric charge, **e**, the strength of the weak interaction. Fermi's first theory description suits for superallowed decays where $\Delta I = 0$ and $\pi_i = \pi_f$. Here ΔI indicates the spin difference between the initial and final nucleus, and $\pi_{i,f}$ denotes the parity for the initial and final states, respectively.

In 1936, Gamow and Teller extended Fermi's Hamiltonian in order to incorporate decays with lepton nuclear spins combined to 1 ($\Delta I = 0, \pm 1$). The detailed form of this Hamiltonian clearly distinguishes the five possible current contributions [2]:

$$\begin{aligned}\mathcal{H} = g_F[&C_s(\bar{\psi}_p\psi_n)(\bar{\psi}_e\psi_\nu) + \\ &C_V(\bar{\psi}_p\gamma_\mu\psi_n)(\bar{\psi}_e\gamma^\mu\psi_\nu) + \\ &\frac{C_T}{2}(\bar{\psi}_p\sigma_{\lambda\mu}\psi_n)(\bar{\psi}_e\sigma^{\lambda\mu}\psi_\nu) - \\ &C_A(\bar{\psi}_p\gamma_\mu\gamma_5\psi_n)(\bar{\psi}_e\gamma^\mu\gamma_5\psi_\nu) + \\ &C_P(\bar{\psi}_p\gamma_5\psi_n)(\bar{\psi}_e\gamma_5\psi_\nu)] + h.c.,\end{aligned} \quad \textbf{(1.2)}$$

with

$$\sigma_{\lambda\mu} = -{}^1/_2\, i(\gamma_\lambda\gamma_\mu - \gamma_\mu\gamma_\lambda)$$

To simplify the notation, equation 1.2 can be rewritten also as:

$$\mathcal{H} = g_F \sum_{i=S,V,T,A,P}[C_i\,(\bar{\psi}_p\mathcal{O}_i\psi_n)(\bar{\psi}_e\mathcal{O}^i\psi_\nu) + h.c.] \quad \textbf{(1.3)}$$

In the last equation, $\mathcal{O}_S = \mathbb{I}_{4x4}, \mathcal{O}_V = \gamma_\mu, \mathcal{O}_T = \frac{1}{\sqrt{2}}\sigma_{\lambda\mu}, \mathcal{O}_A = i\gamma_\mu\gamma_5$ and $\mathcal{O}_P = \gamma_5$. The numerical constants C_i are the so-called ***coupling constants*** and have to be determined by experiment. In this general Hamiltonian, the scalar and vector contribution come from transitions having a combined lepton spin 0, and these are called Fermi transitions. Tensor and axial-vector terms incorporate parallel lepton spins leading to so-called Gamow Teller transitions.

Discoveries about the non-conservation of parity were realized in the late 1950s. Lee and Yang originated the idea of parity non-conservation in the weak interaction and suggested several possible experiments [2]. Within one year Madame Wu and her colleagues performed the first such experiment with ^{60}Co [4] and demonstrated that parity was not conserved (P-violation) in the weak interaction. What they observed was that electrons were emitted preferentially in the direction of the ^{60}Co spin vector - a clear violation of parity conservation. This contribution was not even small - almost all of the electrons were emitted in only one direction. It seemed as if the violation was maximal, providing a direct way to define the notion of left-handedness and right-handedness scientifically. At the same time, the experiment of Wu and colleagues also meant that the charge conjugation symmetry is maximally violated in weak interactions. In order to include information on the parity non-conservation nature of weak interactions, Lee and Yang rewrote the Hamiltonian from Equation 1.3 to

$$\mathcal{H} = g_F \sum_{i=S,V,T,A,P}[(\bar{\psi}_p \mathcal{O}_i \psi_n)(\bar{\psi}_e \mathcal{O}^i (C_i + C'_i \gamma_5)\psi_\nu) + h.c.] \quad \textbf{(1.4)}$$

The Lee-Yang coupling constants C_i and C'_i, still define the relative strength of the different possible weak interaction types but the newly added primed coefficients include the information on the parity-non-conserving properties of the interactions. The experimental maximal parity violation imposed a condition on these coupling constants, $C'_i = \pm C_i$ giving

$$H = g_F \sum_{i=S,V,T,A,P}[C_i(\bar{\psi}_p O_i \psi_n)(\bar{\psi}_e O^i (1 \pm \gamma_5)\psi_\nu) + h.c.] \quad \textbf{(1.5)}$$

In principle all C_i are complex numbers, but when time-reversal is assumed the complex parts are reduced to zero [5]. Note that no indication for T-violation in beta decay has been observed till now [1].

Experiments on e.g., parity violation, neutrino helicity, spin change in nuclear β decays, muon decay, finally led to the V-A theory. The V-A theory implies to $C'_V = C_V = 1$, $C_A = C'_A$, and the rest of the coupling constants being zero. The V-A structure in the weak interactions was crucial to the unification of the weak and electromagnetic interactions by Weinberg, Salam, and Glashow [6]–[8]. The evolution from the 4-fermion point interaction to the SM interaction up to now is depicted in Figure 1.

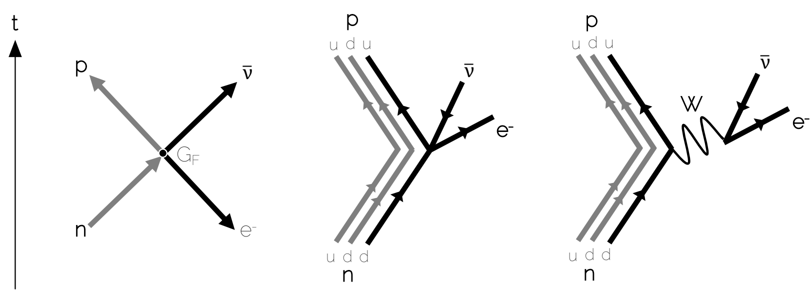

Figure 1. (left) Four-fermion point interaction. (center) Four fermion point interaction represented as a quark composition of a proton and neutron. (right) Feynman diagram of the weak interaction. The four-fermion vertex is no longer seen as a point of interaction and it is replaced with 2 vertices. The process is mediated by a massive boson, W-, with neutron decay being shown here.

One more point of view comes from the particle physics description (see Figure 1-right), i.e., the β-decay is caused by the conversion of the left-handed chiral states of leptons and quarks by the emission of a W^- boson [9]; this W^- boson subsequently decays into an electron and antineutrino, which at the quark level results in (for neutron decay):

$$d \longrightarrow u + e^- + \bar{\nu}_e \quad \textbf{(1.6)}$$

1.2.1. Coupling constants

Discrete symmetries as parity, charge conjugation, and time-reversal play a special role in the framework of the SM. The invariance under time reversal and maximal violation of parity and charge conjugation has been proved to be very useful to set certain conditions on the values of the coupling coefficients, as was mentioned briefly in the previous section with the maximal parity violation.

Based on experimental evidence, the SM prescribes purely vector and axial-vector currents, the V-A theory setting some conditions on the coupling constants: $C'_i = \pm C_i$ and $C_S = C_T = C_P = 0$. However, extensions of this model, such as super-symmetric theories with more than one charged Higgs doublet or leptoquarks naturally predict scalar or tensor currents [10], [11] and lead to non-SM contributions. The current limits on these parameters are given in [1] (see also Falkowski 2020 [12]):

$$\left|\frac{C_S}{C_V}\right| = 0.0014(12) \text{ and } \left|\frac{C_T}{C_A}\right| = 0.0020(22) \quad \textbf{(1.7)}$$

which are still in agreement with the SM prediction. However, experimental error bars still leave sufficient room for nuclear β decay experiments to improve the current constraints on these individual parameters, i.e., C_S and C_T.

To follow the SM approach, the pseudoscalar contribution, $\boldsymbol{C_p}$, is neglected in the data analysis in chapter 5 and 6. To address the reason, we have to look into the process $\pi \rightarrow e\nu$, which gives much more opportunity to reach for higher sensitivity to this coupling constant than β decays. A global fit in [13] resulted in $C_P = 348(11)\epsilon_p$, where ϵ_p is the Wilson coefficient which can be extracted from pion decay processes. A profound explanation about the sensitivity that can be reached for this coupling constant by pion and muon decays can be found in [1], [14].

Overview between energy and precision frontiers

If a slight deviation of scalar and tensor coupling constants from their zero values predicted in the SM would be observed in experiments at low energy, i.e., the precision frontier, this would allow one to link these results to the High Energy Physics (HEP), i.e., the energy frontier as is probed in LHC experiments. Such a link requires a theoretical framework with the least number of assumptions on it.

A model-independent effective field theory (EFT) suits these conditions where the only assumptions are Lorentz symmetry and the absence of non-standard light states, with the only possible exception of a right-handed neutrino [15]. Due to the fact that it is a general theory, it does not restrict the value of the variables involved in the analysis of any experimental data. Beta decay can be analyzed in this framework and the derived constraints on effective operators can be converted into constraints on the parameters of any SM extension [1]. Most of the low energy experiments aim to reach sensitivities between 10^{-3} and 10^{-4} on the coupling constants, turning low energy observables into ideal probes for new physics effects at the high energy scale (TeV). The dimensionless parameterization between the non-standard Wilson coefficients, ϵ_i*, and the new physics (NP) scale through the mass scale where physics beyond the standard model (BSM) appears, i.e., Λ_{BSM} is:

$$\epsilon_i\,, \tilde{\epsilon}_i = \left(\frac{E}{\Lambda_{BSM}}\right)^2 \qquad \textbf{(1.8)}$$

where E is the characteristic energy scale of a given process [15]. Thus, precision frontier experiments aiming at $\epsilon_i < 10^{-3}$ can explore the Λ_{BSM} = 5 - 10 TeV range, not fully explored at the energy frontier. For further details of equation 1.8, we refer to [1], [16] and references therein.

* The coupling constants C_i, also called Wilson coefficients, can be recovered from these parameters by computing the one-nucleon matrix elements of all quark bilinears, obtained from the paired onto a quark-level effective Lagrangian and nucleon-level effective Lagrangian, see [14].

1.3. Nuclear beta decay observables

As was mentioned in previous sections, the values of the coupling constants have to be determined experimentally. Measurements at low energy rely on three main types: relations between decay rate and energy release, β-spectrum shapes, and correlations among the directions of emission of particles in the decay. Following the latter type, one obtains as observables the energy and angular distribution of the β particle and the (anti-)neutrino in an allowed transition.

The distribution in electron and neutrino directions, electron polarization and energy for a beta transition can be determined using Fermi's Golden Rule. One can integrate over all the differential variables in Eq.1.5, in order to obtain the decay rate equation described by Jackson et. al. [17], which in absence of orientation of the initial state and without detection of the lepton's helicity can be written as

$$\omega(\langle J\rangle|\, E_e, \Omega_e, \Omega_\nu)\, dE_e d\Omega_e d\Omega_\nu \;=\; \frac{F(\pm Z, E_e)}{(2\pi)^5} p_e E_e (E_0 - E_e)^2 dE_e d\Omega_e \Omega_\nu \times \xi\{\mathbb{I} + a\frac{p_e \cdot p_\nu}{E_e E_\nu} + b\frac{m}{E_e} + \;...\} \qquad \textbf{(1.9)}$$

To make the previous equation simpler, only the terms important to this work are presented. Full expressions can be found in [17]. The labels $\boldsymbol{e}$ and $\boldsymbol{\nu}$ are used to denote the electron and neutrino particles, respectively. E_i, p_i and Ω_i are the total energy, momentum and angular coordinates of the leptons. E_0 is the maximum total electron energy, m_e is the electron rest mass, $\langle J\rangle$ is the nuclear polarization of the initial nuclear state with $\mathbf{J}$ spin vector, and $F(\pm Z, E_e)$ is the Fermi function, which contains the dominant Coulomb correction and the atomic number of the daughter nucleus.

The correlation coefficients: $a = a_{\beta\nu}$ and b_F are the so-called β−ν angular correlation and Fierz interference term, respectively, which depend on the Fermi and Gamow-Teller matrix elements, $|M_F|^2$ and $|M_{GT}|^2$, respectively, on the coupling constants, $C_i^{(\prime)}$, and the β-energy spectrum. The factor ξ is described as:

$$\xi = |M_F|^2(|C_S|^2 + |C_V|^2 + |C'_S|^2 + |C'_V|^2) + |M_{GT}|^2(|C_T|^2 + |C_A|^2 + |C'_T|^2 + |C'_A|^2) \qquad \textbf{(1.10)}$$

The particular expressions for the correlation coefficients are:

$$a\xi = |M_F|^2(-|C_S|^2 + |C_V|^2 - |C'_S|^2 + |C'_V|^2) + \frac{|M_{GT}|^2}{3}(|C_T|^2 - |C_A|^2 + |C'_T|^2 - |C'_A|^2) \qquad \textbf{(1.11)}$$

$$b\xi = \pm 2\gamma Re\big(|M_F|^2(C_V C_S^* + C'_V C'^*_S) + |M_{GT}|^2(C_A C_T^* + C'_A C'^*_T)\big) \qquad \textbf{(1.12)}$$

with the upper (lower) sign for $\beta^-(\beta^+)$ decay and with $\gamma \equiv \sqrt{1-\alpha^2 Z^2}$ and α the fine structure constant. Equation 1.9 is perfectly general. No assumptions concerning invariance with respect to space inversion, charge conjugation, or time reversal have been made.

It is clear that a precise measurement of the β−ν angular correlation coefficient ($a_{\beta\nu}$) and of the Fierz interference term (**b**) lead to important information on non-SM contributions. The fact that the correlation coefficient provides information on the nature of the couplings can be understood more easily if we use pure Fermi and pure Gamow-Teller transitions as examples in the expressions 1.11 and 1.12.

Pure Fermi transitions

In a $0^+ \rightarrow 0^+$ β–decay, the two leptons have to couple to zero angular momentum. The SM prescribes a vector current, and the leptons should then be emitted preferentially parallel to each other. If scalar currents dominated, the leptons would be emitted preferentially anti-parallel, which implies that one of the leptons would have the "wrong" (i.e., non-SM) helicity. The above-mentioned equations 1.11 and 1.12, for this kind of transitions then simplify to $C_{V,S}$ contributions only. Skimming on the new equations 1.13 and 1.14, one can see a quadratic and linear dependence on the non-SM contributions present in $a_{\beta\nu}$ and the Fierz term, respectively:

$$a_{\beta\nu}^{F} \approx 1 - \frac{|C_S|^2 + |C'_s|^2}{|C_V|^2} \qquad \textbf{(1.13)}$$

and

$$\mathrm{b^F} \approx \pm\mathrm{Re}\left(\frac{\mathrm{C_S + C'_S}}{\mathrm{C_V}}\right) \qquad \textbf{(1.14)}$$

The superscript **F** emphasizes that the angular correlation coefficient and the Fierz term are expressed for pure Fermi (F) transitions.

Pure GT transitions

In Gamow-Teller transitions, the spins of the emitted leptons couple to a total spin equal to one, S=1, leading to an angular momentum change $\Delta J = 0, \pm 1$ between the initial and final angular momentum states of the nucleus. In this case, the SM prescribes an axial-vector current, and the leptons should be preferably emitted anti-parallel to each other. Equations 1.15 and 1.16, to which Equations 1.11 and 1.12 in this case reduce, will now depend, contrary to the F transitions, will depend on the axial-vector and tensor coupling constants, $C_{A,T}$. The quadratic and linear dependence on the non-SM contributions persists in this case as well:

$$a_{\beta\nu}^{GT} \approx -\frac{1}{3}\left[1 - \frac{|C_T|^2 + |C'_T|^2}{|C_A|^2}\right] \tag{1.15}$$

and

$$b^{GT} \approx \pm Re\left(\frac{C_T + C'_T}{C_A}\right) \tag{1.16}$$

The superscript **GT** emphasizes that the angular correlation coefficient and the Fierz term are expressed in this case for pure Gamow-Teller (GT) transitions.

High-precision measurements at low energy aim to look for small contributions of S or T components that could hint at physics beyond the SM. It is highly recommended to pick out one of the pure transitions to increase the sensitivity to a specific non-SM contribution, instead of a mixed transition which leads us to a combination of all four terms.

In the present work, measurements on the β−ν angular correlation will be used as a sensitive tool to provide constraints on scalar and tensor contributions. Nevertheless, it is still important to give some details related to the Fierz term and the β energy spectrum before deepening into information regarding measurements on the angular correlation coefficient, $a_{\beta\nu}$.

Fierz interference-term and why we don't need it.

The linear dependence on the coupling constants gives to the Fierz term a high sensitivity level to search for non-SM contributions [18]–[20]. As the Fierz term in Eq. 1.14 depends only on the energy of the emitted β particle, see Eq. 1.9, and does not have any privileged directional dependence, a measurement of any correlation coefficient will always include $b' \equiv bm/E_e$. It is therefore not possible to perform measurements of $a_{\beta\nu}$ independently of b_F.

A measurement of the β-spectrum shape, which depends on the beta-particle energy but has no directional dependence, allows in principle to determine the Fierz term b_F and b_{GT}.

One can make some assumptions on the value of the Fierz term avoiding a direct measurement of the β-spectrum shape. Previous experiments, as will be discussed in the next chapter, extracted the value of the $a_{\beta\nu}$ correlation coefficient, setting $b' = 0$. The second option is to extract the b' value by means of Monte Carlo simulations as the full study presented in [19]. This study shows that a misinterpretation in the bounds on the Fierz-term can lead us to give a wrong value to $a_{\beta\nu}$. Since every measurement performed on any correlation coefficient, includes the b-term it is convenient to rewrite the angular correlation coefficient in terms of the Fierz term as follows:

$$\tilde{a} = \frac{a_{\beta\nu}}{1+b<m/W>'} \quad \textbf{(1.17)}$$

The denominator in equation 1.17 results from the integration of equation 1.9 over the angle, θ, between the beta particle and the neutrino and integration over the phase space. This expression holds only when the integration limits of the β particle energy, W, are carried out without dependence on the angle θ. The term $< m/W >$ can be written as a function of the endpoint energy as is shown in [19].

2
The $\beta - \nu$ angular correlation

There are two possible outcomes: if the result confirms the hypothesis, then you've made a measurement. If the result is contrary to the hypothesis, then you've made a discovery. -E Fermi

A direct measurement of exotic contributions to the weak interaction is the observation of the angular correlation between the two leptons for a certain beta decay process. In this chapter, a brief summary of the experimental techniques used previously to address $a_{\beta\nu}$ is presented. The current efforts pursuing its high precision determination are also reviewed.

2.1. Physics case

As stated in section 1.3, the β−ν angular correlation coefficient, $a_{\beta\nu}$, can be deduced in experiments with unpolarized nuclei in the allowed approximation of the β decay rate, as given in equation 1.9. From this equation, it can easily be seen that $a_{\beta\nu}$ has to be accessed experimentally by determining the angular correlation between the beta particle and the neutrino. This correlation can be obtained through direct measurements of the recoil energy distribution of the daughter nuclei or by coincidences with the beta particle. Besides these techniques, an indirect analysis can be done by choosing an unstable daughter nucleus, which undergoes delayed particle or gamma emission, in order to reconstruct the kinematics of the emitted leptons. Direct measurement of the angle between the leptons emitted from the β-decay, i.e., $\beta^{\pm}$ particle and (anti)neutrino, is omitted due to the difficulty to detect the latter.

Figure 2 explains the properties of the interactions that lead to different angular correlations in nuclear beta decay. The two possible scenarios for the recoil energy of the daughter nuclei in a $0^+ \rightarrow 0^+$ decay are: *(i)* For a pure scalar scenario, the angular distribution between the β particle and the neutrino reaches its maximum at 180°, being the preferred angle of emission, the leptons carry away no net angular momentum, meaning the leptons have opposite spin and equal helicities, and the recoil energy of the daughter nucleus will be small, i.e., typically less than 100 eV. *(ii)* For a pure vector scenario, an opposite behavior is expected. The preferred angle between the leptons is minimal (0°) and the daughter nuclei experience a large recoil energy. Notice that the momentum of the daughter nuclei is the vector-sum of the momenta of the neutrino and the β particle. The effect on the recoil energy that one commonly is looking for is tiny. Therefore, the measurements designed to identify exotic current like a scalar current require high sensitivity and rigorous control of the systematic errors and a high counting statistic. A detailed discussion on the control of systematic errors is presented in Chapter 6.

A compendium of techniques and angular correlation values obtained by experiments that took advantage of the spin structure for pure transitions in the β decay, i.e., Fermi (F) and Gamow-Teller (GT), are indicated in the following subsection. If for an isotope a pure transition is not existing, a well-known mixing ratio would be required.

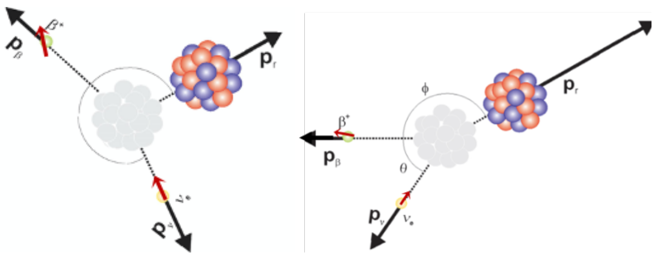

Figure 2. Recoil energy of the daughter nucleus as a function of the angle between the β particle and the neutrino. (left) For a pure scalar decay, the helicities must be the same, thus neutrino and β particles will be emitted in opposite directions. (right) In a pure vector interaction, the leptons are emitted parallel since their helicities must be opposite giving thus to the daughter nuclei a large recoil energy. The red arrows show the spin vectors of the leptons.

2.1.1. Beta-neutrino experiments

The growing body of experiments using different techniques to measure the β−ν angular correlation of various β decays is presented, highlighting the values of the coupling constants achieved in these experiments, to close the chapter up with the sensitivity needed to gain a better constraint on these coupling constants.

One of the most common ways to measure the angular correlation is through the recoil energy of the daughter nuclei. A first example is a study made by Johnson et al. measuring the recoil energy spectrum from the allowed β^- decay of ^{6}He looking for a tensor contribution [21]. This nucleus undergoes a pure allowed GT transition $0^+ \rightarrow 1^+$ to a single final state. The value quoted by Johnson is $a_{\beta\nu} = -0.3343(30)$ being one of the most accurate values for GT transitions. The most serious limitation of this measurement is the detection efficiency. Other examples using a similar approach were presented by Allen et al. observing the energy spectra of recoil ions from the decay of ^{6}He, ^{19}Ne, ^{23}Ne, and ^{35}Ar [22].

With the development of Penning, Paul, and Magneto-Optical (MOT) traps, a new series of beta neutrino correlation experiments has emerged with the investigation of decay kinematics through the direct measurement of the daughter nucleus recoil energy or by detecting secondary particles emitted after the decay. Generally speaking, a trapping technique provides a confining potential made by an electric field or by a combination of electric and magnetic fields, creating ions (Paul and Penning traps) or atoms (MOT) nearly at rest in vacuum, which is an ideal environment to study the kinematics of radioactive decays, [23].

Scielzo et al. in 2004 studied the case of a transition between mirror states $^{21}\mathrm{Na}\left(\frac{3}{2}^{+}\right) \rightarrow {}^{21}\mathrm{Ne}\left(\frac{3}{2}^{+}\right)$ (F/GT mixed) using the MOT technique. The value of $a_{\beta\nu}$ deduced in this work is $a_{\beta\nu} = 0.5243(91)$. As discussed in [24], one of the prime sources of systematic errors is caused by the photoassociation of molecular sodium in the trap. Vetter et al. suppressed the fraction of trapped atoms in the molecular state by using a dark trap reducing the photoassociation process. This experiment detected the time of flight (TOF) of the recoil nucleus in coincidence with the electrons from the β decay of ^{21}Na inside the MOT, yielding a value of $a_{\beta\nu} = 0.5502(60)$, [25]. The remaining systematic uncertainties are the position and size of the atom cloud as well as the subtraction of background.
Based on the TOF approach, Fléchard et al. used a transparent Paul trap, where the $a_{\beta\nu}$ value is deduced from the TOF of the recoil nuclei detected in coincidence with the β particle from the $^{6}He^{+}$ decay leading to a final value of $a_{\beta\nu} = -0.3335(73)_{stat}(75)_{syst}$ [26]. The use of a Paul trap allowed the preparation of a scattering-free source of ions, being the first experiment that uses an ion trap to determine the beta-neutrino angular correlation.
Trapping techniques were also used to search for scalar contributions. Gorelov et al. used the MOT to provide a backing-free source of $^{38}K^{m}$ atoms in a $0^{+} \rightarrow 0^{+}$ pure F decay. The recoiling nucleus was detected in coincidence with the emitted β particle. The published value is $\tilde{a} = 0.9981 \pm 0.0030^{+0.0032}_{-0.0037}$ [27] and constitutes the most precise result on scalar weak currents from an $\beta - \nu$ angular correlation measurement. The WITCH experiment used a Penning trap to measure the energy of the recoiling daughter nuclei from the β^{+} decay of ^{35}Ar, yielding $\tilde{a} = 1.12(33)$ [28]. In the experiments discussed till now, the $\beta - \nu$ angular correlation

has been determined from the measurement of the energy of the recoiling nucleus, leaving room to improve the precision. If a decay is selected that brings the recoiling nucleus in an excited state with a short half-life, the momentum of the particle or photon emitted from this state, is shifted by the recoil ion motion. Previous experiments miscalled this technique as Doppler shift due to the similarity with the Doppler effect [29], [30]. The effect is nowadays more properly referred to as the kinematic energy shift.

The precise measurement of this kinematic energy shift, together with the emitted beta-particle momentum, determines the direction of the momentum of the recoiling nucleus and, therefore, the direction of the neutrino. Such indirect measurements give an energy broadening of the delayed particle emitted after the β decay, which depends on the kinematic energy of the recoiling nucleus. Examples of kinematic shift measurements performed by Clifford et al. used a $\beta - \nu - \alpha$ triple correlation in the decay of ^{20}Na. A carbon catcher foil located at the center of a coplanar array of α and β detectors was used to stop the ^{20}Na beam. The geometry of the detection setup allowed coincident measurements between α–β events detected at three different emission angles, giving thus six detectors combinations to obtain the energy difference between the emitted particles opening up possibilities for new and indirect measurement techniques that achieve higher precision values on $a_{\beta\nu}$ [31]. For instance, after a first measurement in 1993 by Riisager and Schardt [32], Adelberger et al. [33] , in 1999, used the superallowed $0^+ \rightarrow 0^+$ decay of ^{32}Ar, implanted in a carbon foil. The technique used is based on the instability of the ^{32}Cl daughter nucleus, which emits a proton shortly after the beta decay. The kinematics of the beta decay is reflected in the energy of these protons (broadening of the proton peaks due to the kinematic shift). The resulting value from this experiment is $a_{\beta\nu} = 0.9989(52)_{\mathrm{stat}}(36)_{\mathrm{syst}}$,[33]. Due to an update of the mass and excitation energies of ^{32}Ar, this value has been recently reviewed to be $a_{\beta\nu} = 1.0050(52)_{\mathrm{stat}}$ [34].

Similar experiments using this indirect measurement technique looking for scalar contributions were performed by Egorov et al. using ^{18}Ne [30]. Vorobel et. al. [35] used positrons and coincident γ–rays from the pure Fermi $0^+ \rightarrow 0^+$ branch of the β decay of ^{14}O. In a search for tensor contributions, Stenberg et. al. studied the $\beta - \bar{\nu} - \alpha$ correlation in the β decay of ^{8}Li, where the α-particles comes from the breakup of ^{8}Be [36]. Table 2 compares some of the above-cited values of $a_{\beta\nu}$ according to the nuclide and the transition, the observables used in the experiment as well as the value of $a_{\beta\nu}$. One can note, the improvement in sensitivity over the years, mostly due to the improvement and sophistication in the experimental arrangements.

Table 2. Experiments on beta-neutrino angular correlations in beta decay.

Type	Nuclide	J_i	J_f	Observable	a(error) $()_{stat}()_{syst}$	Ref	Year
a^F	^{14}O	0	0	$\delta E_\gamma(E_\beta,\theta)$	1.00(3)	[35]	2003
	^{18}Ne	0	0	$\delta E_\gamma(E_\beta,\theta)$	1.06(19)	[30]	1997
	^{32}Ar	0	0	$N(\delta E_p)$	1.00(8)	[32]	1993
	^{32}Ar	0	0	$\delta E_p(E_\beta,\theta)$	0.9989(52)(36) 1.0050(52)()†	[33], [34]	2003
	^{33}Ar♦	1/2	1/2	$N(\delta E_p)$	1.02(4)	[32]	1993
	^{38m}K	0	0		0.9981(48)	[27]	2005
a^{GT}	^{6}He			E_R	-0.3343(30)	[21]	1963
				TOF & E_β	-0.3335(73)(75)	[26]	2011
	^{8}Li	2	2	$\delta E_\alpha(E_\beta,\theta)$	-0.3342(26)(29)	[36]	2015
	^{19}Ne♦	1/2	1/2	$N(E_R)$	0.00(8)	[22]	1959
	^{20}Na	2	2	$\delta E_\alpha(E_\beta,\theta)$	-0.3330(330)	[31]	1989
	^{23}Na			E_R	-0.37(4)	[22]	1959

Observable value: N=number of events, E=particle energy, θ = angle between emitted particles.

♦Mixed transitions. † Improved value after considering the updated value for the ^{32}Ar-mass quoted in [34].

2.1.2. State-of-the-art

As shown in Table 2, the experimental error bars still leave sufficient room to better constrain the limits for scalar and tensor interactions. Until now, the values quoted regardless of the technique used have yielded a precision on $a_{\beta\nu} \approx 5 \cdot 10^{-3}$ for pure F transitions [27], [33] and $a_{\beta\nu} \approx 3 \cdot 10^{-3}$ for pure GT ones [21], [36]. The present project aims at a precision of 10^{-3} [37], [38] improving by of factor 5 or more the most precise result quoted by Adelberger et. al. [33]. Other experiments aiming at a precision level of 10^{-3} and below, are found in [39]–[42].

The plots in Figure 3 show the expected constraints on scalar (left) and tensor (right) contributions, respectively, from the most precise experiments to date. Further planned experiments are the LPCTrap experiment at GANIL using ^{6}He as a case of study [43] and the TAMUTRAP experiment where superallowed beta emitters will be used [44], apart from the TRINAT experiment [45] at TRIUMF using ^{38m}K to improve the limits on F transitions quoted by Gorelov et al. in 2005 and the Ne-MOT experiment using neon isotopes (^{18}Ne, ^{19}Ne and ^{23}Ne) at SARAF [46].

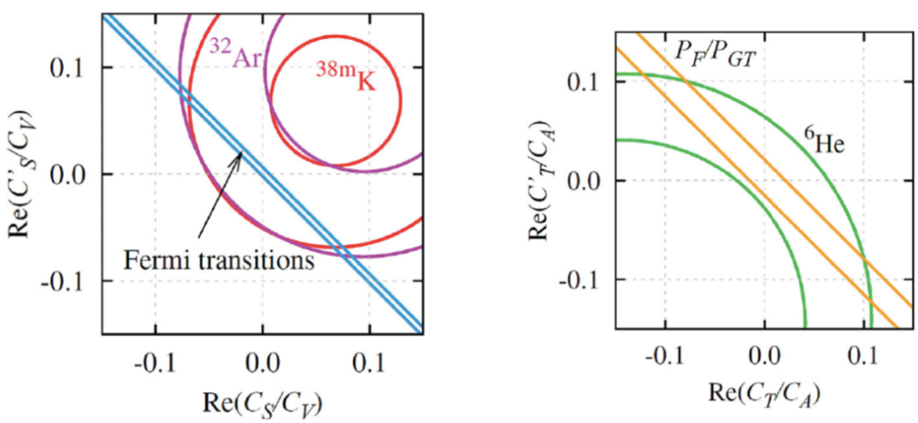

Figure 3. Exclusion plot on the real part for the scalar (right) and tensor (left) coupling constants. In both cases, the straight lines represent the limits for the Fierz interference term in superallowed F transitions (blue) and the relative polarization P_F/P_{GT} for the positrons emitted by F and GT decays [47] (yellow). The circular limits are deduced from measurements of the beta neutrino angular correlation in ^{38m}K decay [27] (red lines), ^{32}Ar decay [33] (purple lines), and by the ^{6}He [21] decay (right). The limits are calculated at the 90% CL. Both plots taken from [48].

3
Kinematic energy shift

If I have seen further than others, it is by standing upon the shoulders of giants. — I. Newton

A new challenge arises in the determination of the $a_{\beta\nu}$ coefficient: to find a suitable experimental technique that allows to control the sources of systematic errors at high precision level. In the present chapter, the problem of reaching a higher experimental precision on $a_{\beta\nu}$ through the kinematic energy shift technique is examined. The proof-of-principle of the WISArD experiment is also introduced.

3.1. Experimental technique and case of study

Up to this date, two different experimental techniques have been used to achieve the highest precision in the determination of the angular correlation coefficient in a Fermi transition.

The first one uses a beta-delayed secondary (proton) emission. As the daughter nucleus of the beta decay recoils, the secondary emitted particle will suffer an energy shift in the laboratory frame since it is released from a moving source. Since the recoil is isotropic, what we observe is the broadening in the energy distribution of the secondary particle.
Unfortunately, without conditioning or tracking the direction of the emitted particles, this approach results in problems related to adding up beta-background into the proton spectra as was found by Schardt et al. In their work, the broadened proton energy was measured by limiting the beta particle detection within a small solid angle relative to the emitted proton. This experiment suffers from low statistics as only those events that are within the solid angle are considered; this cannot be enlarged without increasing the probability of a proton summing with its associated beta. Nevertheless, this work quoted one of the most precise results for the angular correlation coefficient for $0^+ \rightarrow 0^+$ beta decay of ^{32}Ar, thanks to its superior proton energy resolution.

A more recent study of the same isotope, ^{32}Ar, was done by Adelberger et al. who placed the detection setup inside a 3.5T superconducting solenoid in order to prevent the beta particles from reaching the proton detectors. Nevertheless, the resulting proton energy spectrum suffered from beta-background, since the emitted beta-particle and the protons

hit the same detector, and consequently, the broadening shape of the proton distribution was affected.
The second experimental technique implies a detection in coincidence, for instance between the lepton emitted in the beta decay (beta-particle) and the secondary particle. In this configuration it is then possible to observe a shift in the mean-energy of the secondary particle (protons). This technique was implemented by looking at the coincidence between the energy of the delayed α-particle from ^{20}Na and beta particles emitted [31]. Similarly, Egorov et al. [30] used delayed gamma rays from ^{18}Ne decay in coincidence with beta particles.
The key problem with these techniques is the background in the proton or gamma ray spectra predominantly from beta particles.

The WISArD experiment has tailored specific solutions to this specific problem by tracking independently, the particles involved in the beta delayed particle emission. The advantage becomes all the more significant when the mean value (centroid) instead of the broadening of the proton energy distribution is measured. The aim of this approach is to improve by a factor of three to five the present limits on the scalar currents compared to the quoted values in [27], [32], [33] relaying on the energy resolution of the detection system.
One more advantage of this technique is that it is less sensitive to the response function of the proton detector than in the case of measuring the broadening of the proton distribution in a singles measurement.

First, the choice of the right nuclear system has to be considered. In principle, any delayed-proton precursor that has a strong superallowed branch could be used to study the beta neutrino angular correlation. But for practical considerations, the isotope selection has to be restricted to specific cases of study. In the following section, a full discussion about the isotope requirements is presented.

3.1.1. Isotope requirements

The choice of the right beta decay process is of paramount importance: specific requirements must be met as the production yield of the primary isotope has to be high to get enough statistics and the beta decay should be either a pure Fermi or a pure Gamow-Teller transition. The daughter nucleus has to be unstable for the delayed emission of a secondary particle. The half-life of the populated level in beta decay has to be small enough so that the nucleus should not have decelerated before emitting the secondary particle. In this way the secondary particle is emitted from a nucleus which still moves with the velocity acquired from the beta decay.

The latter requirements can be seen in Figure 4, where the colors indicate those candidates that have positive Q_β values and whose daughters are also proton emitters. In the close-up, the observed region pinpoints isotopes that are considered candidates, where only ^{32}Ar and ^{38m}K have already been a case study for the search for scalar contributions. The ^{32}Ar decay has been used by measuring the broadening of the beta delayed proton emission [32], [33], the isomer ^{38m}K by studying the recoil energy distribution in MOT experiments [27]. The isotope selection over these candidates will depend only on the yield production. For instance, in a low-energy radioactive beam facility as ISOLDE at CERN, only ^{32}Ar and ^{20}Mg are candidates. Further, the latter one is less favored because it would require a high mass separator to distinguish between the isomers ^{20}Mg and ^{20}Na, which is presently not possible. The ^{20}Na is an alpha emitter, which would strongly pollute the ^{20}Mg spectra. All other candidates are not or very weakly produced at ISOLDE.

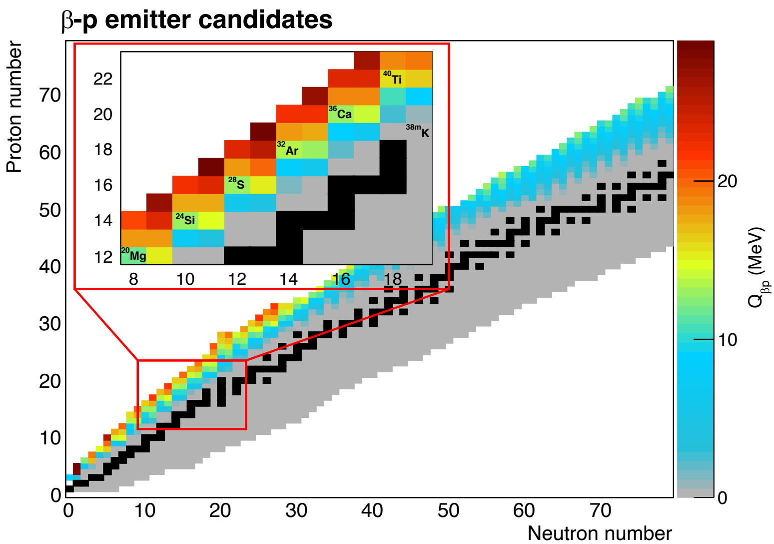

Figure 4. Close up to the possible candidates to search for scalar contributions in beta-delayed proton decay. The color scheme from low (blue) to high (red) represents the energy value of Q_β - S_p. So far ^{32}Ar and ^{38m}K have been studied using different experimental techniques.

3.2. WISArD: The 0.1% challenge

The <u>W</u>eak <u>I</u>nteraction <u>S</u>tudies with ^{32}<u>**Ar**</u>gon <u>**D**</u>ecay, **WISArD**, experiment builds upon previous efforts in precise measurements of the angular correlation coefficient using the kinematic energy shift technique as approach.

As a first case of study, the superallowed F transition of ^{32}Ar (0^+, Q_{EC} = 11134.4(19) keV, $T_{1/2}$ = 98(2) ms) to the T=2 state in ^{32}Cl (0^+, E^* =5046 keV) is examined. The kinematic energy shift results from the ^{32}Ar decay to the isobaric analogue state in ^{32}Cl. In this case, the maximum kinematic energy of the recoiling ^{32}Cl is 517 eV considering a maximum velocity of v = $1.86\text{x}10^{-4}$c, with *c* being the speed of light. Details of this calculation can be found in Appendix A and [49]. The T=2 state in ^{32}Cl is a proton unbound state with a width of $\Gamma \approx$ 20eV giving a half-life so short ($T_{1/2} \approx 3\text{x}10^{-17}$ s) that the daughter nuclei travel on average less than $2\text{x}10^{-2}$Å before emitting the proton, and thus without the possibility of any other interaction to slow down its velocity. Therefore, all the kinematics of ^{32}Cl is inherited to the delayed protons while it is still traveling with the full velocity.

The ^{32}Ar decay and emission of the delayed proton proceeds as

$$^{32}_{18}Ar_{14} \rightarrow {}^{32}_{17}Cl_{15} + e^{+} + \nu_e$$

$$^{32}_{17}Cl_{15} \rightarrow {}^{31}S + p$$

As mentioned before, via the angular correlation between the emitted leptons, one can distinguish between the two interaction types: a pure F transition (driven by vector and scalar interactions) or a pure GT transition (i.e., axial-vector and tensor interactions). Figure 5 points the two possible scenarios where the energy distribution of the recoiling nucleus (^{32}Cl) is influenced by the angular correlation between the emitted leptons of the beta decay. Hence the proton, which is emitted from a moving source, will suffer a kinematic shift. This secondary shift will of course depend on the direction of emission relative to the recoil direction.

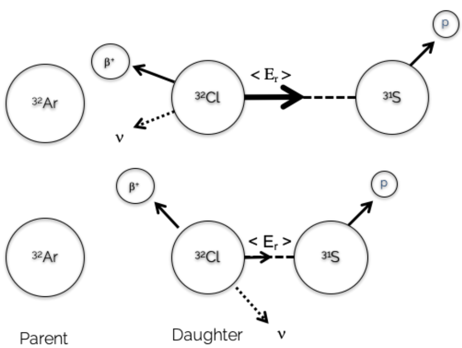

Figure 5 : The recoil energy of the daughter ^{32}Cl depends on the emission angle between the beta particle and the neutrino. Top: leptons preferentially emitted in the same direction gives a stronger recoil energy. This is the case for a Fermi decay. Bottom: For a Gamow-Teller

decay, both lepton particles are emitted preferentially in opposite directions and the recoil energy is much smaller.

Because the WISArD experiment takes advantage of clean proton spectra with a good energy resolution (as it will be discussed in chapter 5) allowing to distinguish between different proton lines and thus studying simultaneously scalar and tensor current contributions using the same experimental setup. This is a clear advantage over previous measurements, which were concentrated only on one current contribution, either scalar or tensor, by focusing on a single proton or gamma peak in the spectrum.

In this work, the precise measurement of the angular correlation coefficient in a superallowed $0^+ \rightarrow 0^+$ beta decay of ^{32}Ar transition is used to search for scalar contributions, and for the first time, protons following GT transitions in the same isotope are studied simultaneously to search for tensor contributions with the same setup. The proton lines following GT transitions are less pronounced than for the F transition, due to a lower branching ratio, generating insufficient statistics to improve the current upper limit on tensor interaction. Despite, this limitation, a number of transitions were studied in this work to establish overall consistency and set a reference for future improvements in the experimental design. Figure 6 shows the partial decay scheme of ^{32}Ar. The superallowed $0^+ \rightarrow 0^+$ F transition to search for scalar contributions and the pure GT ($0^+ \rightarrow 1^+$) transitions of interest are indicated.

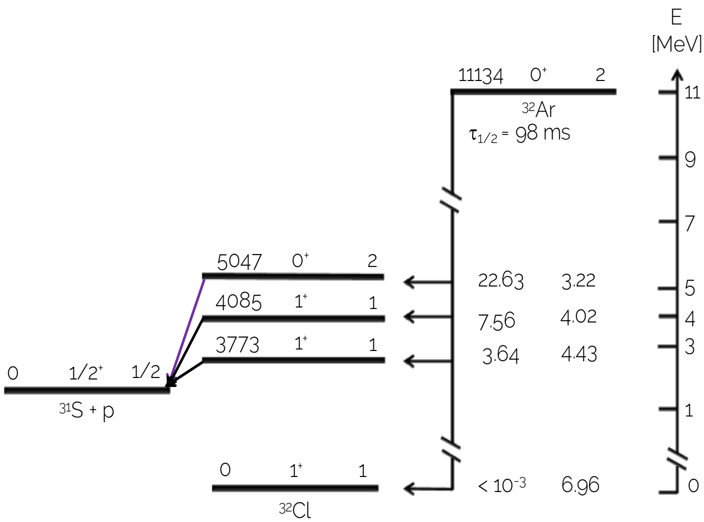

Figure 6: Partial decay scheme of ^{32}Ar that shows the β-delayed proton lines used in this work. The numbers shown above each state are, from

left to right, the excitation energy in keV, the spin and parity, and the isospin, respectively. The numbers given for the β decay branches of ^{32}Ar are the branching ratio (in %) and log ft value.

The proton energies presented in Figure 6 were taken from a detailed study of the beta decay properties of ^{32}Ar, Blank et al., [50]. Information related to the ^{33}Ar isotope is taken from Adimi et al., [51]. These proton energy values are used in the energy calibration section within the data analysis chapter.

3.3. Proof-of-principle experiment

To examine the impact of applying proton-positron coincidence measurements, GEANT4-based Monte Carlo simulations [52] were performed with a proton energy resolution of 10 keV to demonstrate the feasibility of the WISArD approach (see refs. [33], [37]). A detailed discussion about the experimental setup is present in the following chapter. Figure 7 shows the detection setup that was used in both the simulations and in the proof-of-principle experiment, with a beta detector above the ^{32}Ar sample and a proton detector at each side of it (up and down). The expected proton energy shapes in positron-proton coincidence measurements, for the Fermi transition is presented.

The Monte Carlo simulations demonstrated the clear difference in proton energy distribution that follows from two Fermi scenarios: (left) a pure vector current and (right) a pure scalar current.

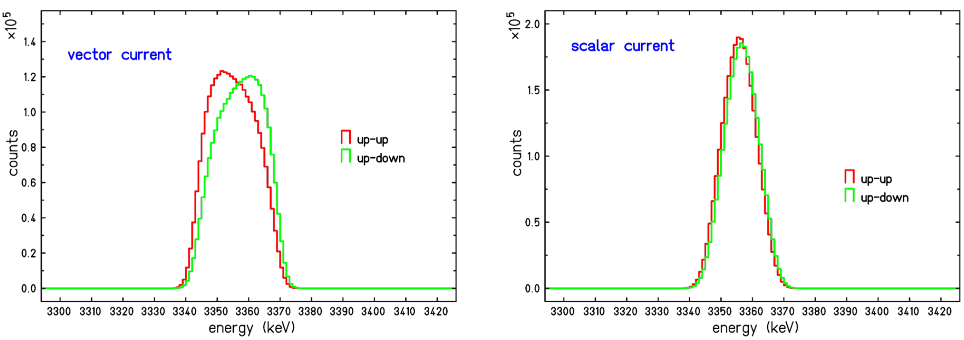

Figure 7: (left) Monte Carlo simulation performed with a proton energy resolution of 10 keV (FWHM) for a pure vector contribution. The difference between the kinematic energy shift for protons and positrons traveling in the same direction (up-up) or in opposite directions (up-down) highlights the sensitivity required for the proton detectors in order to achieve 0.1% precision, in this case 10 keV energy resolution is required. (right) A pure scalar contribution is presented§.

For simplicity, let us examine the simplest frame of reference, up and down, where "up" is to choose those particles that travel upward immediately after the beta decay and "down" for those particles that travel downwards with respect to an applied magnetic field.

The part for the pure vector current in Figure 7 (left) presents two possible cases after applying the proton-positron coincidence condition. The first one is by choosing those protons traveling in the same direction (parallel) as the positrons and both being detected in the upper hemisphere (up-up label). In this case, the proton energy distribution will be slowed down because the protons are emitted in the opposite direction in which the daughter nuclei move (red). The second case consists in selecting those protons that travel in the opposite direction (antiparallel) to the positron. In this case, positrons are detected in the upper hemisphere and the protons have to be detected in the lower hemisphere. The daughter nuclei move, for this configuration, in the same direction as the emitted proton, boosting its energy, as can be seen in the up-down label (green).

In contrast, for a scalar current, in which the recoil energy is small, there is no difference between the proton and the positron detected in the same direction (up-up) or opposite direction (up-down), as was expected and proven by the Monte Carlo simulations (Figure 7, right panel).

The mean value (centroid) of the proton energy distribution (the WISArD approach) for each case will give us the information related to the kinematic proton energy shift, which is more sensitive to scalar or tensor currents than the broadening of its shape. Afterwards, this value will be used as a reference to compare with GEANT4 simulations with different values of the angular correlation coefficient. Interpolating the experimental value with the simulated ones will lead to the final value for the angular correlation coefficient, $a_{\beta\nu}$. In our proof-of-principle experiment, only the detection of the positron in a single hemisphere was studied, but the possibility of studying both directions and therefore coincidences with the protons in the opposite direction is contemplated for future planned measurements.
One more benefit to performing simulations before actually performing the experiment is to stress out the requirements of the setup, in this case the energy resolution for the proton detectors. If a proton resolution better than 10 keV can be obtained, a new limit for $a_{\beta\nu}$ (of the order of 0.1%) can be achieved [37]. Such a measurement would be complementary to the future LHC experiments where a similar sensitivity is expected (*see e.g., Fig. 14 in Ref.* [1]).

§ The labels up-up and up-down in Figure 7, match the labeling used as a reference in the detection setup of the WISArD experiment, and later on in the data analysis, which is detailed in chapters 4 and 5, respectively.

4
The WISArD Experiment: setup

It doesn't matter how beautiful your theory is, it doesn't matter how smart you are. If it doesn't agree with experiment, it's wrong. - R Feynman

GEANT4 based Monte Carlo simulations presented in [37] highlight the importance of the energy resolution of the proton detector. To achieve better accuracy, positrons and protons were guided into two different detectors: plastic scintillator and silicon detectors, respectively.

In this chapter, the experimental setup with its challenges is presented, including how the apparatus, detectors, and acquisition system were set up. The ^{32}Ar beam production at the ISOLDE facility at CERN, the beamtime period, and the steps used to collect the data are described also.

4.1. WISArD setup

The WISArD setup makes use of the former WITCH beamline [53] located in the ISOLDE Hall [54] at the Conseil Européen pour la Recherche Nucléaire, CERN. This particular apparatus was chosen because it hosts a vertical superconducting solenoid (superconducting magnet by Oxford Instruments) which provides a strong magnetic field up to 9T besides its convenient location inside an ISOL-type facility.

The proof-of-principle experiment was carried out with available detectors and with the beam optics equipment from the former WITCH experiment. A final dedicated setup for WISArD is currently under development. The proof-of-principle experiment was performed at ISOLDE in the last beamtime campaign in 2018, just before the long shut-down period at CERN. Figure 8 shows how the ISOLDE Radioactive Beam Facility is linked to the external proton beam from the Proton Synchrotron (PS) Booster within the accelerator complex of CERN.

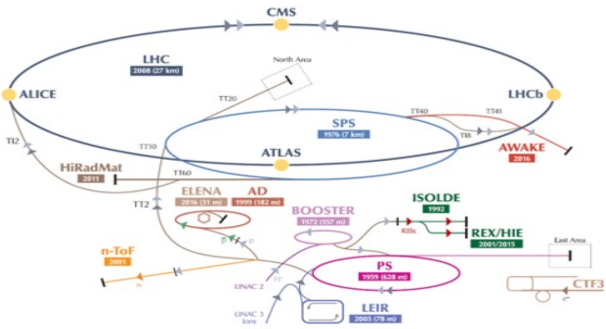

Figure 8. Layout of the complete accelerator complex at the Conseil Européen pour la Recherche Nucléaire, CERN. In green, the Radioactive Ion Beam Facility, ISOLDE (Isotope OnLine DEvice).

To produce the ^{32}Ar beam, 1.4 GeV proton pulses in a low repetition rate (in multiples of 1.2 s) from the PS Booster are impinging on a CaO (nanostructured powder) thick target [55] with a mean intensity of 1.4 μA in the ISOLDE target area where the radioactive ions are created via spallation, fragmentation, or fission reactions. The exotic cocktail of isotopes is then extracted, ionized, accelerated by the Versatile Arc Discharge Ion Source (VADIS) to then be separated by the High-Resolution Separator (HRS). The layout of the ISOLDE Hall is presented in Figure 9.

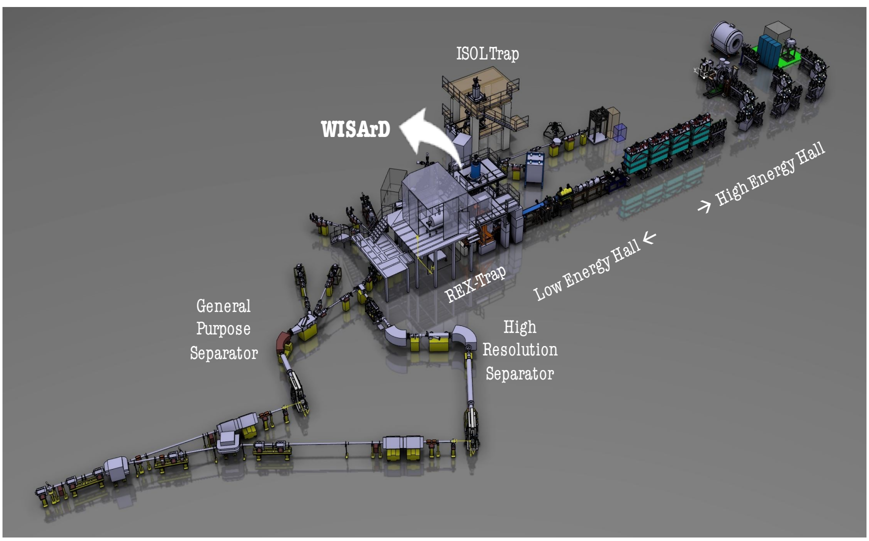

Figure 9. Part of the ISOLDE Hall layout. The Hall is conveniently split into two zones for experiments with respectively low energy beams (up to 50 keV) and post-accelerated high-energy beams (up to about 10 MeV/nucleon). The WISArD setup is located in the low energy part and it is distinguished from the other experiments by being one of the two

platforms, in the drawing the WISArD magnet is shown in the center of the image in blue.

After the mass selection, a 30 keV $^{32}Ar^{+}$ beam is supplied into the WISArD beamline which is located in the low energy part of the ISOLDE Hall, next to the REX-ISOLDE setup, and spans roughly over a 10 m^2 area. The average $^{32}Ar^{+}$ production yield was estimated to be 1700 pps, about half of the standard capability quoted by the ISOLDE data yield [55]. The WISArD beamline can be described as consisting of two main parts: the horizontal (HBL) and the vertical (VBL) beam lines. In Figure 10, the layout of the WISArD setup is shown, with labels for some of the main components like the offline ion source in the HBL and the detection system located inside the superconducting magnet in the VBL.

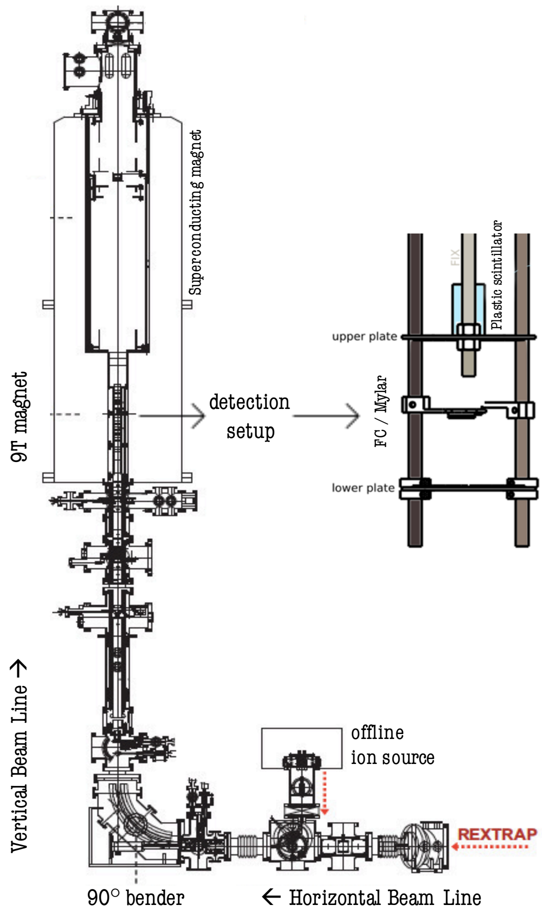

Figure 10. WISArD beamline. To describe fully the components on the beamline, it is splitted in two parts: the Horizontal beam line (HBL) compound from the REXTRAP valve to the 90º bender, and the Vertical

beam line (VBL) from the 90º bender to the top flange of the superconducting magnet.

The main purpose of the beamline is to drive as efficiently as possible the continuous ^{32}Ar beam of 30 keV until the detection zone. The detection setup is designed coaxially with the superconducting solenoid of 9T. In this region, the magnetic field lines are expected to be perfectly constant and homogeneous up to the about $5x10^{-5}$ level (according to a report of the Oxford Instruments company). The beamline houses the electrostatic ion optics elements and additionally is equipped with diagnostics tools, such as Faraday Cups (FC) and diagnostic apertures, which are compound of different collimator sizes and slits.

The HBL itself can be regarded as comprised by several sections: one part being before the 29º bender; another between the 29º and 90º kicker-benders; and finally, the one with the offline ion-source. HBL is equipped with four electrostatic elements: the deflector plates, Einzel lenses, steerers, and kickers. In addition, there are two diagnostics sets consisting of a small trolley which holds a FC and collimators of different sizes to monitor the quality of the beam. These tools are used to efficiently inject the ion-beam from the general ISOLDE beamline or from the WISArD offline ion source into the HBL and transport it with minimal losses to the VBL. Figure 11 shows the electrodes and diagnostic tools located in the HBL.

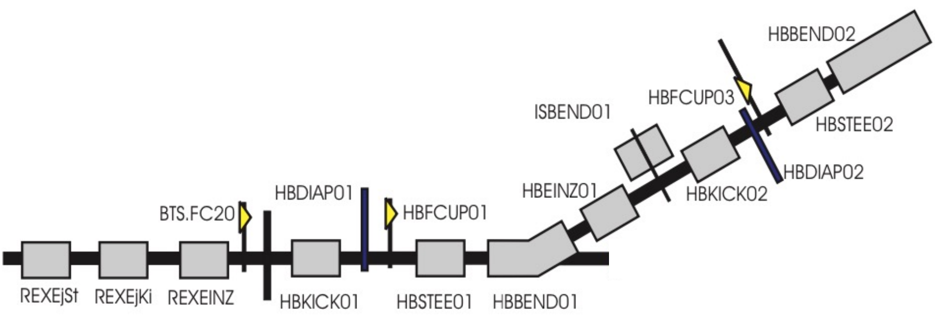

Figure 11. Horizontal beamline. The first four elements from left to right are REXEjSt for ejection steerer, REXEjKi for ejection kicker, REXEINZ for an einzel-lens electrode, and BTS.FC20 is the last Faraday cup used and controlled by the ISOLDE operators before the ^{32}Ar beam is delivered to the WISArD beamline. The name convention used for the beamline elements is presented in Table 3. Figure taken from Coeck [56].

The VBL spans over two floors (around 7 meters high) with the last section being covered by a superconducting magnet. A collimator installed just after the 90º kicker-bender electrode was used previously for the former WITCH experiment to ensure the proper bunch beam quality (emittance and divergence). For the WISArD experiment four additional diagnostics feedthroughs have been installed. Figure 12 shows the electrode elements and beam diagnostic tools hosted in the VBL.

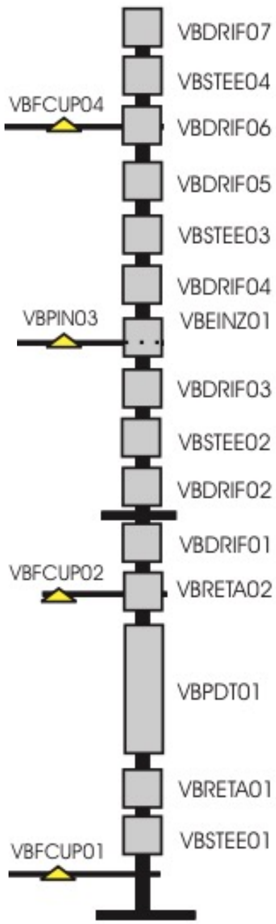

Figure 12. Vertical beamline. Sketch of the electrodes and the beam diagnostics presented in the VBL. The name convention used for the beamline elements is presented in Table 3. Figure taken from Coeck [56].

Note that the Pulsed Drift Tube (VBPDT01) was used in the WITCH experiment to retard the pulsed ion beam, no longer required for the WISArD experiment which use a continuous beam. In this case, the VBPDT01 is used as one more electrostatic ion component. For sake of convenience, the labels used by the former WITCH experiment remain to describe the components through the beamline and are presented in

Table 3. The high voltage values applied during the ^{32}Ar campaign can be found in Appendix B.

Table 3. Convention list used to describe the components in the WISArD beamline.

label	Function
HB	Horizontal beamline
VB	Vertical beamline
IS	Ion Source in HBL
KICK	Kickers
BEND	Benders
STEE	Steerers
EINZ	Einzel lens electrode
RETA	Retardation electrode
PDT	Pulse drift tube
DRIF	Drift electrode
FCUP	Faraday cup detector

In the following section, the attention is directed to the most important part of the WISArD setup, the detection system which is installed inside the superconducting magnet. A technical description of the beam transport, vacuum system, high voltage system as well its operation is given in Appendix B.

4.2. Detection system and superconducting magnet

Figure 13 shows the detection setup inside the superconducting solenoid capable to reach up to 9T magnetic field. The detection setup consists of eight 300-µm-thick silicon detectors of 30 mm diameter which are installed on two aluminum plates: upper and lower plates. These plates are positioned in a mirrored configuration having as a reference system the catcher foil at 65.5 mm from each silicon detector. The 65.5mm-distance is considered from the mylar foil to the silicon surface. In the same figure, the final view of the detection setup is also shown. The reference system is aligned with the geometrical center of the 9T solenoid, where the magnetic field is known to be constant and homogeneous.

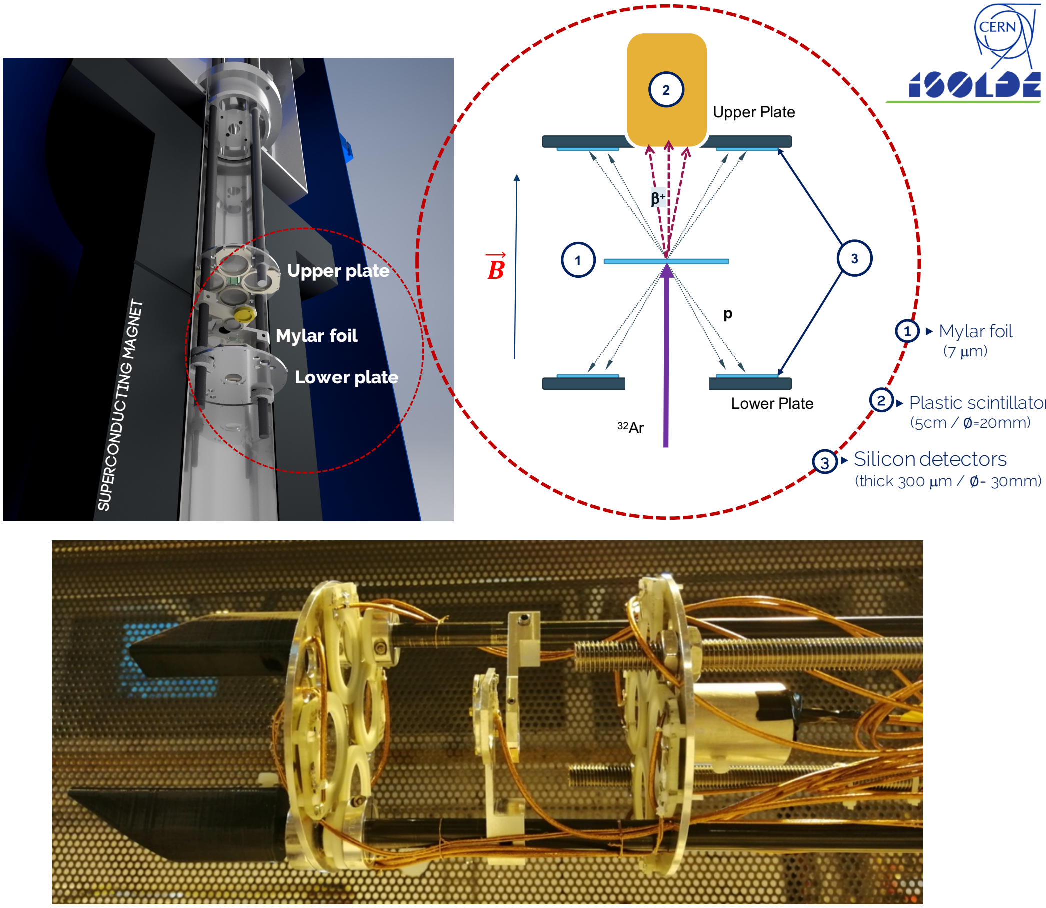

Figure 13. (top-left) Layout of detection setup inside the magnet. (top-right) Close-up to the setup used to detect the beta particles, β^+, and the protons, p. The distance between the upper and lower plate was set to 140 mm. (bottom) Final detection setup configuration.

The upper detection plate holds four silicon detectors labeled Si1U to Si4U and a plastic scintillator (BC408) of 20 mm diameter and 50 mm length coupled to a silicon photomultiplier (see figure 14). In a mirror configuration, four additional silicon detectors are located in the lower plate labeled as Si1D to Si4D. Note that there is no plastic scintillator located in the lower plate. Instead, the ^{32}Ar beam goes through the 20 mm aperture to be implanted in a 15-mm-diameter and 7-micrometer thick aluminized mylar foil. The bias voltage value used for the silicon detectors was +35 V and for the SiPM +54 V. The performance of both detectors are summaries in Appendix D.

The detection setup also includes two rotatory rods that can be controlled from outside the magnet. On the first rod a two-position arm is attached. The first arm-position allows to place the mylar foil in which the ^{32}Ar activity is implanted right in the center of the reference system while the second position places a Faraday cup in the same position to measure the intensity of the beam. The second rod hosts an alpha source (^{208}Po) used for energy calibration, which is always covered by two aluminum plates if not in use (see Figure 14).

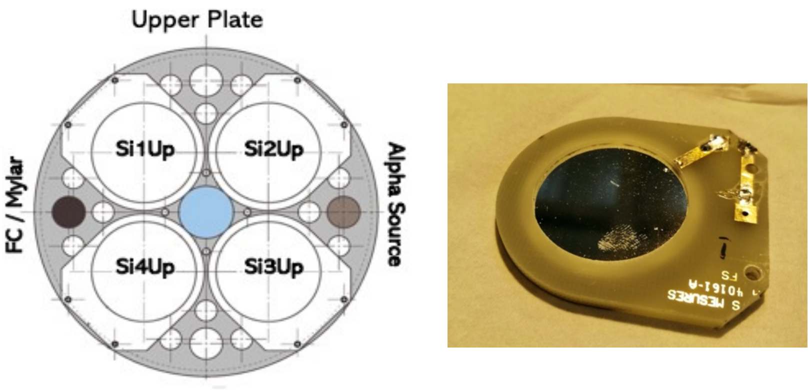

Figure 14. (left) Layout (front view) of the upper plate used to locate the protons and positron detectors. In the center, in blue, the 20 mm-diameter plastic scintillator is shown. The same configuration of silicon detectors is used for the lower plate, no plastic scintillator is located on it. (right) One of the eight identical silicon detectors is shown.

The eight silicon detectors and the plastic scintillator were read out by the FASTER data acquisition system, developed by LPC CAEN [57]. This is a high-performance, modular digital acquisition system based upon a synchronized tree model. It is a triggerless system that records time-stamped events. The latter are used in the subsequent offline data analysis to build energy spectra and investigate coincidences between emitted beta particles and protons. FASTER was equipped with two four-channel ADC modules, MOSAHR, to digitize and record proton events. Besides, a 2-channel QDC-TDC module, CARAS, was used to record the beta signals. The recorded data is split into several RUN files, reflecting various conditions such as magnetic field value, radioactive beam-implanted or calibration and background measurements. Details of the run files recorded during the beamtime can be found in Appendix C.

4.3. ^{32}Ar campaign

The experiment was scheduled in November 2018, just before the long shutdown at CERN (December 2018 - April 2021). Two out of three requested days were used, leading to an effective beamtime of about 2600 min or 1.8 days. In this period, the production of ^{32}Ar ions was estimated to be on average 1700 pps considering 20% transport efficiency through the WISArD beamline. The latter value is estimated by considering the current transmission measured from the Faraday cup BTS.FC20 (see Figure 11) to the Faraday cup located in the detection setup. The production yield is by a factor of 2-3 lower than the ISOLDE standard capability [55]. The ^{32}Ar beam is implanted in the first micrometer of the bottom surface of the aluminized mylar foil where the decay happens. Then positrons and protons escaped from the mylar following the magnetic field lines of 4T. The intensity of the magnetic field was chosen such that the curvature radius of the positrons is less than the radius of the plastic scintillator and the size of the beam spot. In this sense, positrons emitted upstream are guided towards the plastic scintillator positioned in the upper plate with a 100% efficiency. The radius of curvature for protons of 3 MeV is approximately 7 cm giving a total detection efficiency of 8% for a single proton detector due to the solid angle covered by the proton detectors.

5
Data Analysis

"No one can explain something better than how they understand it". -Anonymous

The present chapter includes a description of the detailed energy calibration of the silicon detectors (proton detectors), of the fitting procedure, and of the energy losses suffered by the protons before reaching the silicon detectors. The energy calibration of the plastic scintillator (positron detector) is also described. To conclude, the proton-energy shift value is determined by choosing those protons that are detected in coincidence with the beta particles either in parallel or antiparallel direction.

5.1. Calibration: silicon detectors

The precision that can be achieved in the current study strongly depends on the energy resolution of the silicon detectors. Since the maximum proton energy shift between various kinematic conditions is in the order of a few keV, one needs to calibrate these silicon detectors carefully so that the energy determined from experiment is not biased. To do this, online radioactive beams of ^{32}Ar and ^{33}Ar were used as calibration sources, making use of their strong beta-delayed proton emission probabilities. Overall, seven (ten) proton peaks emitted following the beta decays of ^{32}Ar (^{33}Ar) were used in the calibration. Proton energy values in the decay of ^{32}Ar and ^{33}Ar were determined by Blank et. al. [50] and Adimi et. al. [51], respectively. The proton energies relevant to this analysis are summarized in Table 4. A partial decay scheme of the ^{32}Ar decay is shown in Figure 15, showing the excited states in the beta decay daughter from which the proton energy listed in Table 4 originate, as well as the energies of these proton peaks to the respective ^{31}S grand-daughter isotope.

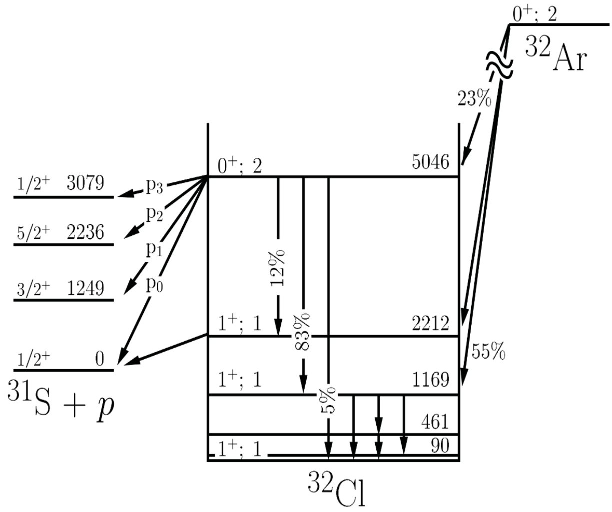

Figure 15. Partial decay scheme of the ^{32}Ar decay. Updated values can be shown in Blank et. al. [50]. The labels p_0, p_1, p_2, and p_3 are proton lines following by an unbound proton state of the daughter nuclei (^{32}Cl) from the beta decay.

Table 4. Summary of proton energies in the laboratory frame and absolute branching ratios from ^{32}Ar and ^{33}Ar decay used to calibrate proton detectors in this work. Proton lines attributed by [50] and [51], respectively.

Isotope	Proton energy [keV]	BR(%)
^{32}Ar	2121.7(31)	3.621(67)
	2421.8(29)	7.236(110)
	3356.0(7)	20.508(166)
	3988.6(36)	0.19(10)
	5555.5(45)	0.112(5)
	5832.1(53)	0.087(7)
^{33}Ar	1320.5 (30)	0.168(9)
	1642.8 (4)	0.411(20)
	1779.7 (4)	0.471(22)
	2096.4 (4)	2.73(12)
	2480.4 (20)	0.362(17)
	3172.1 (6)	31.0(14)
	3857.2(20)	0.735(34)
	5046.8 (20)	0.224(12)

5623.7 (30)	0.124(7)
5726.5(30)	0.092(5)

The energy calibration takes into account the energy loss in the about 1290-nanometer (see below) dead layer of the silicon detectors and the mylar implantation foil, see Figure 16. To simplify the analysis, it is assumed that all silicon detectors have the same dead-layer thickness, and only protons traveling upward (detected by the upper silicon detectors) experience strong energy loss due to the mylar foil, since the implanted ions are stopped just in the first μm at the bottom surface of the mylar foil. Thus, the energy calibration is determined in a two-step process.

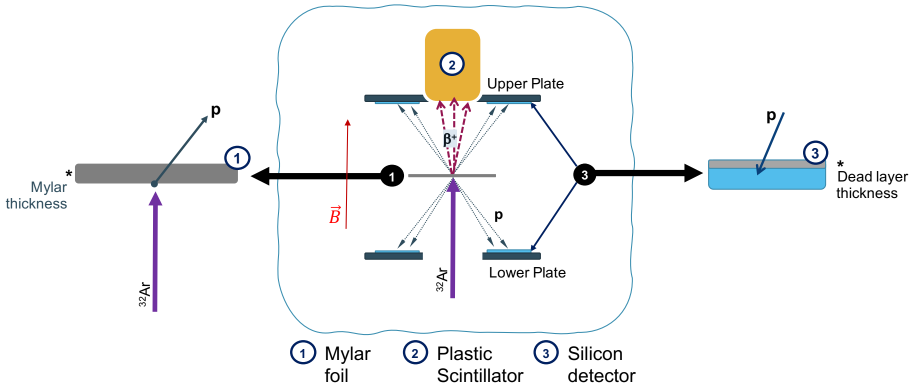

Figure 16. Sketch of the detection system (center) and the sources of proton energy losses. (left) Close-up to the mylar foil. Protons travelling to the upper detectors experience an energy loss due to the mylar foil thickness. (right) Close-up of a silicon detector. For each silicon detector, an energy loss due to the dead layer has to be considered.

The first step is to determine the energy calibration for the SiD-detectors, in which the proton deposited energies are not affected by the energy loss due to the mylar foil thickness. This will help us to determine the dead-layer thickness simultaneously with the energy calibration parameters for the SiD detectors. As all silicon detectors were produced in the same production process (by the company Eurisys Mesures (40161-A FS)) we suppose the dead layer to be the same for all eight detectors. Once the dead layer thickness is determined for the SiD detectors, this is assumed equal for the SiUs. As a final step, the energy calibration parameters for the SiU-detectors and the mylar thickness are determined.

In both steps, the procedure to determine the energy calibration parameters and energy losses for each set of four silicon detectors could thus be inferred from the best fit of the data by varying nine parameters; two related to the energy calibration parameters i.e., slope and intercept, and one more parameter linked to the energy loss that protons suffer to travel through the materials. These parameters are introduced to an adapted χ^2minimization function from a ROOT(MINUIT) class in order to determine the parameters simultaneously [58]. The following equation presents in general the function to be minimized,

$$E_{cal} = Cx + y + \int \frac{dE}{dx}\, dx \tag{5.1}$$

where E_{cal} is the calibrated proton energy. In this analysis, the calibrated energy is assumed to be linear with x and y being the slope and intercept, respectively, C is the mean value for each peak. The proton stopping power, dE/dx, depends on the matter (silicon and mylar) through which the proton travels, with dx is the mass thickness, expressed by $dx = \rho d\tau$, where ρ and $d\tau$ are the density and thickness of the material, respectively. The pstar NIST tables [59] were used as a reference.

The accuracy with we can extract these parameters from the data depends on our knowledge about the shape of the peak and background. The following subsections describe the detailed procedure of each step.

5.1.1. Down plate: SiD

The proton spectra presented in Figure 17 show the information obtained during the November 2018 campaign for ^{32}Ar (top) and ^{33}Ar (bottom). Because the proton histograms are similar for all four SiD detectors, for the sake of simplicity, only Si1D is shown here. The remaining information about the proton spectra can be found in Appendix D. Proton peaks used in the energy calibration are indicated in the histograms, in blue proton peaks related to GT transitions and in orange peaks related to the superallowed F transition.

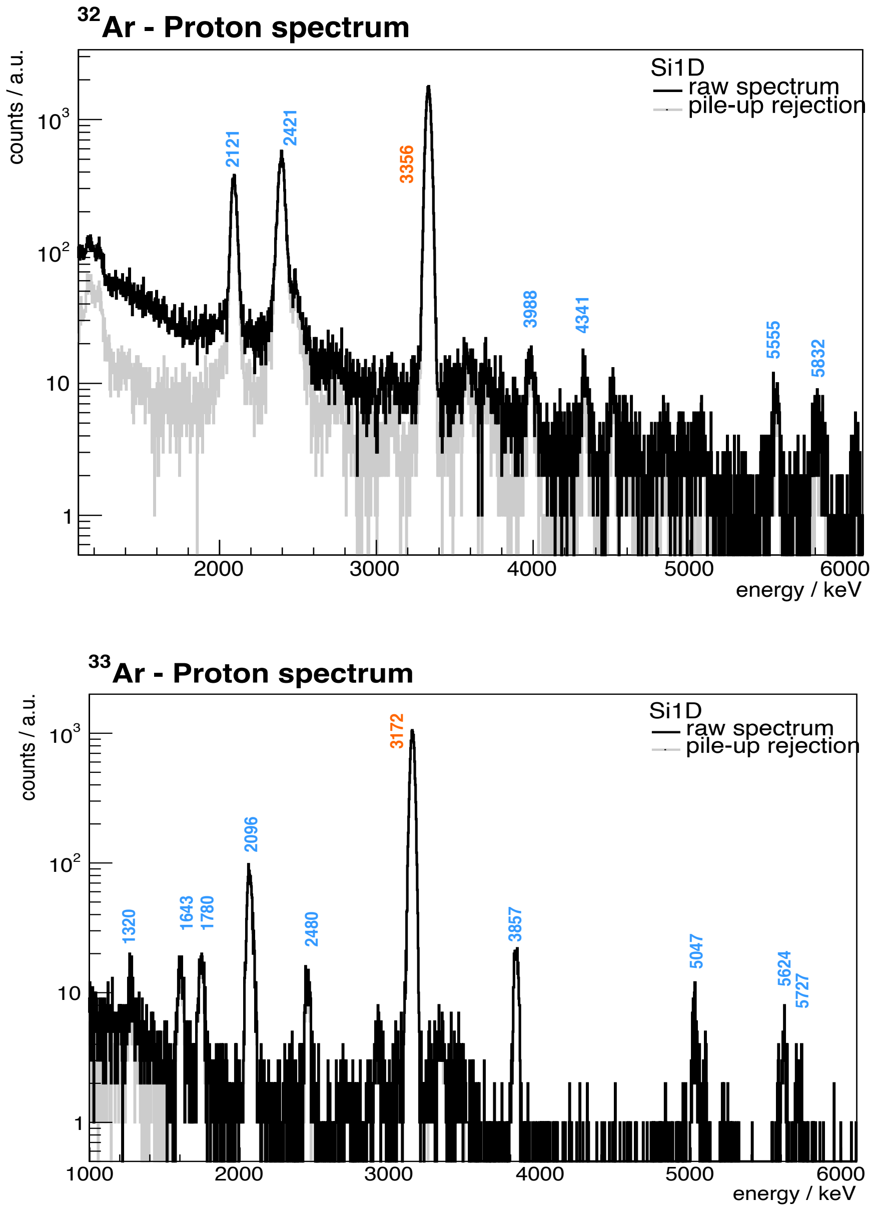

Figure 17. Spectrum of beta-delayed protons from the decay of ^{32}Ar (top) and ^{33}Ar (bottom) measured in the proof-of-principle WISArD campaign. Labels in both spectra indicate the proton peaks and their energy used to calibrate the eight silicon detectors.

The DAQ software has a pile-up flag that informs about the validity of the data. If two signals are detected within a time window in the same silicon detector, their waveforms overlap. These events are piled-up and the flag returns a 1. If the flag returns a 0, only one signal is detected and accumulated, i.e., pile-up free.

The pile-up window was set to 300 ns. This means that if a second event starts within 300 ns of the first one, it will be identified as a pile-up. Only when the second event starts after these 300 ns, it will be properly counted (as it should). The spectra with and without pile-up rejection are also compared in Figure 17 for both isotopes, ^{32}Ar (top) and ^{33}Ar (bottom). This procedure reduces possible background contributions giving a cleaner spectrum with a proper estimation of the count rate for each proton peak.

As an example, a close-up of the proton lines at 2121 keV and 2421 keV following GT transitions (see Figure 18) and at 3356 keV following the super allowed F transition are shown in Figure 19. It is clear that pile-up rejection does not affect the proton peaks shape, but only suppresses background, improving the signal-to-background ratio. The pile-up rejection condition is applied to all proton spectra used in the data analysis.

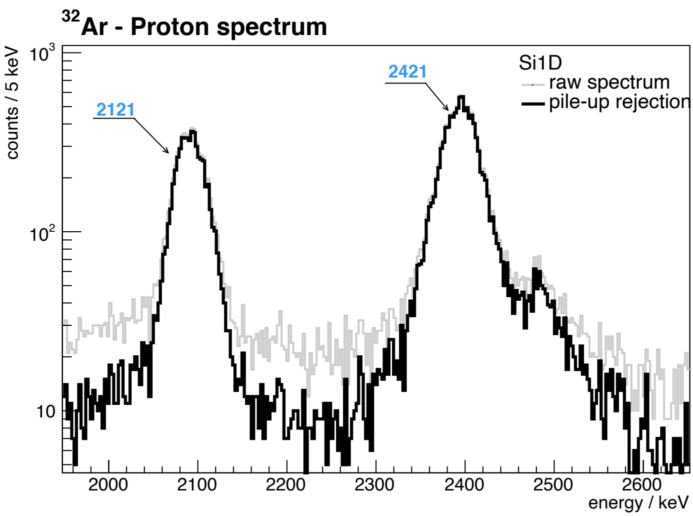

Figure 18. Proton peaks at 2121 keV and 2421 keV following the two prominent GT transitions. The average energy resolution for these peaks is 36 keV and 45 keV, respectively.

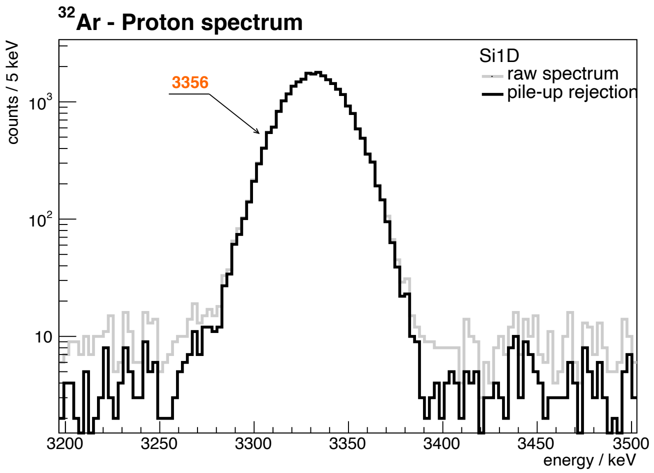

Figure 19. Energy distribution of the 3356 keV protons following the pure F transition of ^{32}Ar. The energy resolution is 30 keV. The pile-up rejection does not affect the proton peak but suppress background, improving the signal-no-background ratio.

Without any condition applied to the raw proton spectrum, other than the pileup-rejection, the kinematic energy shift shown in the proton distribution is isotropic. Consequently, by looking at the centroid of the peak, the shape to the left or right will look the same. Therefore, the best description to fit the data is a Gaussian function. The data is fitted in a region around the proton peak using a Gaussian and a linear function, the latter to determine the background counts under the peak. Figure 20 shows the fitting region for the superallowed F transition.

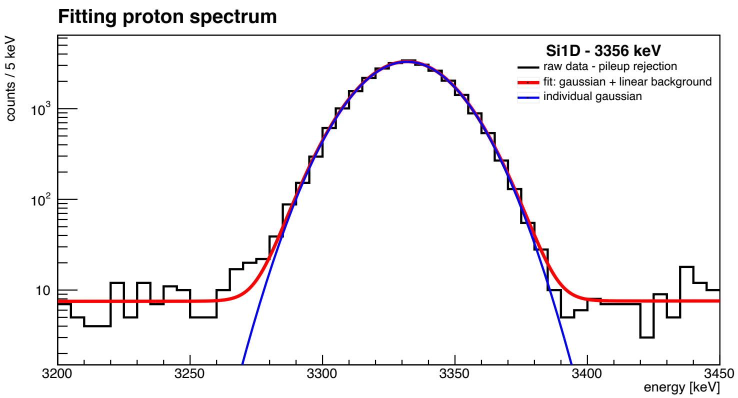

Figure 20. Fitting region for the superallowed Fermi transition. In red, the symmetric-gaussian plus a linear background fit is presented. The entire fitting region is shown here.

Figure 21 shows a special case where the previous assumption does not apply. Here the two proton lines at 2421 keV and 2510 keV are too close to each other to be fitted separately. In this case, a two-gaussian fit plus a linear background is used to determine precisely the mean value of the prominent peak at 2421 keV.

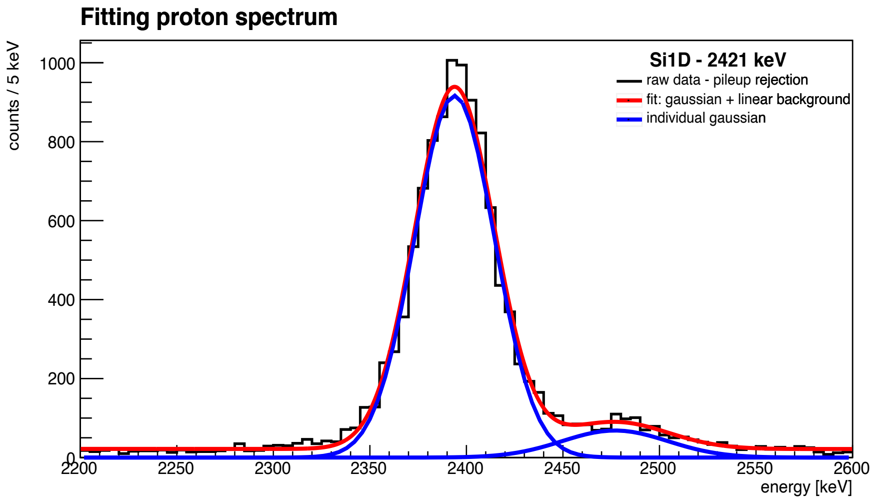

Figure 21. Fitting procedure used for the special case where two proton lines are too close to each other to be fitted independently. In this particular case, two Gaussians were used to get the mean value for the prominent peak at 2421 keV. The entire fitting region is shown here.

Three main parameters from the fitting routine will be of interest throughout this analysis. (i) The mean value, C, (channel number of the center of the proton peak) which is linked to the proton energy from literature, (ii) area under the proton peak (or integral value), **A**, which gives information about the number of protons emitted with the particular energy of the peak center, and (iii) width of the peak, **w**, which is commonly used to measure the energy resolution.

The procedure of χ^2 minimization for a set of four proton detectors requires in total nine parameters to optimize, i.e., two parameters related to the energy calibration (slope and intercept) per detector, resulting in 8 parameters plus the parameter corresponding to the dead layer thickness, *DL*, which is constructed using Eq. 5.1, and can be rewritten as:

$$E_{cal} = Cx + y + E_{loss}|_{DL} \qquad \textbf{(5.2)}$$

Figure 22 shows the proton stopping power in silicon, with the vertical lines defining the region where the proton energies are concentrated for the analysis of the experiment discussed here.

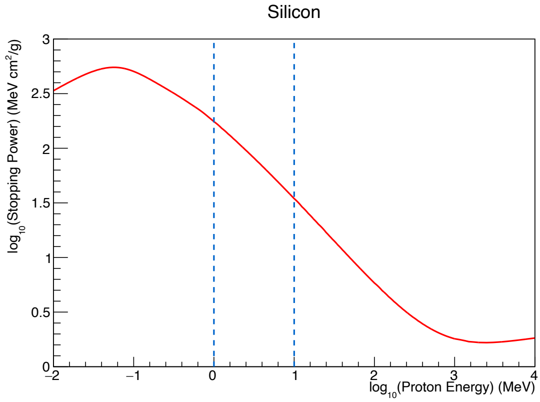

Figure 22. Proton stopping power (dE/dx) in silicon used to determine the dead layer of the proton detectors. The dotted lines mark the proton energy range from 1 to 10 MeV used in this experiment.

The difference between E_{cal} and the proton energy from literature, E_{lit}, used in this χ^2 minimization will be discussed later. The smaller the value of the χ^2 function, the better the parameters fit the data. Mathematically, the χ^2 function can be written as:

$$\chi^2 = \sum_{i=1}^{4} \frac{(E_{lit}-E_{cal})^2}{\delta E_{lit}{}^2+\delta E_{cal}{}^2} \qquad \textbf{(5.3)}$$

where i runs over the number of silicon detectors situated on each plate and δE is the uncertainty related to the energy, either from literature or the calibrated one. Table 5 shows the parameter values that best fit the data for the SiD analysis.

Table 5. Optimal calibration parameters for proton detectors in the lower plate and dead layer thickness value.

Detector	slope [keV]	intercept [keV]
Si1D	0.52352 ± 0.00038	-36.2 ± 4.4
Si2D	0.54922 ± 0.00039	-49.1 ± 4.5
Si3D	0.55838 ± 0.00041	-24.6 ± 4.5
Si4D	0.45336 ± 0.00033	-24.5 ± 4.6
Dead Layer thickness * Silicon detectors of 300-µm-thick		1290(120) nm*

The dead layer thickness in the silicon detectors causes a small energy shift (roughly 10 keV) of the proton peak with respect to the mean incident energies.

5.1.2. Upper plate: SiU

A similar procedure is used for the silicon detectors located in the upper plate, where a larger proton energy loss has to be considered since the protons in this case have to travel through the mylar foil causing a shift in the proton energy distribution. As shown in figure 23, the main proton peaks for ^{32}Ar (top) and ^{33}Ar (bottom) are shifted towards lower energy and weaker background peaks are perceptible at the expected position without mylar interaction. The resulting background peaks come from the decay of ^{32}Ar ions that were not implanted on the mylar foil. These protons were then either emitted directly towards the upper detectors by ^{32}Ar ions implanted on the walls and on the setup structure or by outgassing ^{32}Ar atoms. Indeed, being a noble gas Argon ion can diffuse from the region close to the foil surface and then leave the foil.

In the following figure, we show in blue the protons following a GT transitions and in orange those following the superallowed F transition. An asterisk is used to point out the background peaks and cases of study in this analysis.

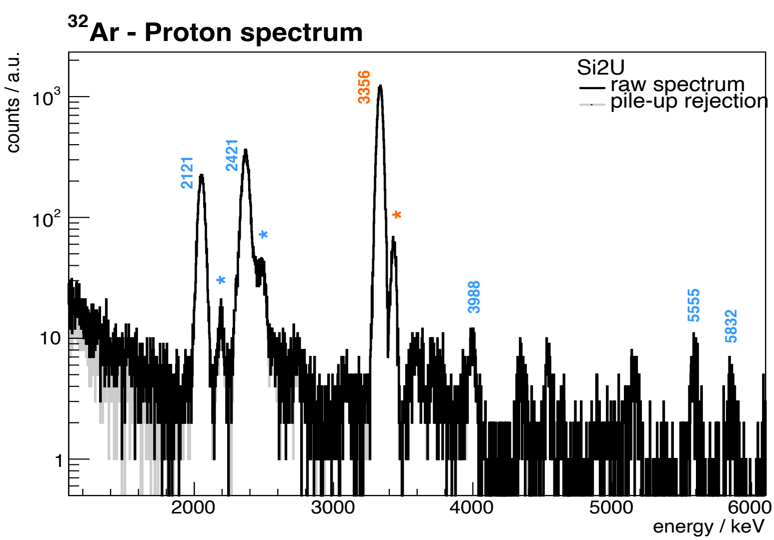

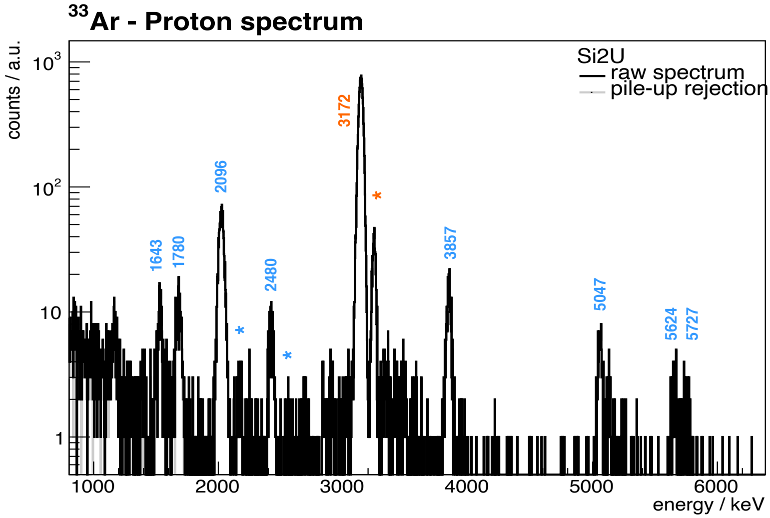

Figure 23. Proton energy distribution for (top) ^{32}Ar and (bottom) ^{33}Ar for one out of four upper-silicon detectors.

The energy calibration for the SiU detectors involved nine (twelve) proton peaks emitted following the beta decays of ^{32}Ar (^{33}Ar) including the background peaks. The fitting procedure consists of using in specific cases a two gaussian distribution (proton peak and background peak) plus a linear background to determine the centroid of the noticeable peak. The plots in Figure 24 illustrate the fit for the proton distribution 2421 keV (top) and the 3356 keV (bottom) transitions.

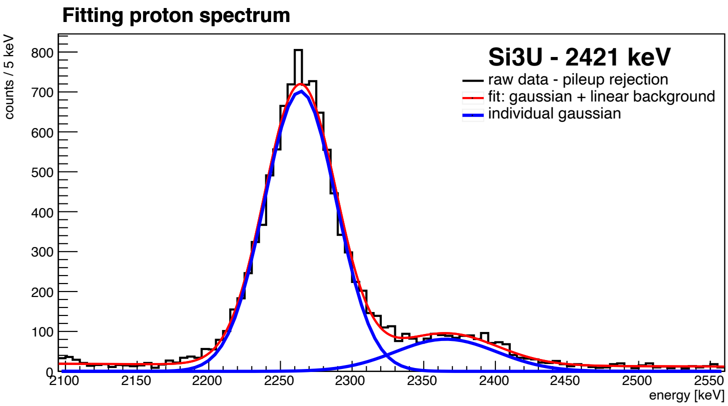

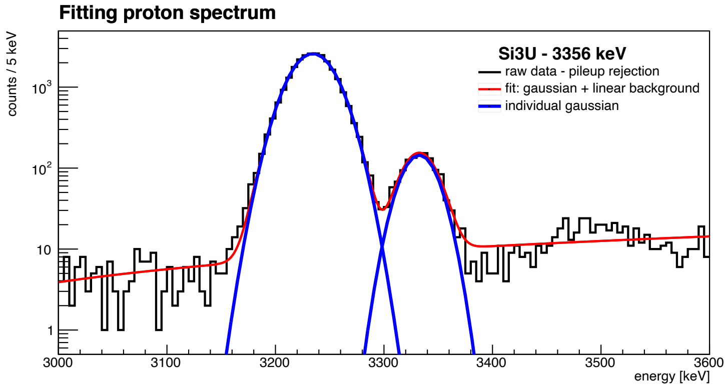

Figure 24. Fits of the proton peaks at 2421 keV (top) and 3356 keV (bottom). The peak at left is the peak shifted by the energy loss of the proton while traveling through the mylar foil. The peak at right is the (unshifted, i.e., with the original energy) background peak, coming from ^{32}Ar ions not decaying in the mylar foil (*see text*). The average energy resolution is 55 keV-FWHM for the 2421 keV peak and 40 keV-FWHM for the 3356 keV line. In both scenarios, a double gaussian was considered to get a precise centroid value of the prominent proton distribution.

For the upper proton detectors, the calibrated energy E_{cal}, in equation 5.1, can be written as:

$$E_{cal} = Cx + y + E_{loss}|_{DL} + E_{loss}|_{mylar} \quad \textbf{(5.3)}$$

where the energy loss due to the dead layer thickness is assumed to be equal to the one obtained for the SiD detectors and $E_{loss}|_{mylar}$ is the energy that the protons lose on their travel through the mylar foil. Mean energy losses were determined by the pstar NIST table [59]. Figure 25 presents the proton energy region that is used in the analysis.

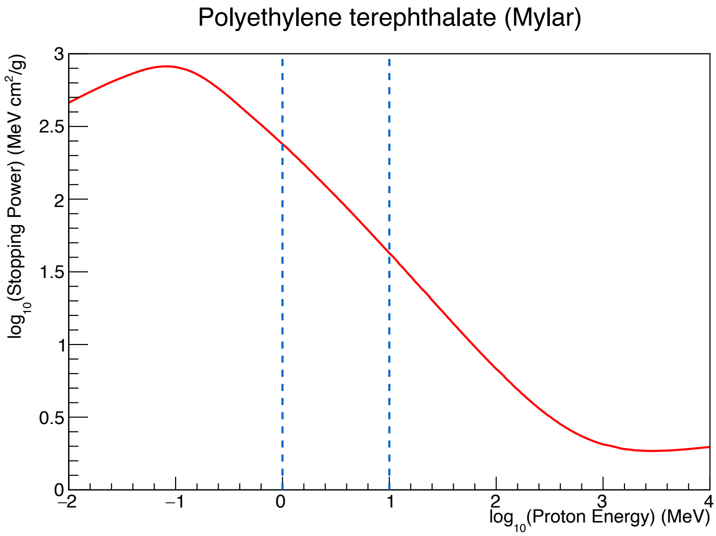

Figure 25. Proton stopping power (dE/dx) in mylar used to determine the energy loss due to the interaction of protons with the mylar foil. The dotted lines mark the proton energy range from 1 to 10 MeV used in this experiment.

The χ^2 minimization function has the same mathematical expression as equation 5.3. Table 6 summaries the obtained values from the minimization function.

Table 6. Summary of the optimal calibration parameters for proton detectors in the upper plate and the mylar thickness obtained by the chi-squared minimization function.

Detector	slope [keV]	Intercept [keV]
Si1U	0.45584 ± 0.00020	-20.5 ± 1.5
Si2U	0.46798 ± 0.00020	-35.1 ± 1.5
Si3U	0.44181 ± 0.00020	-34.1 ± 1.6
Si4U	0.47416 ± 0.00022	-14.9 ± 1.6
Mylar thickness		6937(700) nm

The uncertainty on the mylar thickness is set to a conservative 10% due to the different assumptions made in the fitting analysis, such as all proton detectors having the same dead layer thickness and all protons detected in the upper plate feeling the same effective thickness of the mylar. The energy loss that all protons detected in the upper hemisphere experience due to the 6937(700)-nm-thick mylar foil is about 100 keV. The uncertainty in the linear slope of the calibration for all eight silicon detectors leads to 0.3% and is dominated by the energy losses in the dead layer.

Residual energy calibration

To get a sense of how accurate the χ^2 minimization function is, the proton energies from literature [50] are compared to the values obtained from the calibration fit. Each point in the regression plot (showing the differences between the literature value and the fit value for each proton peak) shown in Figure 26 is related to a specific proton peak for each silicon detector located in the lower plate. For viewing purposes in the plot, data points from each silicon detector have been shifted slightly from the actual proton energy. From the figure it is evident that the calibration is quite successful, with the energy difference being smaller than ±10 keV for ^{32}Ar and ±20 keV for ^{33}Ar keV. The plot reveals, on the other hand, significant differences among different proton energy intervals. For the higher energy differences are clearly larger, which is related to the limited number of statistics (see Figures 17 and 23).

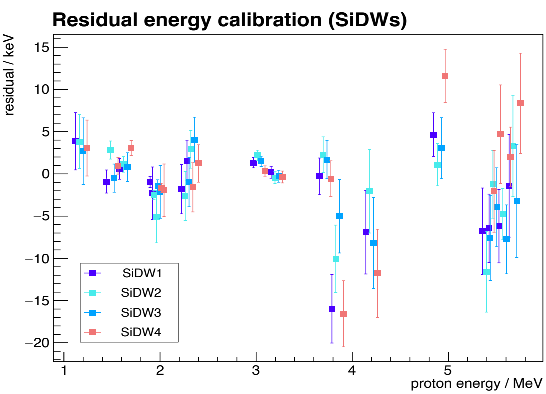

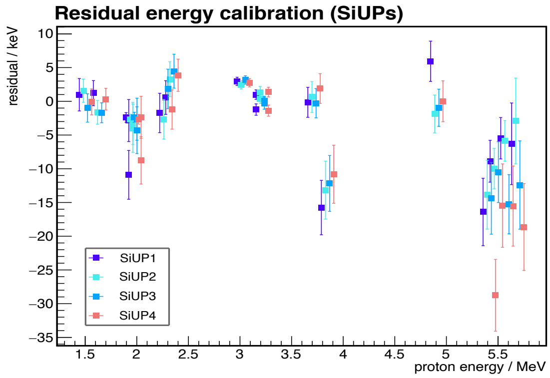

Figure 26. Residual plot for each silicon detector located in the lower (top) and upper (bottom) plate. The proton energy is slightly shifted for visualization purposes.

5.2. Coincidence measurement

Until now, proton events without any constraints, defined as singles, have been studied. The singles measurements can be used as a reference for extracting the mean kinematic energy shift because it preserves the isotropic proton emission, thus affecting only the broadening of the proton energy distribution, but not the central value of the peaks. Furthermore, the geometry of the detection setup allowed coincident proton-beta events to be detected in parallel or antiparallel emission. By imposing a coincidence requirement new information related to the shape and width of the proton energy distribution is obtained.

Kinematic energy shifts have been directly evaluated for each beta-delayed proton group as a function of the beta-particle emission direction. In this work, with only one beta detector being available, the case when the positrons are emitted upwards (upper plate) is only analyzed. Two possible coincidence scenarios could be considered. The first is by choosing the protons that are detected in the same direction as the beta particle (both particles going upwards, parallel direction), and the second scenario is by choosing the protons detected in the opposite direction of the beta particle (antiparallel; protons detected in the lower plate). In comparison with other techniques, the method used here has the advantage that the positrons are immersed in a strong magnetic field so that they are deflected from their original direction spiraling in a continuous curve around a central point on the beta-detector plane. The advantage becomes all the more significant when signals from the beta and proton detectors are found within a trigger

time, T_{diff}. Afterwards, coincidence spectra can be produced from this by choosing protons detected in either hemisphere, parallel or antiparallel to the beta direction.
The calibration of the plastic scintillator is carried out by matching the beta end-point energy between the experiment and GEANT4 simulations. In these simulations, the Fermi beta transition is used as a reference and coincidences between the protons and beta particles from this superallowed transition are considered. In order to determine the detection threshold, Monte Carlo simulations with GEANT4 were performed as well. Figure 27 presents the deposited energy spectrum of the F transition in the plastic scintillator found experimentally and compared with the simulations.

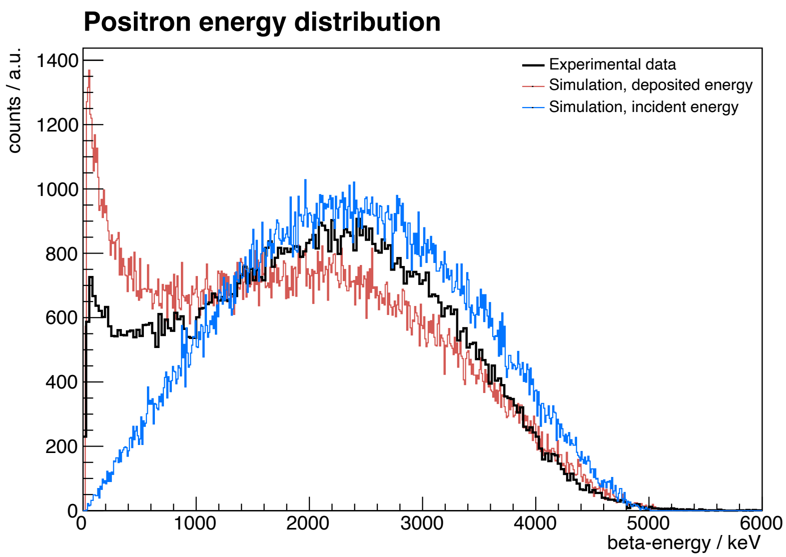

Figure 27. Incident (blue line) and deposited (red line) positron energy distributions given by the simulation compared with experimental data (black line) for the F transition.

Due to limited knowledge of the response function of the plastic scintillator, the detection threshold was estimated to be 25(12) keV with a conservative 12 keV uncertainty. It is important to point out here that the limited knowledge of the detector response function of the plastic scintillator led to a considerable uncertainty in the threshold determination.

As mentioned, the positron being immersed in the strong magnetic field experiences a centripetal force. This will make the beta particle spiral along the magnetic field thereby resulting in the helical path of the particle. Some of these trajectories result in positrons reaching the detector with a very large incidence angle (grazing), increasing the backscattering probability on the plastic scintillator. In addition, the beta-particle may not be fully stopped in the plastic due to its small size, thereby also contributing to the background events. The GEANT4 simulation shown in figure 27 reveals that around 30% of the positrons escape from the detector's sensitive volume, a fact that leads to a non-detection of a fraction of the energy of the positrons initially emitted in the upward direction. In Section 6, a detailed study on the sensitivity to backscattering effects is performed.

It should be noted that since in this study the beta-neutrino angular correlation was determined from the kinematic energy shift of the protons, the energy of the positrons does not play a direct role in the extraction of $a_{\beta\nu}$. The main purpose of the beta detector is thus to use it as a trigger to perform coincidence measurements.

The selection of coincidences for the proton groups is depicted in Figure 28. The horizontal axis shows the time difference (in ns) between plastic and silicon detectors in coincidence events. After choosing the T_{diff} condition for proton-positron coincidences detection, we performed an analysis within a narrow energy window for each proton group. In Figure 28 an example is shown for the case of the proton distribution at 3356 keV following the F beta transition. The energy window (vertical axis) was determined by its centroid at 3356 ± 100 keV. The events outside the T_{diff} window might occur as a result of noise or a coincidence with low energy particles deposited in both detectors. A proper T_{diff} selection is thus required to reduce these false coincidence events. To quantify its influence on the analysis, first a strict (approx. 15% of the total of 600 ns T_{diff} window) and then a soft (approx. 30%) coincidence T_{diff} window were probed to select true coincidences events. Both choices led to the same final results for the contribution of false coincidences. Events outside this T_{diff} window are less than 0.3% demonstrating the absence of any systematic error due to this T_{diff} selection on the resulting $a_{\beta\nu}$ value.

The coincidence spectrum is then conditioned by the time difference, T_{diff}, and the mean value of the proton peak is estimated within this region. Once a restriction on the directions of the positron and proton detection is imposed, the proton energy shape is expected to be asymmetric reflecting the kinematic-energy shift of the proton distribution.

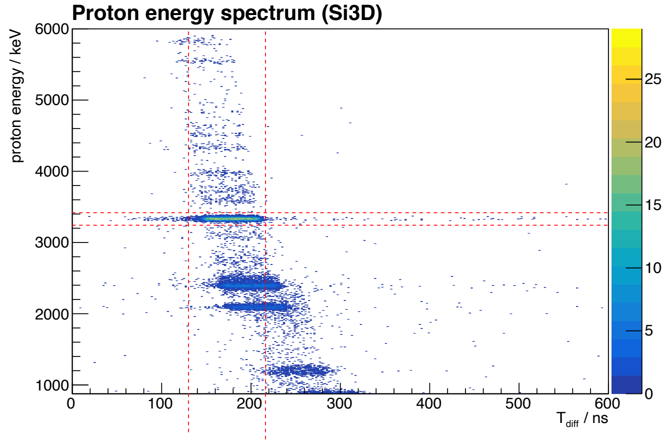

Figure 28. Proton energy spectrum vs T_{diff} for one of the lower detectors. The energy selection window is indicated by the horizontal dashed lines and the selected T_{diff} window is given by the vertical dashed lines. For each proton group T_{diff} is selected in order to reduce possible false counts. The proton following the Fermi transition is presented here as an example.

To avoid systematic bias from the asymmetric proton energy distribution, the mean energy of each proton energy peak in the coincidence spectrum is determined by an iterative procedure.

First, a Gaussian fit is used to get a rough estimation of the mean value. Thereafter, using this approximation, an iterative procedure is used by selecting events with a 3σ window centered on the mean energy obtained in the previous step. This method was favored compared with the use of fits because it does not depend on the shape of the proton energy distribution.

Since only positrons emitted upwards were detected, the data obtained for singles has to be scaled by a factor 0.5 to be easily compared with the coincidence spectrum. This is shown in Figure 29, where one of the proton detectors from the lower plate is used as an example.

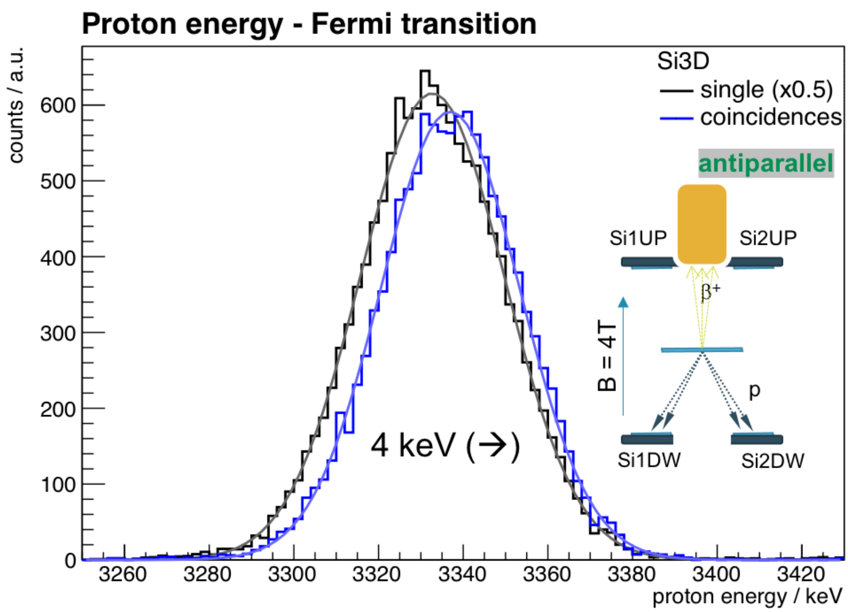

Figure 29. Coincidence (blue) and singles (black) measurements of the protons following the superallowed Fermi transition are presented using the data of one of the SiD-detectors. A clear shift in the mean proton energy is observed. The expected proton energy boost due to the recoiling nucleus is about 5 keV (average).

As was expected for the SiD-detectors, the extra kick in the proton energy due to the recoil energy of the beta-decay daughter nucleus is observed. The centroid of the proton energy in coincidences is shifted towards higher energy values (5 keV in average for the protons following the F transition) for each SiD-detector.

The analysis procedure for the SiU-detectors is similar to the SiD detectors. One only needs to adjust the proton energy region and the time window for the coincidence events accordingly to reduce background from false coincidences as was shown in Figure 28.

Figure 30 shows the resulting proton energy shift for the F-transition for one of the proton detectors in the upper hemisphere. As the detected protons travel in the opposite direction to the recoiling daughter nucleus (see figure 30), the proton energy shifts towards lower values for the upper detectors.

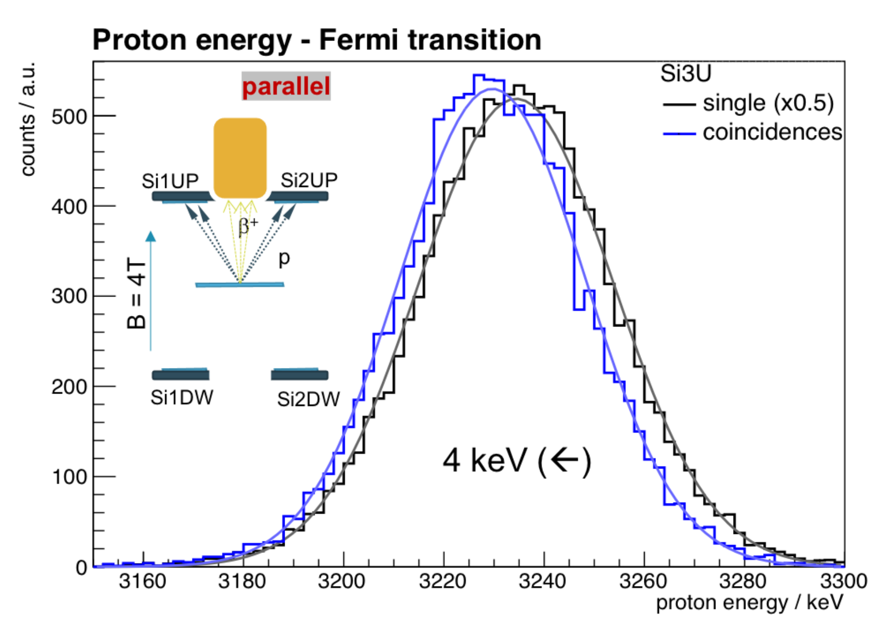

Figure 30. Coincidence (blue) and singles (black) measurements of the protons following the superallowed Fermi transition are presented using the data of one of the SiU-detectors. A clear shift towards lower energy (5 keV average) in the mean proton energy is observed.

An important remark to the shape of the proton peak is to be made here: in singles the proton energy peak is wider as a result of the isotropic emission relative to the recoiling beta-decay daughter. It is just after gating on positrons and protons emitted in a preferred direction when the proton shape becomes smaller making visible the kinematic energy shift. Although the delayed protons following a GT transition are known to have a smaller branching ratio compared to protons following the superallowed F transition a simultaneous analysis using these transitions is useful to check for systematic errors and the validity of the analysis. In the following, using a similar procedure as for the $0^+ \rightarrow 0^+$ Fermi transition, an analysis of one of the five $0^+ \rightarrow 1^+$ GT transitions channels with a strong branching ratio, is presented.

The same approach taken for the F-transition, i.e., measurements of the shift of the centroid values of the proton energy distribution for singles and coincidence spectra, are applied to the GT-proton distributions. The statistics in the proton distributions following a GT transition was not high enough to reach a precision on the beta-neutrino angular correlation sufficient for obtaining useful information for a possible weak tensor contribution. Nevertheless, the study of these proton distributions helps to track consistency of the analysis. Figure 31 shows the obtained proton energy shift for the prominent GT transition at 2121 keV. The top part of the figure illustrates the energy shift (about 3 keV) towards higher values for all SiD as it is expected for the protons boosted by the recoiling energy and the bottom part shows the energy shift (order of 3 keV for SiUs) towards lower proton energy. Notice that the same energy loss due to the mylar (about 100 keV) is also observed in the upper proton detector for this proton peak following a GT transition.

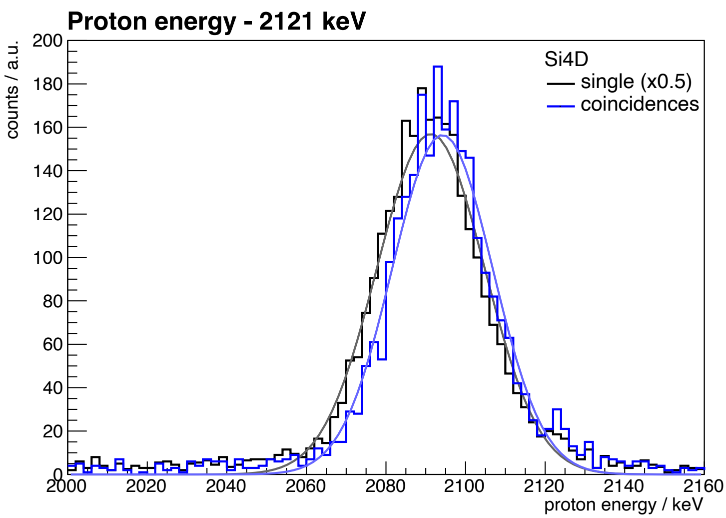

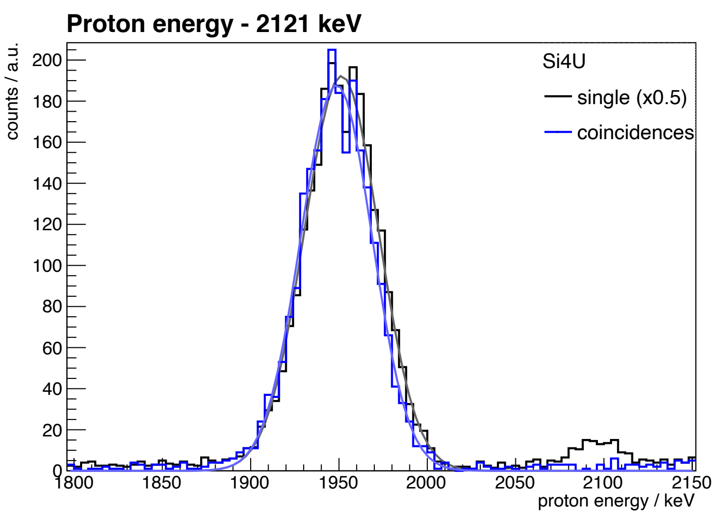

Figure 31. Coincidence (blue) and singles (black) measurement of the energy distribution of the 2121 keV protons following a GT transition. (top) Protons detected in the opposite direction to the positron direction. In this scenario, the difference between the centroids of singles and

coincidence events are in average +3 keV for the SiDs, as it was expected because the proton energy boost given by the recoiling nucleus. (bottom) Protons detected in the same direction to the positron direction leading to an average shift of -3 keV towards lower energies for the SiUs.

5.3. Kinematic-energy shift values

Kinematic-energy shifts were directly evaluated for each beta-delayed proton group from its mean value determined as a function of the beta particle direction and the direction of the emitted proton. As this technique relies on the mean-energy difference between singles and coincidence spectra, the influence of the proton detector response function and the intrinsic proton peak on the result is reduced compared to when the beta-neutrino correlation is deduced from the broadening of the singles proton peaks (as was done in refs. [32], [33]). One more advantage of this technique is that it solves the problem of beta-events summing reported by Adelberger et al. [33], since the measurement of both particles is now done in different detectors.

Figure 32 shows the obtained values for the proton mean kinematic-energy shift, $\bar{E}_{shift} = |\bar{E}_{coinc} - \bar{E}_{single}|$ (absolute values) for all proton detectors, SiUs and SiDs for the F transition and one GT transition. The weighted average of the proton energy shift is represented by the solid line and statistical uncertainties by the dashed line. To show the compatibility of the results for all proton detectors a normalized χ^2 value is also presented in the figures. At the top, the proton energy shift for the F transition is presented. The weighted average value for this transition is 4.51(4) keV. A slight deviation of about 0.03 keV from the weighted average value (solid line) and the absolute value (red squares) is observed in each detector located in the down plate and about 0.1 keV for those located in the upper plate. At the bottom part, delayed protons at 2121 keV from a pure GT transition leads to a 2.96(7) keV weighted average value. In this case, the deviation between the absolute value (blue squares) and the weighted average (solid line) is within the error bars for all proton detectors.
From these results, it is clear that we lose sensitivity in the proton energy shift measurements due to the mylar (as seen by the larger error bars for the upper detectors). It is worth discussing these facts as is done in the next chapter where GEANT4 simulations are performed in order to study the sources of systematic effects.

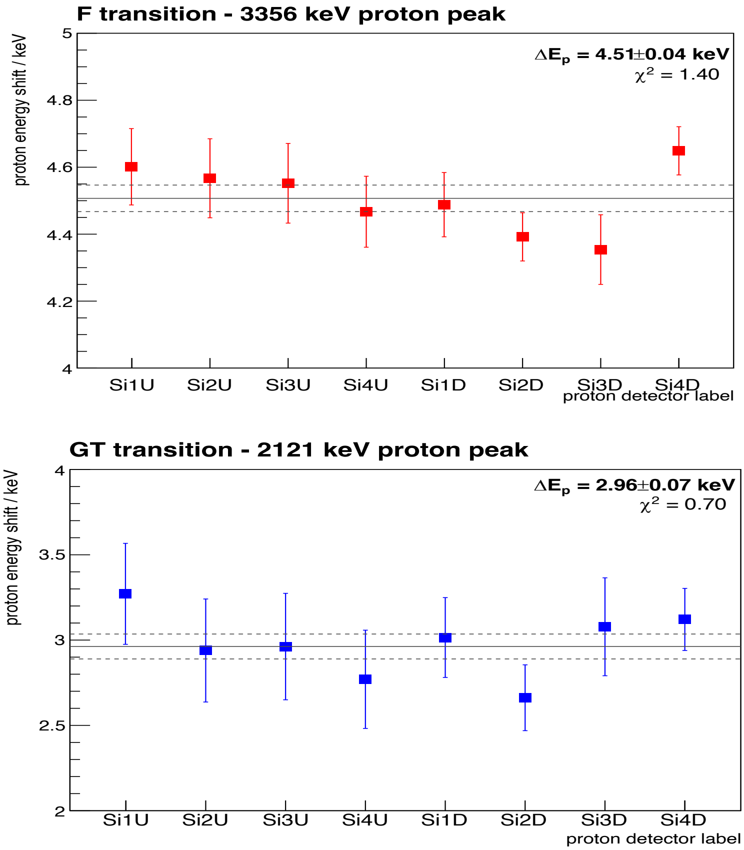

Figure 32. Kinematic-energy shifts for all silicon detectors (top) for the 3356 keV protons of the superallowed Fermi transition and (bottom) 2121 keV protons of a pure Gamow-Teller transition. Weighted averages values on the proton energy shift and statistical uncertainties are indicated by solid and dashed lines, respectively. The presented χ^2 value is normalized.

To estimate the uncertainty of the proton energy shift, we consider the number of counts (integral value) in the singles, N_S, and coincidence, N_C, spectrum. Since the coincidence spectrum is a portion of the singles measurement, the ratio between the counts present in each spectrum has to be considered in the statistical uncertainty. Mathematically, this can be written as

$$\delta\bar{E}_{shift} = \sqrt{\left(\bar{E}_{shift}^2 \Big/ N_s + \bar{E}_{coin}^2 \Big/ \frac{N_S}{N_C} \right)} \qquad \textbf{(5.4)}$$

where $\bar{\mathrm{E}}$ denotes the statistical errors for the proton energy shift ($\bar{E}_{shift}$) and of the proton energy in coincidence ($\bar{E}_{coin}$). The deduction of equation 5.4 can be found in Appendix A.

The study of the sensitivity of the proton energy shift was extended to the GT proton groups following the same analysis. Figure 33 shows the analyzed proton energies shift from the delayed protons at **(a)** 2421 keV, **(b)** 3988 keV, **(c)** 5555 keV, and **(d)** 5832 keV. As can be seen as the energy of the delayed protons increases, the statistics decreases, dispersing the weighted values of the nominal value, losing sensitivity at those energies.

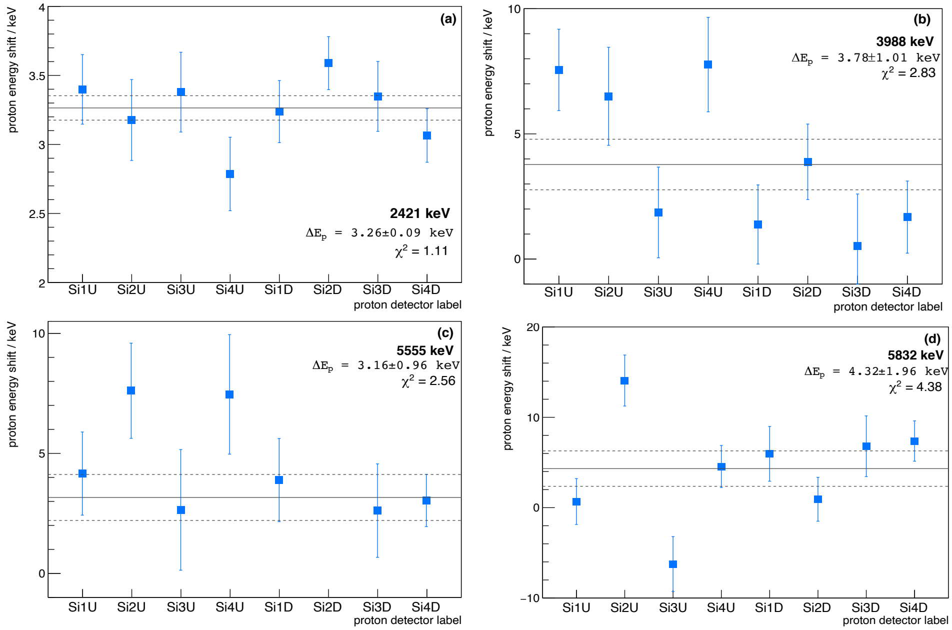

Figure 33. Extended study of the proton energy shift for proton groups following a pure Gamow-Teller beta transition. (**a**) 2421 keV, (**b**) 3988 keV, (**c**) 5555 keV and (**d**) 5832 keV.

Table 7 summary of all obtained proton energy shifts for all the studied transitions, with the superallowed F transition being highlighted as reference for further analysis.

Table 7. Proton energy shift values obtained for the six delayed protons.

Delayed proton energy [keV]	Proton energy shift [keV]
2121	2.96 ± 0.07
2421	3.26 ± 0.09
3356 ‡	4.51 ± 0.04
3988	3.78 ± 1.01
5555	3.16 ± 0.96

5832	4.32 ± 1.96

‡ Superallowed Fermi transition

6

The $a_{\beta\nu}$-value for Fermi and Gamow-Teller transitions

"An expert is a person who has made all the mistakes that can be made in a very narrow field." — Niels Bohr

Since the angular correlation coefficient, $a_{\beta\nu}$, determines the kinematics of the beta decay, it should be possible to extract its value from the measurements of the beta-delayed proton energy shifts. A customized event generator and Monte Carlo simulations were used to study the angular correlation distribution and the energy shift that should be observed from experiment. The correlation was found to be linear. By using the slope of the correlation and the proton energy shift obtained by the experiment a final value for the correlation coefficient can be determined.

Using the same simulations, we can not only extract the centroid of $a_{\beta\nu}$, but also study the systematic uncertainty in our system. All relevant systematic effects such as the geometry, the magnetic field, the distribution of the ^{32}Ar activity over the source surface, as well as scattering of the protons and positrons, are taken into account in the GEANT4 simulations. Last but not least, the uncertainties related to each systematic effect and their impact in the determination of $a_{\beta\nu}$ are studied.

6.1. Monte Carlo Simulation analysis

To interpret the proton energy shift as a measurement of the $a_{\beta\nu}$ values for the different beta decays preceding the protons, Monte Carlo simulations were used to generate proton distributions for different values of $a_{\beta\nu}$. In this work, the simulation consists of two major parts: (i) a C++ code (CRADLE++) to calculate the momentum and energy of the particles involved in a decay process, and (ii) a Monte Carlo simulation using the information given by the first step to study how these particles behave in the experimental setup.

6.1.1. Event generator: CRADLE++

CRADLE++ stands for **C**ustomizable **RA**dioactive **D**ecay for **L**ow **E**nergy **P**article **P**hysics. It is designed to studying the kinematics of a specific decay using the momentum- and energy-conservation laws [60]. In this work, the momentum and energy of all particles in the ^{32}Ar beta decay, i.e., the positron, neutrino, and ^{32}Cl, as well as the protons and the ^{31}S daughter isotope from the decay of ^{32}Cl are calculated in the laboratory frame.

The decay kinematics simulated by CRADLE++ follows the decay rate of unpolarized nuclei given in chapter 3 by Eq. (1.9)

$$\omega(\langle J\rangle|\, E_e, \Omega_e, \Omega_\nu)\, dE_e d\Omega_e d\Omega_\nu \;=\; \frac{F(\pm Z, E_e)}{(2\pi)^5} p_e E_e (E_0 - E_e)^2 dE_e d\Omega_e \Omega_\nu$$
$$\times\, \xi\{\mathbb{I} + \frac{p_e\, p_\nu}{E_\beta E_\nu} a_{\beta\nu} + \frac{m}{E_e} b_F + \;\dots\}$$

where the phase space, the Fermi function, and the $a_{\beta\nu}$ value are included in the analysis. The Fierz interference term, b_F, is assumed to be zero in the following discussion. The effect of the b_F term is further investigated in the systematic uncertainty analysis. To start the kinematic decay, CRADLE ++ takes the Q-value from literature. Figure 34 shows the beta energy spectrum generated with CRADLE++.

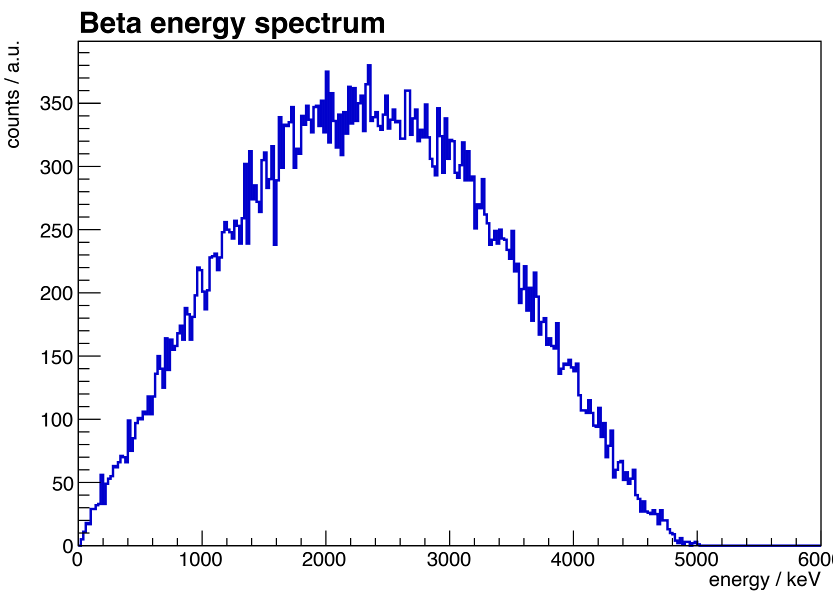

Figure 34. Beta energy spectrum generated by CRADLE++. The simulations consider Coulomb interaction (Fermi function) and phase space shown in equation (1.9).

Equation 1.9 can be written in terms of the angular distribution as follows:

$$W(\theta) = 1 + \frac{p_\beta\, p_\nu\, cos\theta}{E_\beta E_\nu} a_{\beta\nu} \quad \textbf{(6.1)}$$

where θ is the angle between the neutrino and the beta particle. As can be seen from Figure 35, for $a_{\beta\nu} = 0$ this angle is distributed isotropically with no preferred direction in the emission. In the case of a pure scalar contribution ($a_{\beta\nu} = -1$) most decays will have a relatively large θ, close to 180° meaning that the β particle and the neutrino will be emitted in opposite directions. In the case of a pure vector contribution ($a_{\beta\nu} = 1$) the angle θ will in general be small. Notice that in the latter two cases the angular distribution has an anisotropic shape because of energy and momentum conservation.

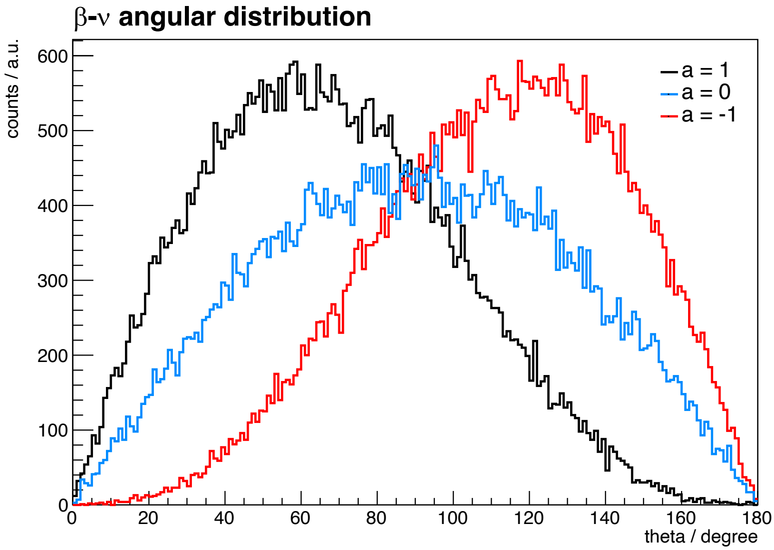

Figure 35. Comparison between three possible angular distributions between the leptons emitted in the ^{32}Ar decay.

Consequently, the shape of the recoil energy spectrum is influenced by the value of $a_{\beta\nu}$, as shown in Figure 36. For a vector contribution (a = 1) the recoil energy reaches a maximum at about 500 eV while for the scalar case (a = -1), the energy of the recoiling nucleus reaches a maximum at a much lower value, i.e., between 100 keV and 200 keV.

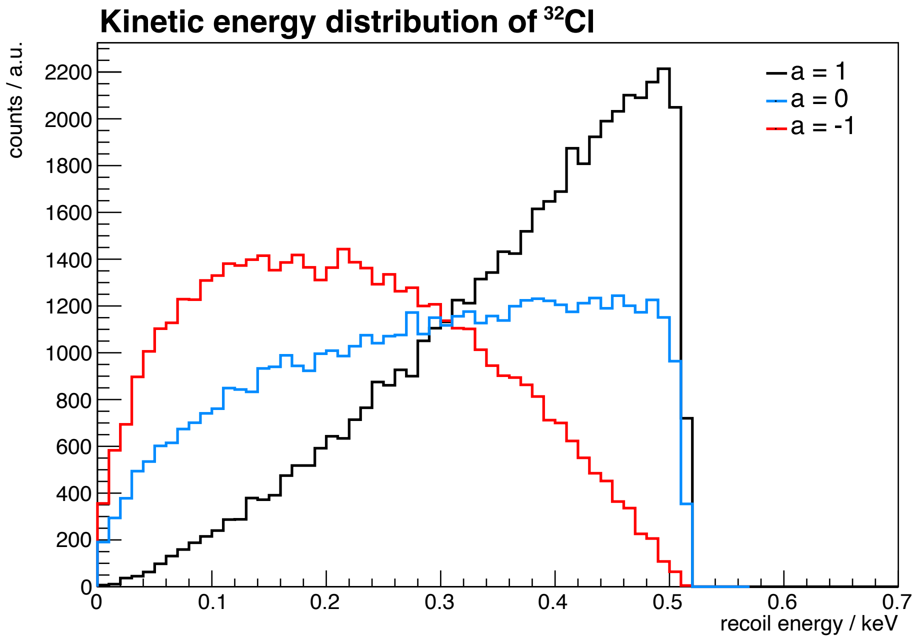

Figure 36. Comparison between different energy spectra for the recoiling daughter isotope ^{32}Cl from the decay of ^{32}Ar with different β–ν angular correlation coefficients, $a_{\beta\nu}$.

Figure 36 shows the different proton energy distributions for several values of $a_{\beta\nu}$ as generated by CRADLE++. For each $a_{\beta\nu}$ value, two possible scenarios are considered for the trajectories of positrons and protons. In the first scenario, protons with a kinematic shift towards lower energies, traveling in the same direction as the detected positrons, are considered. In the second scenario, the protons traveling opposite to the detected positrons, and so with a kinematic shift towards the higher energy side, are considered.

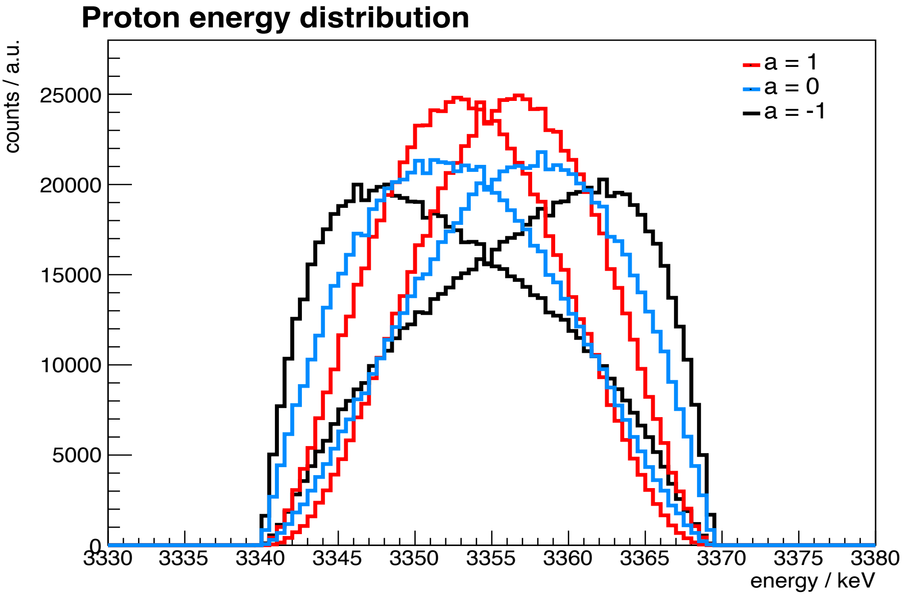

Figure 37. Proton energy distributions as a function of the angle of emission between positron and neutrino. For each value of $a_{\beta\nu}$, two different cases are shown: proton-positron emitted either parallel or antiparallel produces the low and high energy curves, respectively (*see text*).

Figure 37 shows three out of the five $a_{\beta\nu}$ coefficients used to study the kinematic energy shift by means of GEANT4 simulations. Furthermore, the same study was also performed for the four proton lines that follow a GT transition.

6.1.2. GEANT4 simulations

To study the particle behavior under experimental conditions, the detection setup is simulated in GEANT4. Therefore, the geometry and dimensions of the detection setup have been recreated in GEANT4, including the most relevant volumes and materials as is shown in figure 38. Some parts of the detection setup as the rods and mylar holders are imported from Autodesk Inventor using a GDML toolkit.

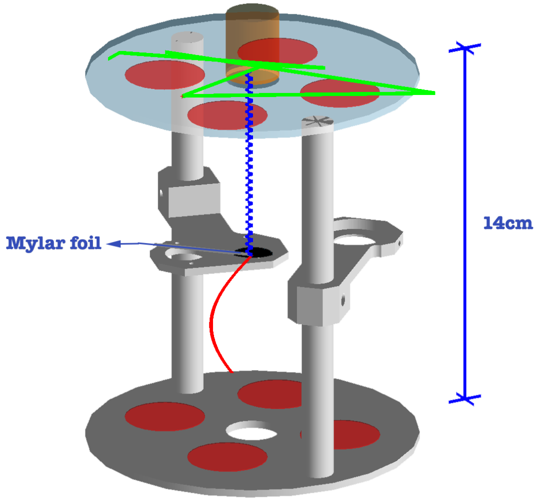

Figure 38. GEANT4 simulation of the detection setup. The red disks represent the proton detectors. In the upper plate, the orange cylinder schematizes the plastic scintillator. The mylar foil is positioned between the detection plates, 7 cm from each. In the figure, a single event is shown for display purposes. The curved red line indicates the trajectory of the proton, the blue spiral is the positron confined by the magnetic field (4T). In green, the photons produced once a beta particle hits the plastic scintillator. The production ratio is roughly 10000/MeV.

To ensure the same experimental conditions in the GEANT4 simulation, the implantation of the ^{32}Ar beam is placed in the first micrometer of the mylar foil, i.e., in the bottom surface, with a concentration distribution following a Gaussian distribution. The generated protons and positrons are propagated through the detection setup, which is immersed in a homogeneous magnetic field of 4T. The proton emission is assumed to be isotropic in the reference frame of the ^{32}Cl nuclei. Protons that hit the wall of the chamber are destroyed neglecting any possible backscattering. The proton energy resolution for the silicon detectors in the simulation is the one obtained from the experimental measurements.

The sensitivity of the backscattering effects is considered only in the study of systematic uncertainties. The mylar thickness in the simulation is set equal to the value from the experiment, i.e., 7 micrometers. In each GEANT4 run 3×10^6 events were used per $a_{\beta\nu}$ value. Approximately 40% of these events counted as detected in relation to the F transition, this value being comparable to the one obtained experimentally.

The output of the generated events for the six proton lines by CRADLE++ can be used directly as input to the GEANT4 simulation to study their behavior under experimental conditions. Figure 39 shows the comparison between the proton energy spectrum simulated with GEANT4 (blue) for the prominent vector contribution and the experimental data. Gamma lines are omitted in the CRADLE++ output file to save CPU time.

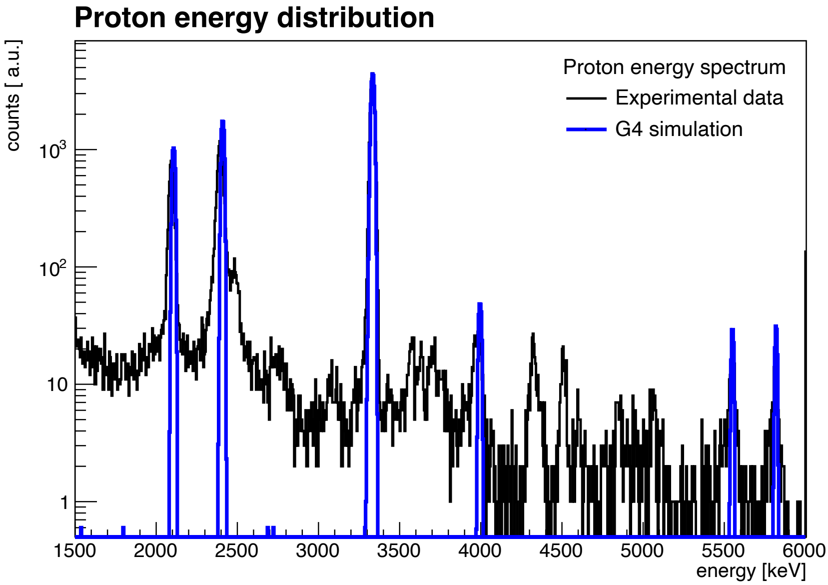

Figure 39. Comparison between experimental data and simulated proton energy distribution from CRADLE++. In blue, the six proton lines at 2121 keV, 2421 keV, 3356 keV, 5555 keV, and 5828 keV used to determine the angular correlation coefficient are shown. The proton line at 3356 keV is of particular importance in this work as it provides information about scalar current contributions.

6.2. Determination of the $\tilde{a}_{\beta\nu}$ coefficient

With the GEANT4 simulations, it is now possible to recreate the decay kinematics for different values for $a_{\beta\nu}$ and determine the kinematic energy shift of the emitted protons under the experimental conditions.

To generate the simulated proton energy distribution, GEANT4 overlays a random number generator which is centralized to the proton energy (from literature) with a certain width; the width is given by the FWHM determined by the experimental data. The FWHM values obtained from the fitting analysis and used to generate the simulated spectra can be found in Appendix D. Furthermore, the simulation FWHM-value has to take into account the proton line width in the final result of the energy resolution.

It is important to verify that the simulation is able to recreate the data obtained in the experiment. For illustrative purposes, Figure 40 shows histograms with single events, and a single detector, to compare the FWHM value from the experiment and the one generated by the simulation. The simulations used the experimental FWHM value in addition to the proton line width has to be considered to generate the proton energy distribution, a small difference between the FWHM values is contemplated. Note that the GEANT4 output has to be rescaled (0.9) to fit the experimental statistics.

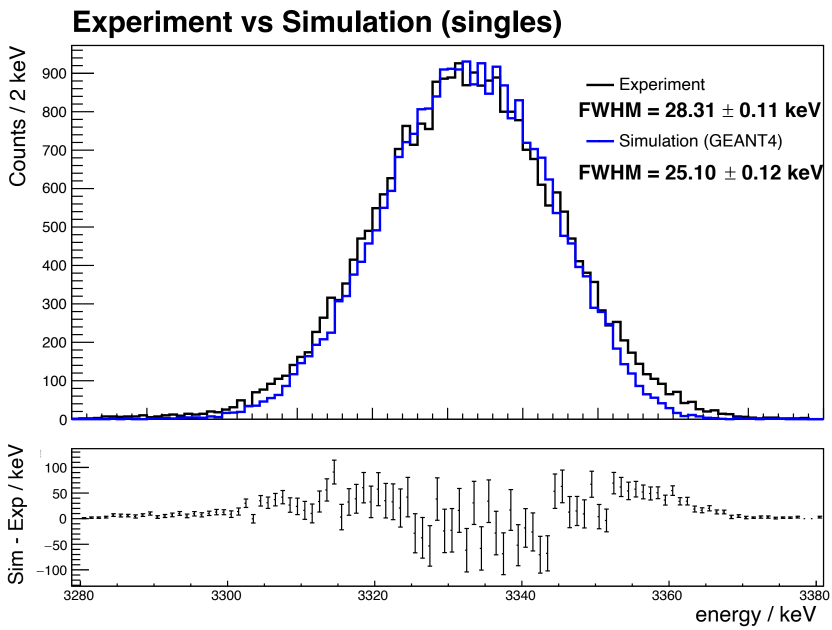

Figure 40. Comparison of the energy distributions (in singles) obtained experimentally and simulated with GEANT4 for the protons following the Fermi beta transition. FWHM presented in each case are also shown (Si2D).

Proton energy spectra in singles and in coincidence with the beta particle are simulated for each proton energy peak included in this work, in order to determine the kinematic energy shift for each kinematic condition (i.e., $a_{\beta\nu}$ value).

The relation between the angular correlation, $a_{\beta\nu}$, and the proton energy shift, E_p, was found to be linear for all proton lines investigated. Figures 41 and 42 shows this linear dependency between $a_{\beta\nu}$ and the proton energy shifts, E_p, for the protons following the F transition and the proton line at 2121 keV following a GT transition, respectively. The dashed lines in both figures take into account the uncertainty from the experimental energy shift (vertical lines) and the linear slope ($da_{\beta\nu}/dE_p$) of the calibration (horizontal lines). The horizontal black solid lines in Figures 40 and 41 indicate the SM prediction for the vector (F transition) and axial-vector (GT transition) contributions with $a_{\beta\nu} = 1$, and $a_{\beta\nu} = -1/3$ respectively. For the sake of brevity, just two plots relevant for the determination of $a_{\beta\nu}$ for the different proton decays are presented here, the rest can be found in Appendix D.

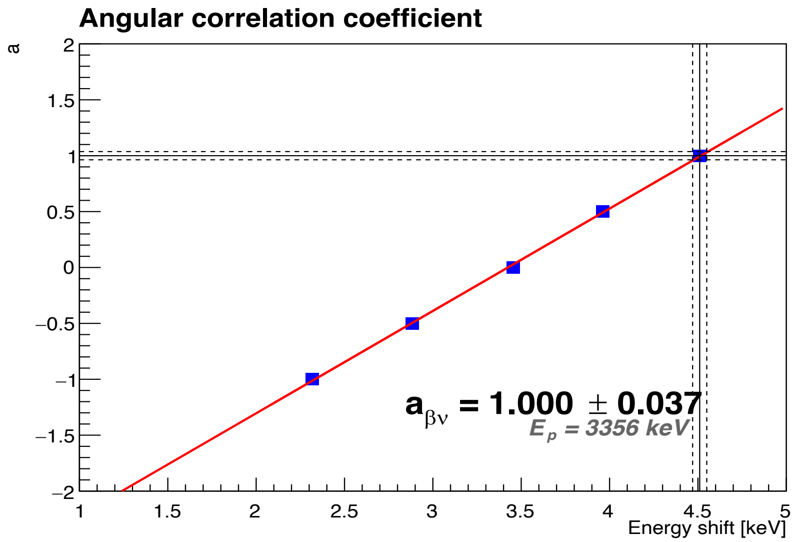

Figure 41. Proton energy shift with respect to the $\beta-\nu$ angular correlation value for protons following the Fermi beta transition. Solid black lines show: (vertical) the experimental energy shift and (horizontal) the $a_{\beta\nu}$ value deduced for the protons following the superallowed Fermi decay. The dashed horizontal and vertical lines are uncertainties related to the linear fit and the experimental energy shift, respectively.

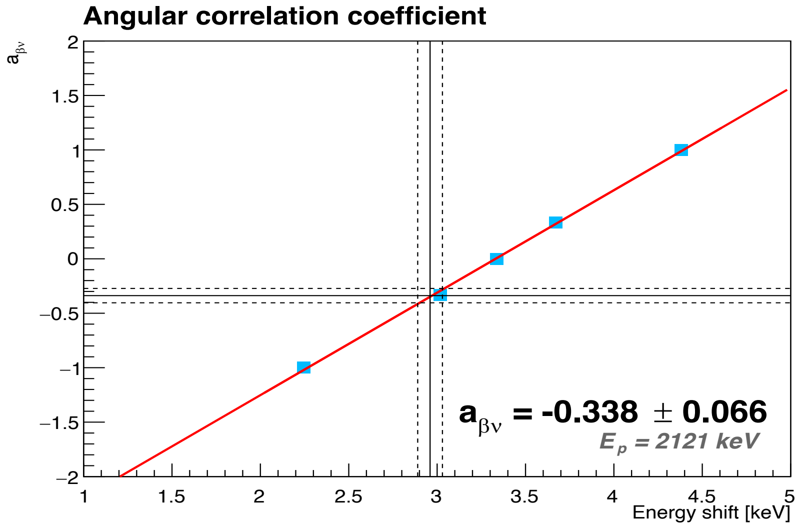

Figure 42. Proton energy shift with respect to the β−ν angular correlation value for the 2121 keV protons following a Gamow-Teller transition. Solid black lines: (vertical) experimental energy shift and (horizontal) $a_{\beta\nu}$ value. The dashed horizontal and vertical lines are uncertainties related to the linear fit and the experimental energy shift, respectively.

Table 8 summaries the obtained $a_{\beta\nu}$ values for each proton line studied here as the rate between the kinematic energy shift predicted by GEANT4 simulations and $a_{\beta\nu}$.

Table 8. Angular correlation coefficients for the analyzed proton lines. In bold, the best values for the proton lines following a GT and F beta transition, respectively.

Proton energy E_p[keV]	Experimental kinematic energy shift [keV]	$da_{\beta\nu}/dE_s$	$\tilde{a}_{\beta\nu}$
2121.7(31)	2.96 ± 0.07	0.936	-0.338 ± 0.066
2421.8(29)	3.26 ± 0.09	0.959	-0.130 ± 0.086
3356.0(7)	4.51 ± 0.04	0.912	1.000 ± 0.037
3988.6(36)	3.78 ± 1.01	0.983	0.468 ± 0.993
5555.5(45)	3.16 ± 0.96	1.333	0.618 ± 1.280
5832.1(53)	4.32 ± 1.96	1.413	2.495 ± 2.769

6.3. Systematic uncertainties

The dominant one sigma systematic uncertainties for the beta neutrino angular correlation coefficient are listed in Table 9. The systematic uncertainties are expected to be independent and assumed to be linear. The following equation describes the link between the sources of systematic errors, κ, and $a_{\beta\nu}$,

$$\frac{da_{\beta\nu}}{d\kappa} = \frac{da_{\beta\nu}}{dE_S}\frac{dE_S}{d\kappa} \quad \textbf{(6.2)}$$

where $da_{\beta\nu}/d\kappa$ is how much the value of $a_{\beta\nu}$ is modified with respect to the systematic error κ, and κ can be any of the systematic errors listed in Table 9, and dE_S is the kinematic energy shift determined by simulations. The first term at the right-hand side of the equation is the slope of the linear calibration of the proton energy shift with respect to the β−ν angular correlation obtained in section 6.2. A new set of simulations has to be done in order to determine the impact of each systematic uncertainty, κ, on the energy shift. Each systematic uncertainty is studied independently. The total uncertainty is calculated by combining all systematic errors in quadrature. A brief description of the dominant systematic effects is given below.

Proton detectors

There are three dominant sources of systematic uncertainty associated with the proton detectors: the dead layer thickness, the proton energies of the different decays taken from the literature for the calibration, and the linear slope of the calibration. To study the impact of each source of systematic uncertainty on $a_{\beta\nu}$, GEANT4 simulations were carried out. The effect of the uncertainty on the proton energy values in the literature [50] (see also column 1 in Table 8) was studied by varying the proton energies and looking by how much the kinematic energy shift changes by 1 keV the proton energy value from the literature. The relation obtained follows the equation 6.2, where $dE_p/d\kappa = 0.0135$ with κ being the proton energy from literature. For the protons following the F beta transition this leads to an uncertainty of $\delta\tilde{a} = \pm 0.0123$. The average uncertainty on the calibration slope was found to be 0.3%. All proton detectors are assumed to have the same dead layer thickness of 1290(120) nm leading to an uncertainty on $a_{\beta\nu}$ of 0.0115. Contributions to the systematic uncertainty from the distance between the proton detectors to the mylar foil, and from the implantation position, were also studied and are mentioned in the section of "non-dominant" uncertainties.

Beta detector

There are two cases in which the detection of positrons strongly influences the sum over all the systematic uncertainties. The first case is when the positrons leave enough energy to be detected by the plastic scintillator i.e., above the threshold value, and the second case is simply when the previous condition is not fulfilled, and the positrons are not detected although they have been emitted upwards. The latter case can be due to two possibilities: either the initial energy of the positrons is too small to generate a measurable signal or due to backscattering. In both cases the precision of the measurement on the kinematic energy shift can be affected since a wrong value for the beta threshold could jeopardize the number of coincidence events. To quantify for these effects, one needs to rely on Monte Carlo (MC) simulations. Therefore, the sensitivity on the threshold value was determined by changing its value in the range from 5 to 85 keV leading to a significant uncertainty on $a_{\beta\nu}$ of $\delta\tilde{a} = \pm 0.0013$ per keV. Apart from this threshold energy effect, positrons can also be scattered inside the mylar foil so as to prevent the detection of positrons initially emitted upwards. By varying the mylar thickness in the simulations by 10% the impact of this was found to be $\delta\tilde{a} = \pm 0.0049$. The fraction of positrons that are not detected due to backscattering on the plastic scintillator was found to be $3\text{x}10^{-3}$ for the protons following the F transition.

Last but not least, the effects of beta scattering were carried out by changing the electromagnetic modules within the physics list in GEANT4. The electromagnetic modules as Penelope were used along with the Goudsmit-Saunderson multiple-scattering model and the LowEWentzelVI model to determine the impact of the positron backscattering due to the mylar material and possible grazing angles on the surface of the plastic scintillator once the positrons reach it. The final value for the beta scattering effect led to a correction of $\delta\tilde{a} = \pm 0.0174$ for the protons following the F transition.

Sensitivity of the Fierz interference term ($b_F \neq 0$)

Although the WISArD approach is not aimed to search for exotic tensor contributions, studies on the sensitivity that can be reached by the Fierz interference term, b_F, is also undertaken. So far, the b_F term was set to zero to test right-handed neutrino contributions by searching for a non-zero value for $a_{\beta\nu}$. An extension of this study can be done by looking for possible left-handed neutrino contributions, i.e., by searching for a non-zero value of the Fierz interference term, b_F. Different simulations with values b_F = -1, 0 and 1 were carried out for the F transition. The change on the angular correlation coefficient with respect to the Fierz term led to $\delta\tilde{a} = \pm 0.00021$.

Non-dominant systematic uncertainties

Additional sources of systematic uncertainties were investigated, such as: the perturbation in the magnetic field, the distance between detector plates and the mylar foil, the implantation position of the ^{32}Ar beam on the mylar foil, and the diameter of the ^{32}Ar beam. They were found to contribute together at a level of $\delta\tilde{a} = \pm 0.0009$. The estimation of false coincidence events with T_{diff} outside the time selection criteria turned out to be less than 0.3% for the selected data. The quadratic sum of all non-dominant systematic effects leads to a combined uncertainty of $\delta\tilde{a} = \pm 0.027$ in $\tilde{a}_F$ at one-sigma as is shown in Table 9.

Table 9. Sources of systematic uncertainties $\delta\tilde{a}$ (x10^{-3}) for the Fermi and Gamow-Teller transitions, respectively.

	Source	Uncertainty	$\delta\tilde{a}_F$	$\delta\tilde{a}_{GT}$
Background	False coincidence	0.3%	1	2
Proton	Linear slope uncertainty	0.3%	9	6
	Proton energy from literature	1 keV	1.23	2.59
	dead layer thickness	120 nm	11.5	15
	Mylar thickness	700 nm	4.87	6.60
Positron	β backscattering	15%	17.39	27.8
	β energy threshold	12 keV	6.53	8.2
Non-dominant	Detector position	1 mm	0.321	0.186
	Source position	1 mm	0.786	0.278
	Source radius	1 mm	0.167	0.177
	Magnetic field	1%	0.002	0.464
	Fierz interference term, b_F	0.1%	0.021	0.028
Total			0.027	0.033

The pie chart presents (Fig. 43) all the systematic uncertainties involved in the measurement of the $a_{\beta\nu}$ value for the F transition. The dominant uncertainty is the backscattering of the beta particles in the mylar foil and in the scintillating plastic, the latter due to the energy threshold.

The systematic uncertainty contribution from inaccuracies in the proton energies reported in the literature decays points out the importance of knowing precisely the calibration in energy, and the dead layer of the detectors.

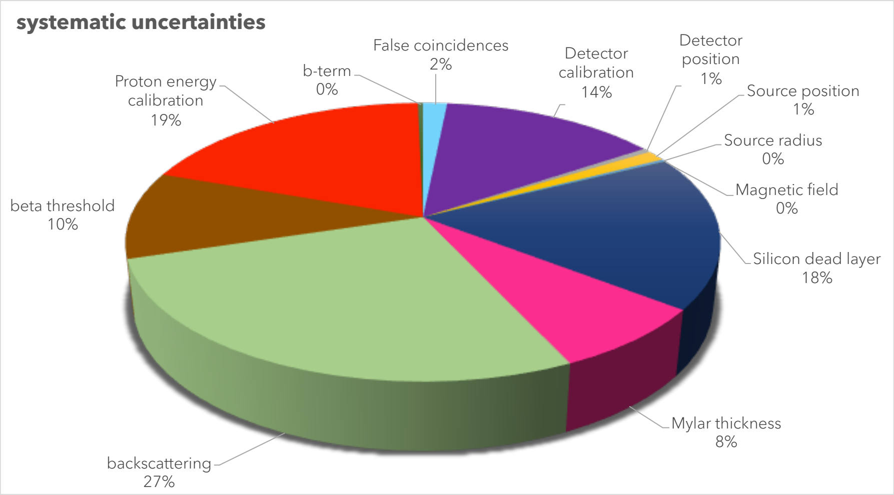

Figure 43. The pie chart summarizes the results obtained by the uncertainty analysis for the superallowed Fermi transition.

Final results

The proof-of-principle experiment based on proton-positron coincidences that was reported here led to a final value on the angular correlation coefficient for a Fermi transition as

$$\tilde{a}_F = 1.000 \pm 0.037_{stat} \pm 0.027_{sys}$$

and for the protons at 2121 keV following a GT transition

$$\tilde{a}_{GT} = -0.338 \pm 0.066_{stat} \pm 0.033_{sys}$$

Both $a_{\beta\nu}$ coefficients agree with the expected SM values of 1 and -1/3, respectively. The technique is not well developed for the search of tensor contributions even though simultaneous measurements of GT and F transitions remain useful to track systematic uncertainties and corroborate the obtained values for the F transition.

7
Conclusion and perspective

"Science makes people reach selflessly for truth and objectivity; it teaches people to accept reality with wonder and admiration". - L Meitner

High precision measurements of the kinematic energy shift from the beta-delayed proton emission in the decay of ^{32}Ar were made. The results obtained from the experimental data are in agreement with the SM predictions for the 3356 keV protons following the superallowed F transition and the 2121 keV protons following a GT transition. These results confirm that the dominant contributions in the weak interaction are Vector and Axial-vector types. Still, the obtained results leave room to pursue the one per mile precision in the search for exotic contributions aside the dominant weak interaction components.

The proof-of-principle experiment was successful as it produced the third-best measurement of $a_{\beta\nu}$ for a pure F transition, in spite of the limited beam time allocated. Even though the data taken for the present work did not improve the present limits for scalar currents in the weak interaction, the obtained results leave the WISArD experiment well-positioned to improve with high precision measurements our knowledge of the beta-neutrino angular correlation, as will be discussed below.

7.1. WISArD: The third best $a_{\beta\nu}$ value!

The results of this proof-of-principle experiment based on proton-positron coincidences are $\tilde{a}_F = 1.000 \pm 0.037_{stat} \pm 0.027_{sys}$ for the Fermi transition and $\tilde{a}_{GT} = -0.338 \pm 0.066_{stat} \pm 0.033_{sys}$ for the GT transition. Both values are found to be in agreement with the SM predictions. Although more statistics could have been obtained, during this proof-of-principle experiment, the collected data nevertheless provide the third most precise measurement of $a_{\beta\nu}$ in a pure F transition.

As a consequence of recent updates on the proton energy emitted in the ^{32}Ar decay [50], the numerical values deduced for some parameters are slightly different from those given in the earlier paper [61], although all values still agree within the error bars.

The present situation of the limits on scalar coupling constants for the most precise measurements of the $a_{\beta\nu}$ and b_F parameters are summarized in the exclusion plot (see figure 43) at 95 % confidence level. The donut-type limits are the result of the measurement of the beta-delayed proton peak after the superallowed beta decay of ^{32}Ar by Adelberger et. al. (green; $a_{\beta\nu}$ = 0.9989(52))[33], Gorelov et. al. (pink; $a_{\beta\nu}$ = 0.9981(30)) [27] and the current value achieved by the WISArD experiment in red. The diagonal band is the result of the determination of the Fierz interference term from the ft-values of some superallowed $0^+ \rightarrow 0^+$ beta-transitions quoted in [62]. As discussed before, the measurements of $a_{\beta\nu}$ and of the interference term yield information on the coupling constants that is complementary with high energy experiments as CMS. Current limits for high energy experiments can be seen by the small black circle and the dot in its center in Figure 44.

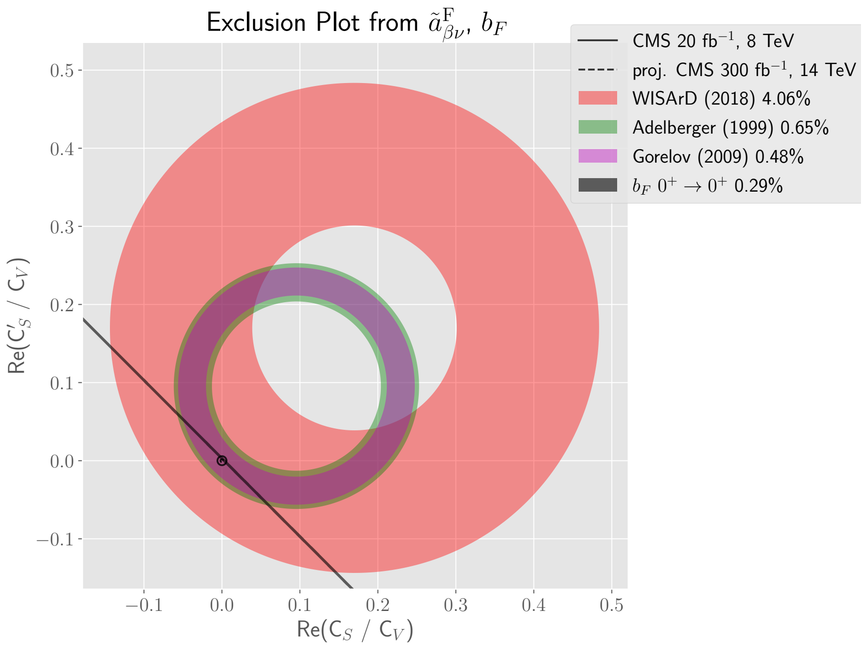

Figure 44. Current constraint values for scalar contributions achieved by the WISArD experiment during the 2018 ^{32}Ar campaing (red area). In the plot also the limits obtained from the two most precise experiments to date are shown (pink and green). The black dot represents the current limits obtained from the high energy experiment CMS at the Large Hadron Collider. The limits on the Fierz term from the superallowed 0^+ to 0^+ beta decays is shown by the black solid line.

7.2. Perspective

With the current experimental setup, only one candidate was used to study scalar interactions, although the list of candidates is vast. Candidates as ^{20}Mg, ^{24}Si, ^{28}S, and ^{36}Ca have similar decay features and can be easily used with the WISArD setup. Table 10 shows the curvature radii for these using a 4T magnetic field. The choice of the isotope will strongly depend on the production yield. Currently only ^{32}Ar and ^{20}Mg can be produced at ISOLDE/CERN, the latter one with a low production rate.

Table 10. The candidates with isospin equals two, that can be easily studied using the WISArD experimental approach. The choise of the next candidate strongly depends on the production yield offered by the ISOLDE facility. The curvature radius shown here is calculated for 4T magnetic field.

Isotope	Lifetime [ms]	E_p [MeV]	Radius of curvature [mm]
^{20}Mg	137.05	4.28	7.4
^{24}Si	147.15	3.91	7
^{28}S	180.33	3.70	6.9
^{32}Ar	98	3.35	6.5
^{36}Ca	141.15	2.55	5.7

In order to achieve the 0.1% precision measurement, some sources of systematic uncertainties can easily be reduced, such as e.g., using a catcher foil as thin as possible to reduce the beta backscattering. By using a 500-nm thick mylar a factor of 10 less on the effect of positron backscattering can be achieved. A detailed study and control of the beta threshold and its uncertainty of the plastic scintillator is also required. A desirable beta threshold value would be less than 10 keV to avoid missing events. The goal is to reduce the uncertainty on the beta threshold down to 5 keV.

Upgrades in the proton detection energy resolution in the silicon detectors from 35 keV to 10 keV will lead to a total gain factor close to 50 in the statistical uncertainty. By increasing by a factor of 3 the detection solid angles (from 8% to 30%) the statistical uncertainty can be reduced by a factor of 2.

Last but not least, an improvement in the production yield of ^{32}Ar with a longer beamtime period seems feasible to finally reach a conservative 0.2% measurement and possibly a 0.1% on the beta neutrino angular correlation coefficient. The following exclusion plot summarizes the aimed goals for the WISArD experiment which includes these upgrades (that are currently being prepared) and is scheduled for the ISOLDE campaign in 2021.

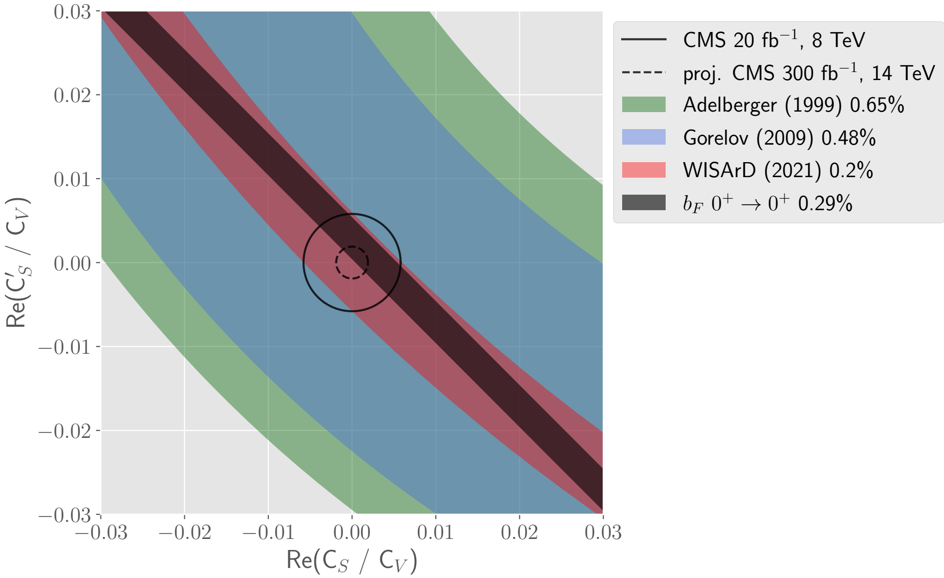

Figure 45. Expected constraints on the scalar contributions after better controlling the systematic errors in the 2018 campaing if a 0.2% precision measurement is achieved the WISArD experiment would constitute the most precise measurement of the beta-neutrino angular correlation at the low-energy scale.

Appendix A

In the following section the equations used along this work are presented.

a. Radius of curvature

The radius of curvature describes the maximum radial distance experienced by charged particles due to the presence of a magnetic field. The derivation of the relativistic form is presented in the following equation:

$$r = \frac{\gamma m v}{|q|B}$$

where γ is the Lorentz factor, m is the mass of the particle, e.g., proton or positron, v is the velocity perpendicular to the direction of the magnetic field, B, and q is the electric charge.

The active surface of the silicon detectors (30 mm) constraint the proton detection from 17 mm to 47 mm, considering zero at the geometric center (see figure 14), i.e., protons moving out of this range will not be detected. Proton with high energies higher than 6 MeV are not considered in the analysis. In the present work, the detection configuration was designed to prefer the superallowed $0^+ \rightarrow 0^+$ Fermi transition. The 3356 keV proton energy following the Fermi transition describe a radius of curvature of 20 mm for a 4T field. An increase in the detection solid angle by a factor of 3 not just reduce the statistical error quoted in chapter 6, it could also improve the precision in other proton lines following a Gamow-Teller transition.
To determine the radius of curvature of the positrons, a relativistic case is followed. For instance, for a 4T field, the radius of curvature of 1 MeV positrons is 1.2 mm.

b. Maximum kinematic recoiling energy

The maximum kinematic energy of the recoiling ^{32}Cl is 517 eV, value quoted by Adelberger et. al., [49] and it is deduced here. Let P, P_1, and P_2 be the four-momentum of the particles involved in beta decay.

$$\mathrm{P} = (E, 0,0,0) \quad \text{..... (1)}$$

$$\mathrm{P}_1 = (E_1, p_{1x}, p_{1y}, p_{1z}) \quad \text{..... (2)}$$

$$\mathrm{P}_2 = (E_2, p_{2x}, p_{2y}, p_{2z}) \quad \text{..... (3)}$$

The law of momentum conservation can be stated as follows

$$\mathrm{P} = \mathrm{P}_1 + \mathrm{P}_2 \qquad \text{..... (4)}$$

According to the conservation of energy and momentum, the momentum can be written in terms of the energy as

$$\mathrm{P}^2 = E^2 = M^2c^4 \qquad \text{.....(5)}$$

$$\mathrm{P}_1^2 = {E_1}^2 - c^2\vec{p}_1 \cdot \vec{p}_1 = {m_1}^2c^4 \qquad \text{.....(6)}$$

$$\mathrm{P}_2^2 = {E_2}^2 - c^2\vec{p}_2 \cdot \vec{p}_2 = {m_2}^2c^4 \qquad \text{.....(7)}$$

Solving for P_2 using equation (4)

$$\mathrm{P}_2 = \mathrm{P} - \mathrm{P}_1 \qquad \text{.....(8)}$$

$$\mathrm{P}_2^2 = (\mathrm{P} - \mathrm{P}_1)^2 \qquad \text{.....(9)}$$

$$\mathrm{P}_2^2 = \mathrm{P}^2 - 2\mathrm{P}\mathrm{P}_1 + \mathrm{P}_1^2 \qquad \text{.....(10)}$$

Replacing the values from (5), (6) and (7) in (10)

$${m_2}^2c^4 = M^2c^4 - 2m_1Mc^4E_1 + {m_1}^2c^4 \qquad \text{.....(11)}$$

Solving for E_1

$$E_1 = \frac{M^2c^4 - {m_2}^2c^4 + {m_1}^2c^4}{2m_1Mc^4} \qquad \text{.....(12)}$$

The kinematic recoiling energy $\mathrm{T_r}$ is given by the following expression

$$\mathrm{T}_r = \mathrm{E} - \mathrm{E}_1 - m_2\mathrm{c}^2 \qquad \text{.....(13)}$$

replacing for the previous values

$$\mathrm{T}_r = \mathrm{Mc}^2 - \frac{\mathrm{M^2c^4 - m_2c^4 + m_1c^4}}{2Mc^2} - m_2\mathrm{c}^2 \qquad \text{.....(14)}$$

rewriting previous equation to

$$\mathrm{T}_r = \frac{\left[(\mathrm{M} - \mathrm{m}_2)^2 - \mathrm{m}_1\right]}{2M}\mathrm{c}^2 \qquad \text{...... (15)}$$

where M and $\mathrm{m_2}$ can be re-written as

$$\mathrm{M} = \mathrm{M}^* - Z\mathrm{m}_e$$

$$\mathrm{m}_2 = {\mathrm{m}_2}^* - (Z - 1)\,\mathrm{m}_e$$

$$\mathrm{M} - \mathrm{m}_2 = \mathrm{M}^* - {\mathrm{m}_2}^* - \mathrm{m}_e$$

c. Uncertainty of the proton energy shift

The main idea is to express the uncertainty of the proton energy shift as a function of coincidence (C) and no-coincidence (NC) events; hence the single spectra contain both event types. Mathematically it is expressed as

$$\bar{E}_p = \bar{E}_C - \bar{E}_S \quad .... (1)$$

where $\bar{E}$ denote the statistical errors for the mean proton energy in coincidence (C) and singles (S). The latter one can be written in terms of C and NC as followed,

$$\bar{E}_S = \frac{N_C\bar{E}_C + N_{NC}\bar{E}_{NC}}{N_S} \quad ..... (2)$$

with N_S, the total number of counts (integral value) for single events. Substituting equation (2) in (1)

$$\bar{E}_p = (\bar{E}_C - \bar{E}_{NC})\left(1 - \frac{N_C}{N_S}\right) \quad ..... (3)$$

The uncertainty of the proton energy shift is a function which depends on the variables in coincidence and non-coincidence events, $\bar{E}_p = f(\partial\bar{E}_C, \partial\bar{E}_{NC})$, and since $N_S = N_C + N_{NC}$, using equation (3) the partial derivatives are expressed as

$$\frac{\partial\bar{E}_p}{\partial\bar{E}_C} = \left(1 - \frac{N_C}{N_S}\right) \cong \frac{1}{2} \quad ..... (4)$$

$$\frac{\partial\bar{E}_p}{\partial\bar{E}_{NC}} = -\left(1 - \frac{N_C}{N_S}\right) \cong -\frac{1}{2} \quad ..... (5)$$

$$\frac{\partial\bar{E}_p}{\partial N_C} = \frac{\partial}{\partial N_C}(\bar{E}_C - \bar{E}_{NC})\left(1 - \frac{N_C}{N_S}\right) = -\frac{\bar{E}_p}{N_S} \quad ..... (6)$$

$$\frac{\partial\bar{E}_p}{\partial N_{NC}} = (\bar{E}_C - \bar{E}_{NC})\left(1 - \frac{N_C}{N_S}\right) = \frac{\bar{E}_p}{N_S} \quad ..... (7)$$

Combining equations from (4) to (6)

$$\bar{E}_p = \sqrt{\frac{1}{2}\bar{E}_{Nc}^2 + \frac{1}{2}\bar{E}_c^2 + \left(\frac{\bar{E}_p}{N_S}\right)^2} \quad .....(8)$$

Finally, the uncertainty associated to the proton energy shift is described by equation (9) by assuming that $\bar{E}_C \cong \bar{E}_{NC}$.

$$\overline{\delta E_p} = \sqrt{\frac{1}{2}\bar{E}_c^2 + \frac{1}{N_S}\bar{E}_p^2} \quad .... (9)$$

Appendix B

a. Beamline: electrode structure and vacuum system

Horizontal beamline

The WISARD experiment is located inside the ISOLDE hall where it is recognized as one of the two experiment platforms. The nearly 10m-high platform, created to maintain the superconducting magnet (Oxford Instruments) as well as the ion beam components for effective ion transmission, is located conveniently close to the REXTRAP setup from where the ion beam is delivered to the experiment. From the last REXTRAP outlet valve (UHV) to the 90° bender of the WISArD experiment (HBBEND02 in figure 46) is described as the horizontal beamline (HBL) that expands about 6m in length, the spatial distance required to avoid possible disturbances due to the strong magnetic field (up to 9T) in neighboring experiments such as REX-ISOLDE. However, with recent updates to the high-energy section of ISOLDE, energizing the WISArD magnet requires advance planning. The horizontal beamline consists of various electrodes and diagnostic tools to adjust and transport the beam with the least amount of losses to the vertical beamline input. Figure 46 shows an overview of the elements presented in the HBL; the labels respect the notation used by the former WITCH experiment.

Table 11. Convention list used to describe the electrostatic components in the WISArD beamline.

Label	Function
HB	Horizontal beamline
VB	Vertical beamline
IS	Ion Source in HBL
KICK	Kickers
BEND	Benders
STEE	Steerers
EINZ	Einzel lens electrode
RETA	Retardation electrode
PDT	Pulse drift tube
DRIF	Drift electrode
FCUP	Faraday cup detector

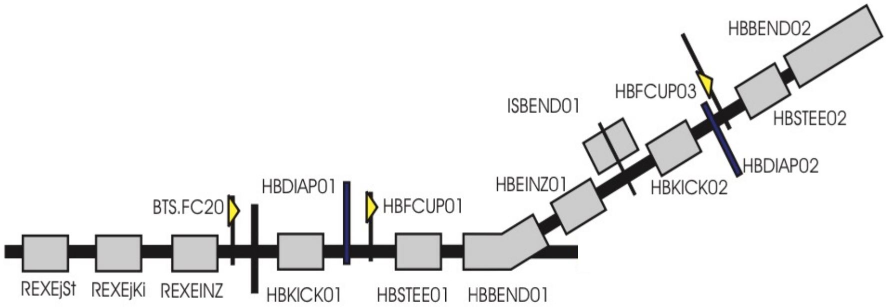

Figure 46. Overview of the electrode structure in the horizontal beamline (HB) and diagnostic tool elements as Faraday cups (FC) used to monitoring the beam transmission to the vertical beamline.

The main electrostatic elements on the HBL section are the kickers and the benders. The kickers (two parallel deflection plates of 60x60 mm^2 with a gap of 3 cm) are located before each bender electrode and can be used as a beam switch. The applied voltage during the ^{32}Ar campaign is presented in Table 12.

Table 12. Voltages values applied to the electrostatic components located in the horizontal beamline during the ^{32}Ar campaign (November 2018).

Electrode name	Voltage [V]
HBKICK01	1200
HBSTEE01	±30
HBBEND01	2039
HBEINZ01	12760
HBKICK02	1314
HBSTEE02	±80
HBBEND02	2181

The two spherical bender electrodes located in the HBL are used to bend the trajectory of the beam in 29º (HBBEN01), and the second one gives the option to bend the ion beam in a radius of 400 mm (385 mm and 415 mm inner and outer radius of the spherical electrodes, respectively). The electrode HBBEND02 is used to link the HBL to the vertical beamline (VBL), see Figure 47. A third bender (ISBEND01, see figure 46) is also located in the HBL in an in-out mechanical position used to perform offline test with stable beam from the offline ion source (IS).

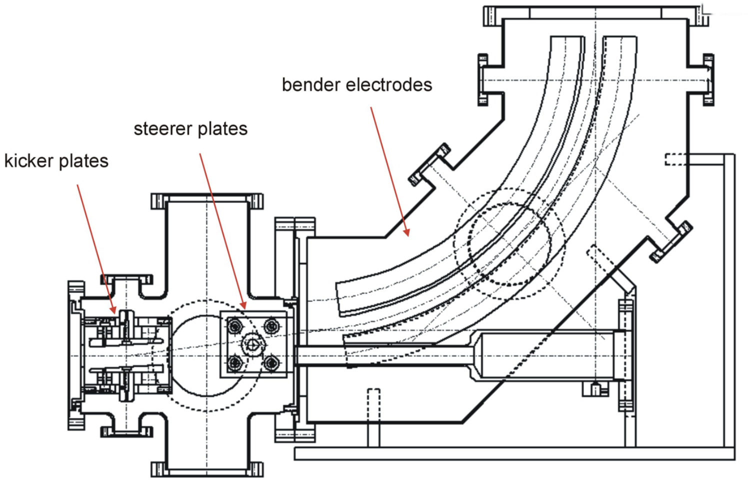

Figure 47. Layout of the 90º bender electrode. It is used to guide the ion beam towards the vertical beamline. The two spherical electrodes allow bending of the ion beam in a radius of 400 mm in a perpendicular direction to the deflection of the plane. (electrode radius: inner 385 mm and outer 415 mm) *Drawing taken from Delaure thesis.*

Among the upgrades to the WISArD beamline was the remote control of the high voltage sources as well as the vacuum system components, such as the UHV-valves. The vacuum system is separated into two parts in the HBL section, the first part consists of the vacuum system for the mainline (HBUHVV01 to VBUHVV01, see figure 49), and the second independent section separated by a manual valve dedicated to the offline-ion source section.

Vertical beamline

The vertical beamline (VBL) consists of 60 mm-diameter stainless steel cylindrical electrodes, four x-y steerer plates to optimize the beam transmission, and what was once a pulse drift tube (VBPDT) to slow down the energy of the ion bunch beam for the former WITCH experiment it is now used as a 78 cm long electrostatic element. The HV switch and the involved electronics had to be removed. The WISArD experiment uses a 30 keV-continuous ^{32}Ar beam. The einzellens presented in the VBL are used to focus and force the beam trajectory as parallel it can be to the magnetic field lines before reaching the superconducting magnet section. As it was the case for the HBL section, diagnostic tools (four Faraday cups and collimator strip system) are also installed along the VBL. In figure 48 an overview of the electrostatic ion beam elements is shown.

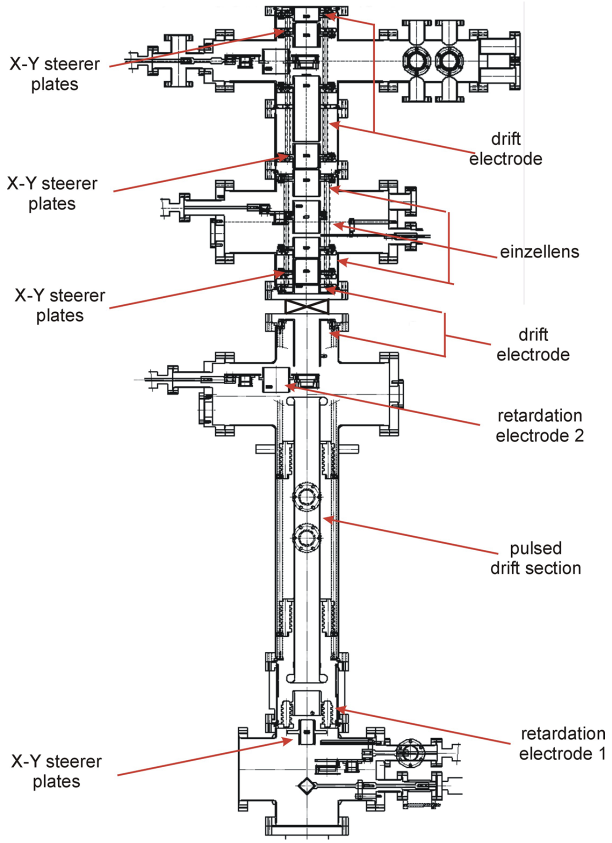

Figure 48. Overview of the electrostatic ion beam elements located in the vertical beamline (VBL). The VBL is built up of cylindrical electrostatic electrodes with 60 mm inner diameter. Four X-Y steerer plates and a 78cm-length electrode, labelled as pulse drift section. *Figure taken from Delaure thesis.*

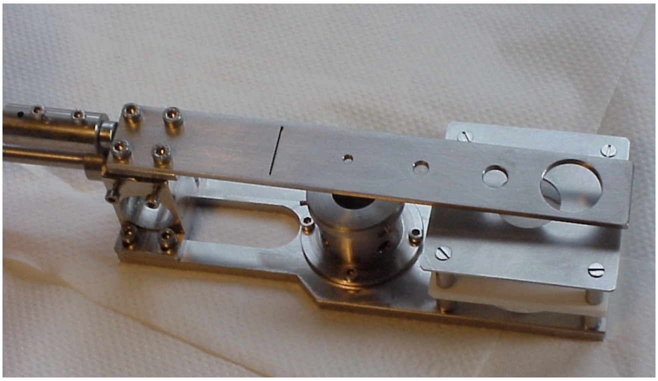

Figure 49. Picture of the diagnostic ion optics tool. A collimator strip system with a 20x1 mm^2 (slit), 3, 5, 8, and 20 mm-aperture uses to perform beam diagnostic test. The collimator strips are only located in

the HBL. In all diagnostic tray a Faraday cup (16.5 mm diameter) is installed, furthermore the installation of microchanner plate detectors is contemplated. *Photo taken from Delaure thesis.*

High voltages values used during the ^{32}Ar campaign in November 2018 are presented in table 13.

Table 13. Voltages values applied to the electrostatic components located in the vertical beamline during the ^{32}Ar campaign (November 2018).

Electrode name	Voltage [V]
VBSTEE01-V	-46
VBSTEE01-H	20
VBRETA01	0
VBPDT01	-8000
VBRETA02	0
VBDRIF01	-8000
VBDRIF02	0
VBSTEE02-H	210
VBDRIF03	0
VBEINZ01	0
VBDRIF04	0
VBSTEE03-H	100
VBDRIF05	0
VBDRIF06	0
VBSTEE04	0
VBDRIF07	0

The figure 50 shows the user interface in LabVIEW to set the high voltage values for the different electrostatic elements along the beamline.
At this point, either to perform current measurements of the low-intensity ion beam or to analyze the beam transmission by using the collimators, positioning the FC and the collimator strip is done manually by means of a linear motion feedthrough.

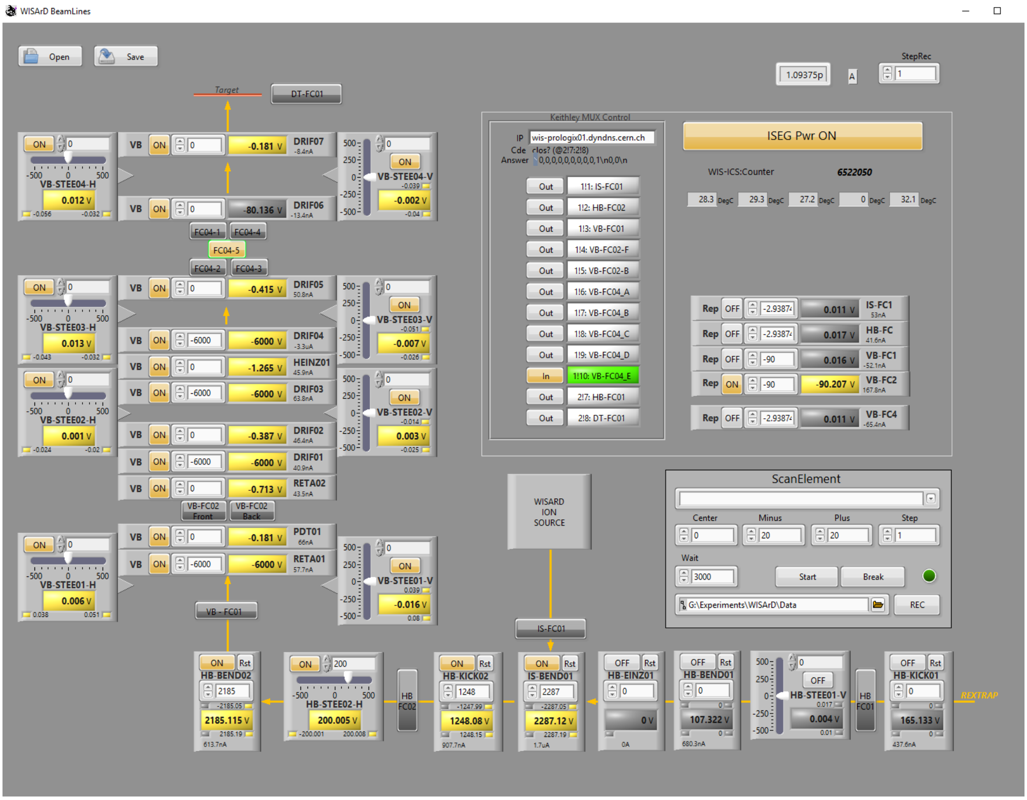

Figure 50. LabVIEW interface of the control panel of the high voltage power supplies for the WISArD experiment.

The vacuum system for the VBL is separated in three sections with ultra-high vacuum (UHV) valves. Each section is able to reach 10^{-7}mbar. Table 14 shows the labels used to describe the components and Figure 51 is the overview of the sections and elements of the vacuum system.

Table 14. Convention list used to describe the vacuum components of the WISArD beamline

convention	meaning
MS	Magnet System section
SP	Spectrometer section
UHVV	UHV Valve
PREV	Pre-vacuum Valve
PREG	Pre-vacuum Gauge
FULL	Full Range Gauge

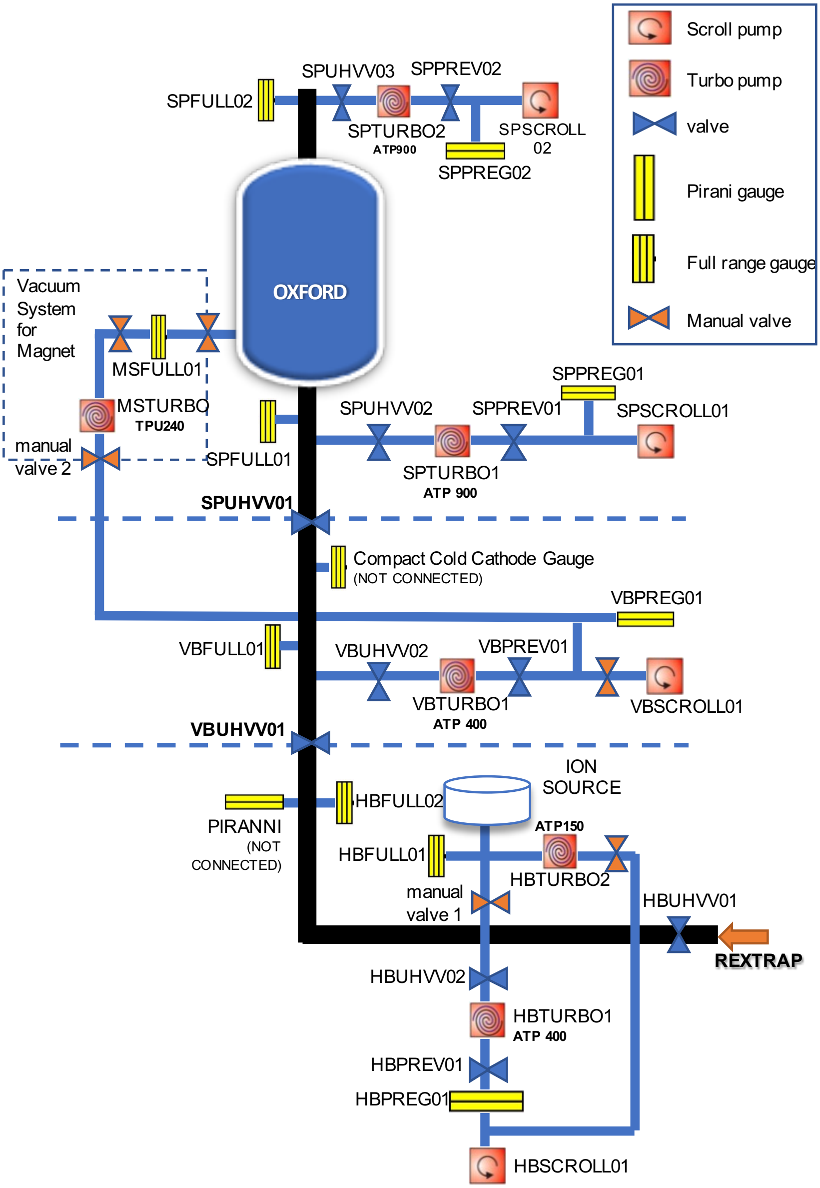

Figure 51. Layout of the vacuum components. The ultra-high vacuum valves are used to split the vacuum in different stages in the platform.

In figure 52 a picture of the SIMATIC touch panel used to control the vacuum elements as the turbo molecular pumps, the open/close of the UHV valves; safety procedures are included in the SIMATIC configuration e.g., a sudden change in the vacuum pressure will cause the UHV-valves to close automatically, blocking the section where the vacuum is less than 10^{-3} mbars. The voltages applied to the ion source can be also controlled on a secondary display in the SIMATIC touch panel, see figure 54.

Figure 52. WISArD SIMATIC touch panel control. In the touch screen, the layout use to visualize the vacuum system through the beamline. Security measures are also shown in the picture.

b. Offline ion source

A surface ionization ion source (^{20}Na) is used to perform offline beam diagnostic; a picture of the source used to tune stable beam before the ^{32}Ar campaign is shown in figure 53. The ion source consists of three electrostatic elements, einzellens, used to extract the beam towards the horizontal beamline. The first step is to set a high voltage tension (ISHT) in order to get the pellet filled with ^{20}Na, see figure 54 where yellow boxes mean that the user can set voltage or current values, depending on the case, green boxes display the current value settled by the yellow boxes, red and light blue boxes monitoring the values for the voltage and current applied to the ion source. As a safety procedure, the value of the current rises up in steps of 1A per 10 seconds.

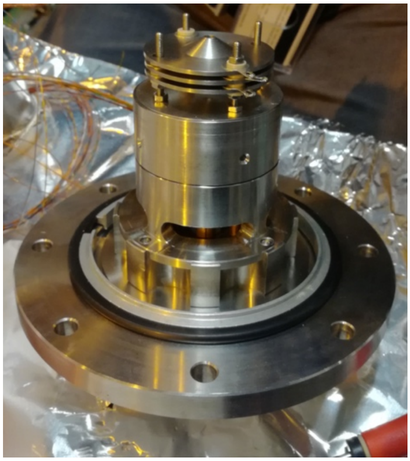

Figure 53. Picture of the WISArD offline source

Figure 54 shows the user interface (touch panel) to control the voltages in the offline ion source. A secondary display is shown in figure 55 used only administrator to configure voltage and current settings.

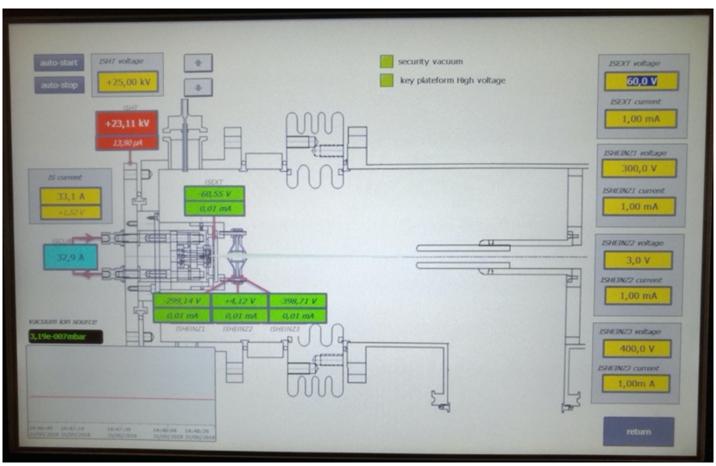

Figure 54. Touch panel used to set voltage in the different electrodes in the offline ion source.

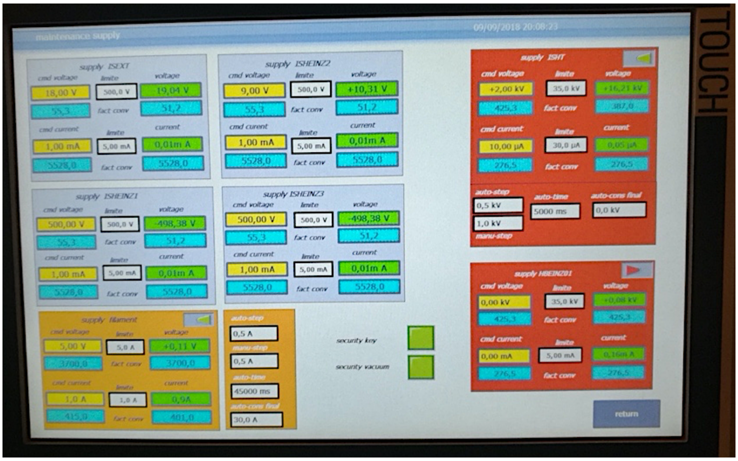

Figure 55. Secondary display of the touch panel (SIMATIC HMI) use to set high voltage values in the offline ion source.

c. Data Acquisition system: FASTER

FASTER is a tailored modular digital acquisition system. For the WISArD campaign in November 2018, two four-channel ADC modules, for the MOSAHR board were used to digitize and record proton events. Also, a 2-channel QDC-TDC module, compatible with the CARAS boards was used to measure the incident beta particles on the plastic scintillator. Figure 56 shows the final configuration for data acquisition, in the upper right part the modules CARAS and MOSAHR.

Figure 56. FASTER Acquisition system and high voltage power supply used in the ^{32}Ar campaing.

The values used for the beta detector (plastic scintillator) were set and tailored according to the online analysis performed during the ^{32}Ar beamtime. Figure 57 shows the values used in the different parameters for the QCD-TDC module. The first parameter is the Low Pass filter which was set ON with the maximum rise time (57ns) because the registered signal was found to be slow and noisy. The BLR is the time needed to have the base line back at "nominal" value (gate at 1200ns).

The trigger value is set to the minimum value (1mV) since the counting rate is low. The QDC option Qx3 define 3 different time windows for the charge integration in the beta detector. The first window, QD1, (from -10 ns to 250 ns,) set an optimal time windows to integrate the superallowed Fermi transition proton peak. The purpose of the second time window, QD2, is to integrate the fast signals that appear at the beginning of the first-time windows (from -10ns to 50ns). The last time window, QD3 integrates the full-time window signal (from -10 ns to 1200 ns), this window works as a trigger to avoid possible pile-up effect.

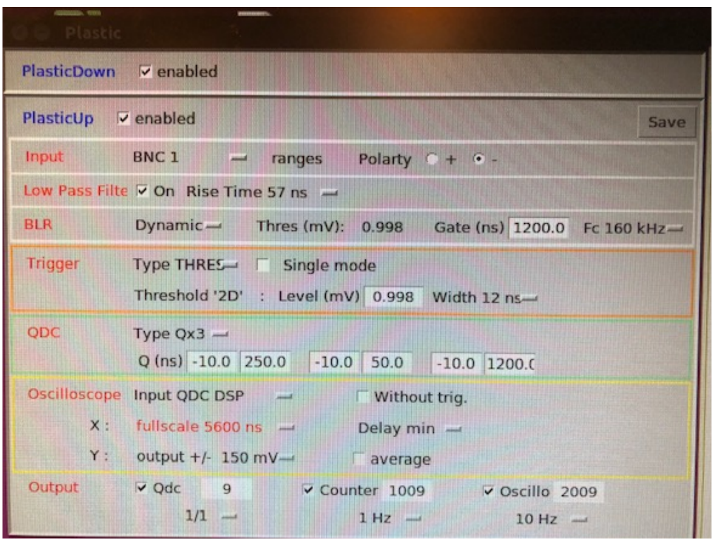

Figure 57. FASTER graphical user interface. QCD values set for the ^{32}Ar campaing.

Appendix C

Information of the collected data of ^{32}Ar campaign (November 2018, ISOLDE/CERN).

Table 15. Detailed description of the RUN files collected during the ^{32}Ar campaign. Highlighted cells were contemplated for the ^{32}Ar data analysis.

RUN name	Acquisition time (start)	Acquisition time (end)	Isotope	B Field [T]	Proton current [uA]	ID elog	Comments
	November 8th, 2018						
1	22:11	22:30	^{208}Po			99	Energy calibration with alpha source
	November 9th, 2018						
2	00:34	00:53	^{33}Ar	4		101	
3	1:13	2:38		4		103	
4	2:39	3:14		4		104	
5	3:22	4:36	^{32}Ar	4	1.49	106	
6	4:48	5:04		4		107	Stop the DAQ, protons have gone
7	5:21	6:07		4	1.08	109	
9	18:54	21:54		4	1.5	113	
10	21:58	22:19		4	2	115	

To be continued…

Continuation…

Table 15. Detailed description of the RUN files collected during the ^{32}Ar campaign.

RUN name	Acquisition time (start)	Acquisition time (end)	Isotope	B Field [T]	Proton current [uA]	ID elog	Comments
	November 9th, 2018						
11	22:27	2:48	^{32}Ar	4	1	116	
	November 10th, 2018						
12	3:04	4:00	^{32}Ar	4	1	117	
13	4:26	6:05			1	118	
14	6:10	8:01	^{32}Ar	4	1	120-121	Test to investigate satellite peak. Mylar foil is out of position
15	13:26	20:44	^{32}Ar		1.5	123	
16	20:53	21:56	--	4	1.5	126	
17	23:50	00:50	^{32}Ar	4	1.9	127	
	November 11th, 2018						
18	1:21	8:10	^{32}Ar	4	1.68		
19	10:00	11:36	^{32}Ar	4	1		
20			*CaO target broke! no more data!!*				

Appendix D

Extension of the data analysis for proton lines following a Gamow-Teller transition during the ^{32}Ar campaign (ISOLDE 2018).

Singles: proton spectrum

a. Down Plate: SiD

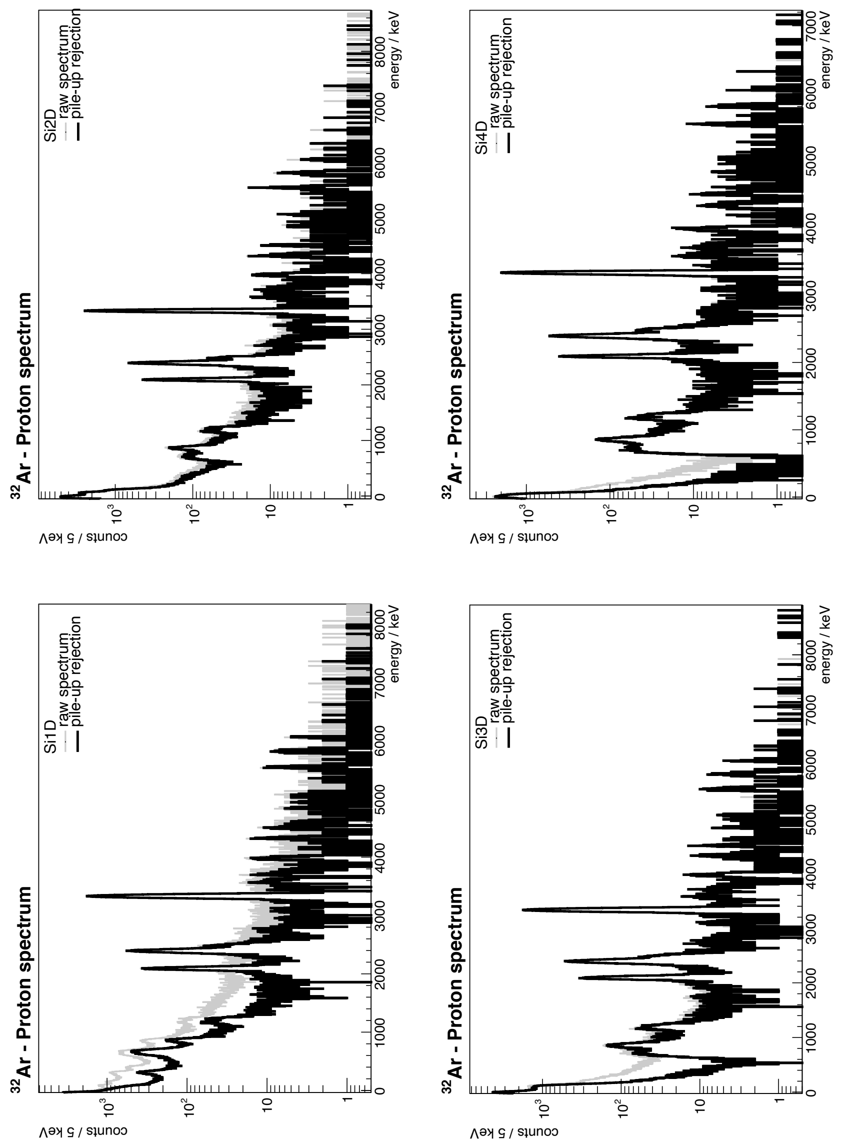

Figure 58. Each histogram contains the sum overall the RUN files (full statistics, see table 15 in Appendix C) collected during the ^{32}Ar beamtime. The pile-up rejection (black line) compared to the raw data (gray line) is presented in the low proton energy region for all detectors, without affecting the 3356keV proton line following by the superallowed Fermi transition.. For each detector, the pile-up effect is subtracted.

b. Upper Plate: SiU

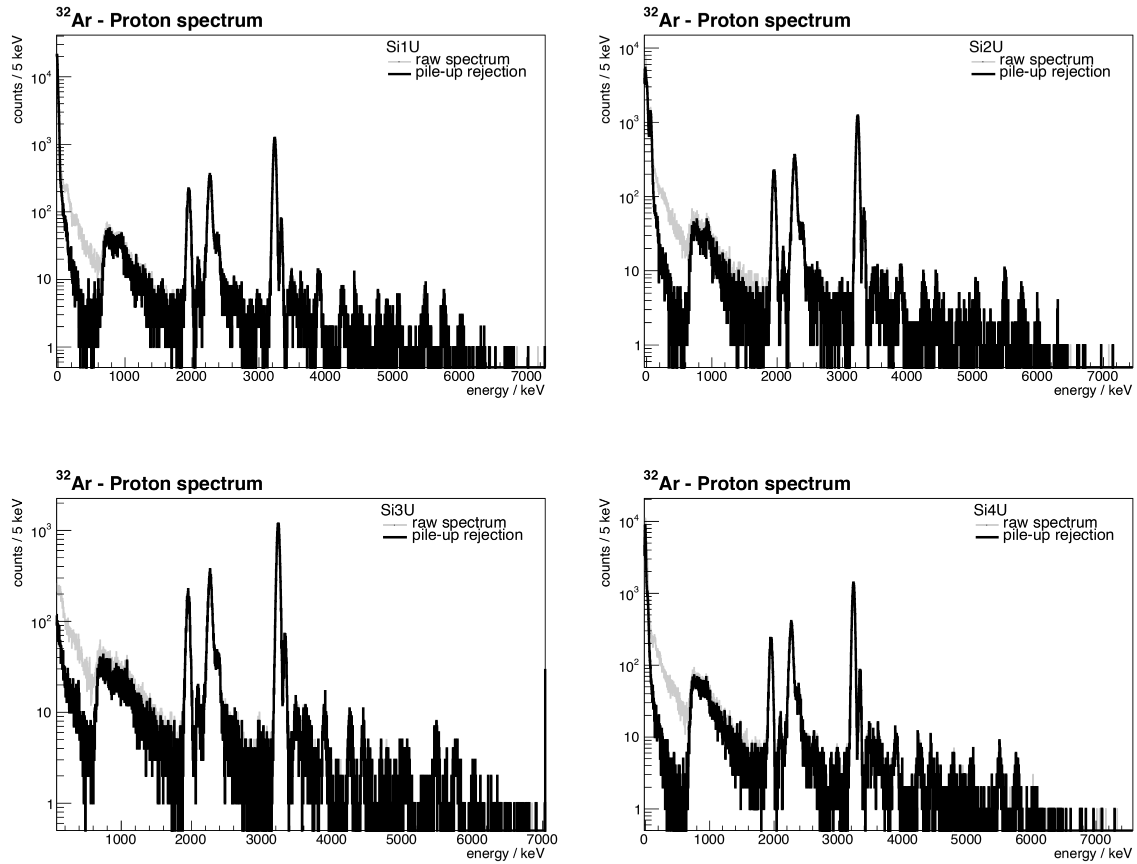

Figure 59. Four proton silicon detectors located in the upper plate. Comparison between the raw spectra (gray line) collected during the ^{32}Ar campaing and the pile-up rejection (black line). All spectra contain the full statistics of the RUN-files.

Coincidences: beta-proton spectrum

In figure 60(a),(b) shows the selection in the time window (vertical dotted lines) in red the superallowed Fermi beta transition and black the 2121 keV proton line. (horizontal dotted lines) Cuts on the proton energy of interest, in this case 2121 keV and 3356 keV proton lines. The subfigures (b) and (d). Figures 60(b), (d) are the resulting 2121 keV proton energy line for singles and coincidences. The proton energy shifts of ~4 keV coincidence towards higher values are clearly observed for SiD. Opposite to the previous case, the energy shift of coincidence moves towards the lower proton energy values for the silicon detectors located in the upper plate, SiU.

a. Down Plate: SiD

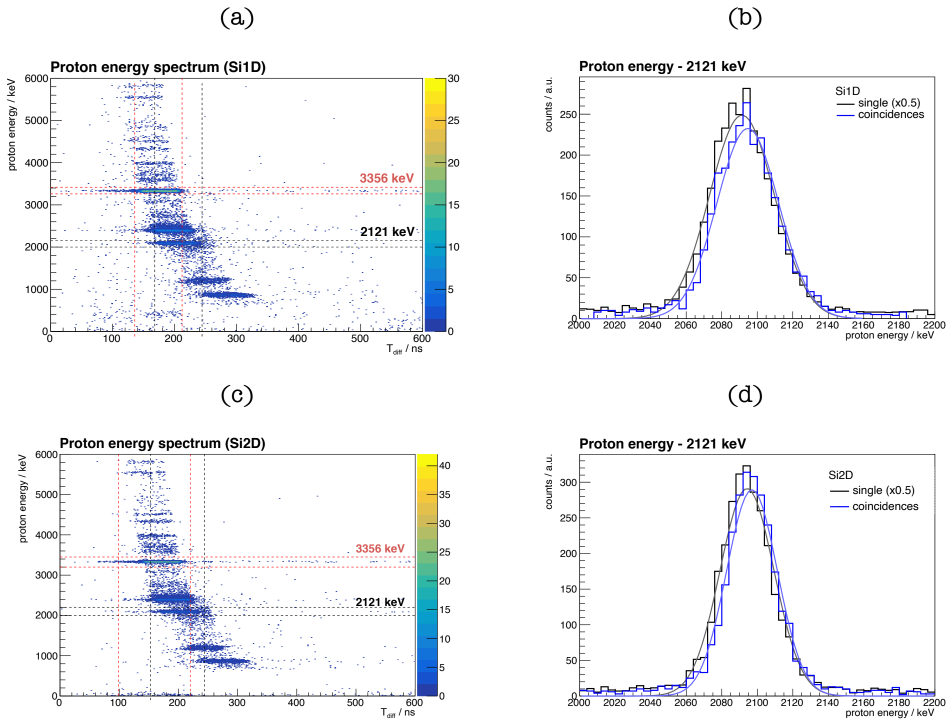

Figure 60. Time window and proton energy cuts used to create the β-p coincidence spectrum for the 2121 keV and 3356 keV proton energy. (b), (d) Proton energy shift for detector Si1D and Si2D, a energy shift (4 keV average) toward high energy is clearly visible.

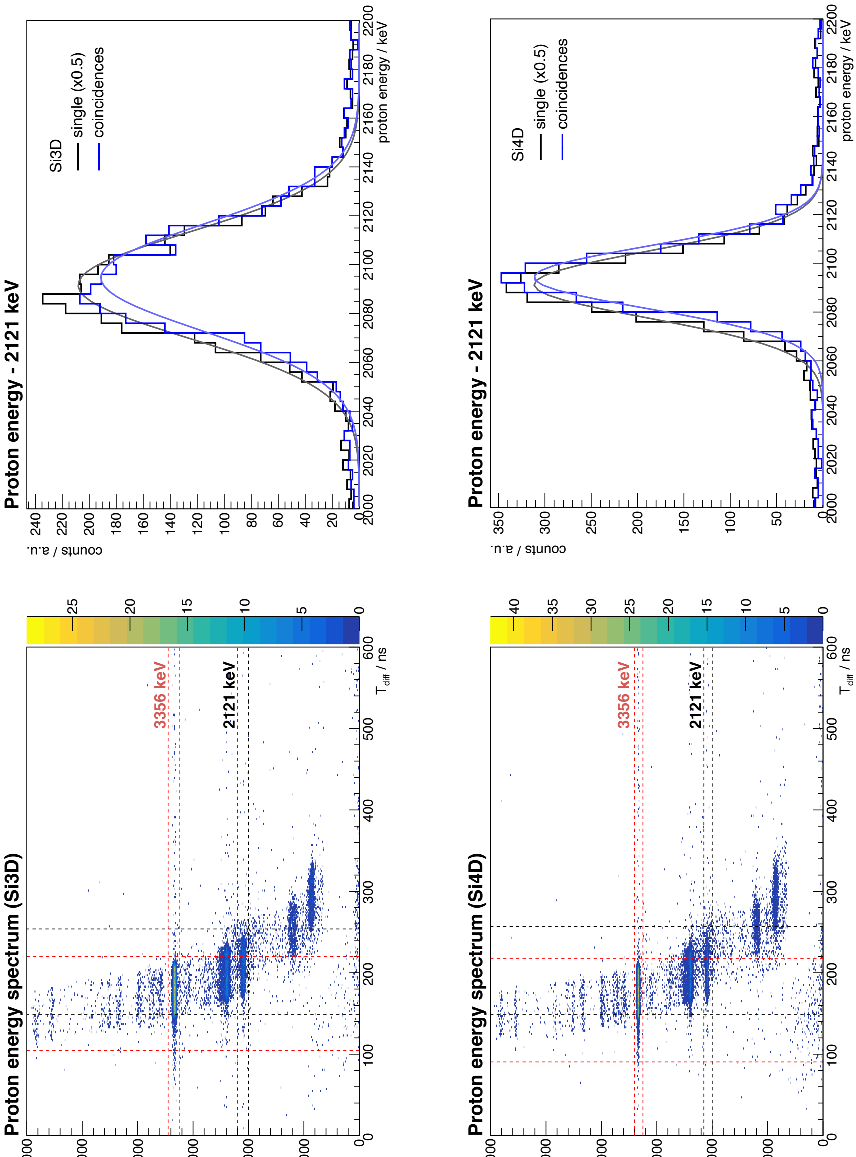

Figure 61. Time window and proton energy cuts used to create the β -p coincidence spectrum for the 2121 keV and 3356 keV proton energy. (b), (d) Proton energy shift for detector Si3D and Si4D, respectively, a shift in the proton energy (4 keV average) toward high energy is clearly visible

a. Upper Plate: SiU

Similarly, to the SiD. Time window and proton energy cuts are performed to the SiU detectors. The expected proton energy shift towards lower energy is clearly visible.

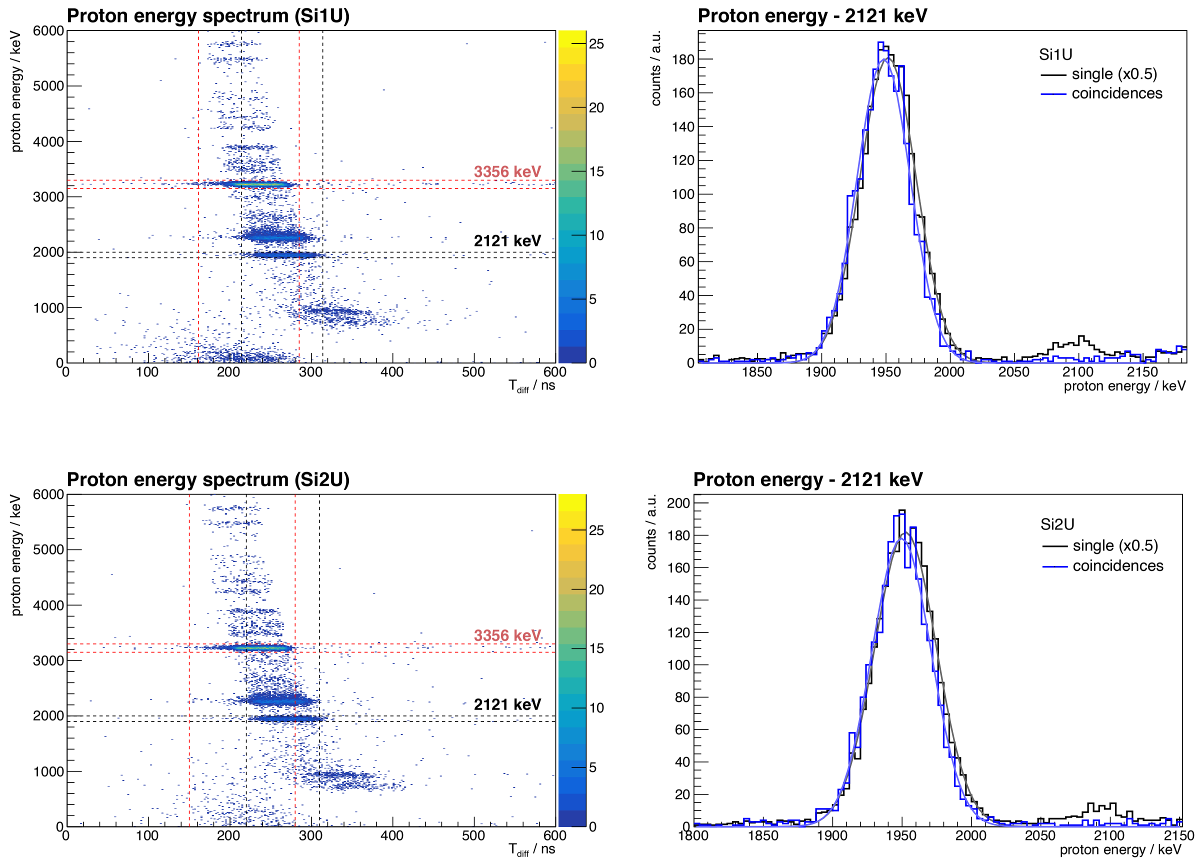

Figure 62. Time window and proton energy cuts used to create the β -p coincidence spectrum for the 2121 keV and 3356 keV proton energy. (b), (d) Proton energy shift for detector Si1U and Si2U, respectively, a shift in the proton energy (4 keV average) toward lower energy is clearly visible

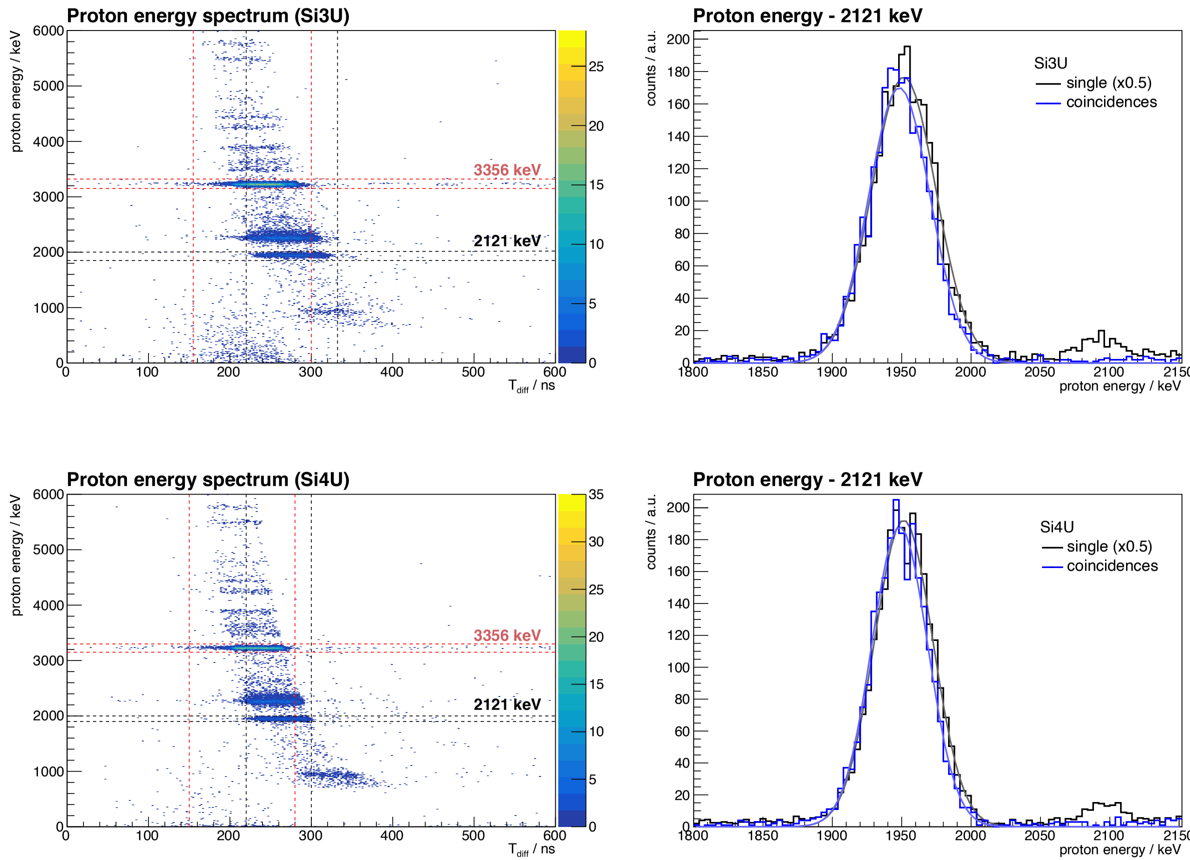

Figure 63. Time window and proton energy cuts used to create the β -p coincidence spectrum for the 2121 keV and 3356 keV proton energy. (b), (d) Proton energy shift for detector Si3U and Si4U, respectively, a shift in the proton energy (4 keV average) toward low energy is clearly visible

b. $a_{\beta\nu}$ vs E_p (extended version)

The following section include the $\boldsymbol{a_{\beta\nu}}$ plotted as function of the simulated proton energy shifts using the proton energies, E_p, (from literature) 2421 keV, 3988 keV, 5555 keV, and 5832 keV proton lines following a GT transition. Figure 64 shows the linear dependency between the $\beta - \nu$ angular correlation value and the proton energy shift values obtained via Monte Carlo simulations, allowing only right-handed neutrinos ($b_{Fierz} = 0$).

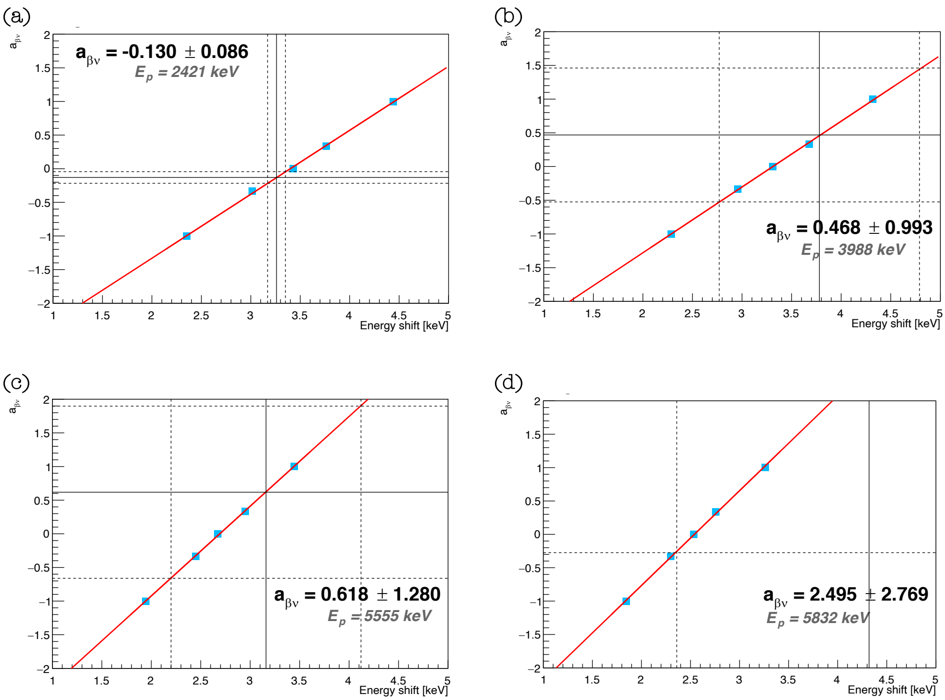

Figure 64. Proton energy shift with respect to the β–ν angular correlation value for the (a) 2421 keV, (b) 3988 keV, (c) 5555 keV, and (d) 5832 keV protons following a Gamow-Teller transition. Solid black lines: (vertical) experimental energy shift and (horizontal) $a_{\beta\nu}$ value. The dashed horizontal and vertical lines are uncertainties related to the linear fit and the experimental energy shift, respectively.

The values obtained for $a_{\beta\nu}$ respect the expected kinematic energy shift for each proton line studied here is presented in Table 8 (see chapter 6). From these results, it is clear that the sensitivity in the $a_{\beta\nu}$ measurement get compromised as the proton energy increased. However, the 2421 keV proton line might achieve a better result by increasing statistics and a fine tune in the fitting analysis hence the proximity of the 2510 keV proton line compromise the extraction of the mean value (centroid) using a Gaussian function.

Table 16. Angular correlation coefficients for the analyzed proton lines. In bold, the best values for the proton lines following a GT and F beta transition, respectively. (see chapter 6)

Proton energy E_p[keV]	kinematic energy shift (simulation)[keV]	$da_{\beta\nu}/dE_s$	$\tilde{a}_{\beta\nu}$
2121.7(31)	2.96 ± 0.07	0.936	-0.338 ± 0.066
2421.8(29)	3.26 ± 0.09	0.959	-0.130 ± 0.086
3356.0(7)	4.51 ± 0.04	0.912	1.000 ± 0.037
3988.6(36)	3.78 ± 1.01	0.983	0.468 ± 0.993
5555.5(45)	3.16 ± 0.96	1.333	0.618 ± 1.280
5832.1(53)	4.32 ± 1.96	1.413	2.495 ± 2.769

In Table 17 the FWHM-values of the 2121 keV and 3356 keV proton peaks are presented. The values were obtained from the fitting analysis (Gaussian fit) using singles histograms for each detector per proton peak.

Table 17. FWHM-values obtained for the 2121keV and 3356 keV proton lines per detector.

Proton detector	FWHM [keV] EP=2121.7(31)	FWHM [keV] EP=3356.0(7)
Si1U	56.80±0.55	48.67±0.24
Si2U	58.74±0.43	51.30±0.25
Si3U	65.20±0.66	57.25±0.29
Si4U	44.90±0.42	37.90±0.19
Si1D	37.98±0.72	37.12±0.19
Si2D	32.60±0.71	28.12±0.13
Si3D	46.03±0.83	39.81±0.20
Si4D	29.71±0.54	27.48±0.13

Systematic uncertainties for proton lines following a GT transition

To determine the sensitivity to the change in the angular distribution between the leptons emitted in the ^{32}Ar beta decay for each of the possible sources of systematic uncertainty, several Monte Carlo simulations (GEANT4) are analyzed by modifying one of these parameters at a time.

The general procedure is to modify the original value in the Monte Carlo simulation (the one that resembles the experimental conditions) by adding/subtracting the error value quoted to the associated uncertainty source. Once the parameter to be analyzed is fixed, GEANT4 simulations of $3x10^6$ events are used to determine the shift in kinematic proton energy between single events and in coincidence with the beta particle. Therefore, the weighted average value of the kinematic energy shift (E_p) can be determined. This procedure is repeated several times, always changing each time the uncertainty by a χ −value. Roughly speaking, by varying x-times the value of a variable τ (where τ could be any possible source of systematic uncertainty), the proton energy shift gets affected, these changes describe the sensitivity on $dE_p/d\tau$. A second part of the analysis has to be done in order to translate the $dE_p/d\tau$ into the sensitivity in terms of the angular correlation distribution ($a_{\beta\nu}$).

Monte Carlo simulations were performed to study the kinematic energy shift of the proton energy by changing the angular distribution between the leptons emitted in the ^{32}Ar decay, i.e., $da_{\beta\nu}/dE_p$. Both behaviors, $dE_p/d\tau$ and $da_{\beta\nu}/dE_p$, were found to be linear, by using the slope of each, the sensitivity of the angular correlation with respect to the uncertainty source can be determined, i.e., $da_{\beta\nu}/d\tau$. Table 18 summarizes the sources of systematic errors (τ) introduced during the experiment. In the following subsections, 2121 keV and 5555 keV proton lines are presented.

The discussion related to the values obtained to the uncertainty of the 2121 keV proton energy is discussed in the text (chapter 6.3), only the graphical visualization of the percentages obtained for each of the systemic uncertainties is presented here, see figure 64.

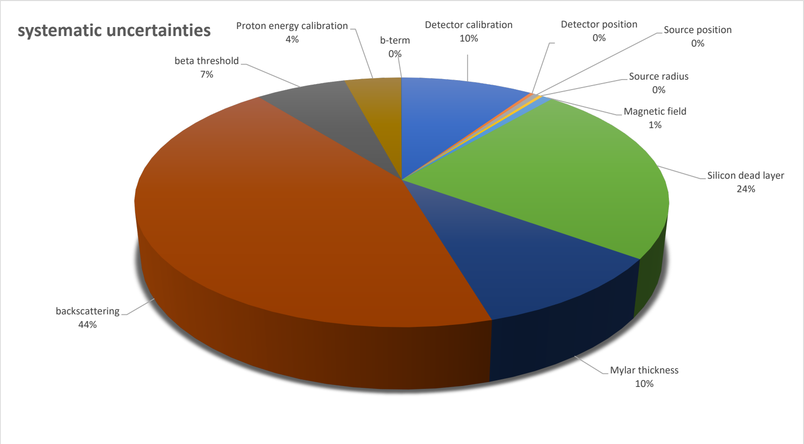

Figure 65. The pie chart summarizes the results obtained by the uncertainty analysis for the 2121 keV proton energy following a Gamow-Teller transition.

Even though the proton lines following a GT transition specifically the one at 5555 keV does not compete with quoted values for tensor current contributions, their study is still useful in order to find trends in our data. Table 18 shows the values founded for the dominant sources of uncertainty for the 2121 keV and 5555 keV proton peaks.

Table 18. Sources of systematic uncertainties. The values presented were determined for the 5555 keV proton line.

Dominant source of uncertainties, τ.	Uncertainty , χ	$da_{\beta\nu}/d\tau$ [$\delta\tilde{a}$(x10-3)]	
		2121 keV	5555 keV
False coincidence	0.3%	2	<1
Linear slope uncertainty	0.3%	6	3
Proton energy from literature	1 keV	2.59	1.68
dead layer thickness	120 nm	15	22.5
Mylar thickness	700 nm	6.60	10.56
β backscattering	15%	27.8	8.75
β energy threshold	12 keV	8.2	22.2
Detector position	1 mm	0.186	0.03
Source position	1 mm	0.278	0.02

Source radius	1 mm	4.14	2.33
Magnetic field	1%	2.59	3.2
Fierz interference term, b_F	0.1%	0.0283	0.027
TOTAL		33	34

The proof-of-principle experiment based on proton-positron coincidences that was reported here led to a final value on the angular correlation coefficient for the protons at 2121 keV following a GT transition

$$\tilde{a}_{GT} = -0.338 \pm 0.066_{stat} \pm 0.033_{sys}$$

The latter value is found to be in agreement with the SM predictions with a 0.07σ-deviation by considering only statistical errors. For sake of completeness the angular correlation coefficient for the protons at 5555 keV following a GT transition is presented:

$$\tilde{a}_{GT} = 0.618 \pm 1.280_{stat} \pm 0.034_{sys}$$

Bibliography

[1] M. González-Alonso, O. Naviliat-Cuncic, and N. Severijns, “New physics searches in nuclear and neutron β decay,” *Prog. Part. Nucl. Phys.*, vol. 104, pp. 165–223, 2019.

[2] T. D. Lee and C. N. Yang, “Question of Parity Conservation in Weak Interactions,” *Phys. Rev.*, vol. 104, no. 1, pp. 254–258, 1956.

[3] E. Wursten, “Searching for Exotic Weak Currents with the WITCH Experiment,” 2013.

[4] C. S. Wu, E. Ambler, R. W. Hayward, D. D. Hoppes, and R. P. Hudson, “Experimental test of parity conservation in beta decay,” *Phys. Rev.*, vol. 105, no. 4, pp. 1413–1415, 1957.

[5] H. J. Andrä, “Precision experiments using fast beam laser interaction,” in *Nuclear Instruments and Methods In Physics Research*, 1982, vol. 202, no. 1–2, pp. 123–137.

[6] S. L. Glashow, “Partial-symmetries of weak interactions,” *Nucl. Phys.*, 1961.

[7] A. Salam and J. C. Ward, “Electromagnetic and weak interactions,” *Phys. Lett.*, vol. 13, no. 2, pp. 168–171, 1964.

[8] S. Weinberg, “A model of leptons,” *Phys. Rev. Lett.*, vol. 19, no. 21, pp. 1264–1266, 1967.

[9] N. Severijns, M. Beck, and O. Naviliat-Cuncic, “Tests of the standard electroweak model in nuclear beta decay,” *Rev. Mod. Phys.*, vol. 78, no. 3, pp. 991–1040, 2006.

[10] S. Weinberg, “Effective gauge theories,” *Phys. Lett. B*, vol. 91, no. 1, pp. 51–55, 1980.

[11] P. Herczeg, “Beta decay beyond the standard model,” *Prog. Part. Nucl. Phys.*, vol. 46, no. 2, pp. 413–457, 2001.

[12] A. Falkowski, M. González-Alonso, and O. Naviliat-Cuncic, “Comprehensive analysis of beta decays within and beyond the Standard Model,” *arXiv:2010.13797v2 [hep-ph]*, 2020.

[13] M. González-Alonso and J. Martin Camalich, “Isospin breaking in the nucleon mass and the sensitivity of β decays to new physics,” *Phys. Rev. Lett.*, vol. 112, no. 4, pp. 1–6, 2014.

[14] M. González-Alonso and J. M. Camalich, “Global effective-field-theory analysis of new-physics effects in (semi)leptonic kaon decays,” *J. High Energy Phys.*, vol. 2016, no. 12, 2016.

[15] V. Cirigliano, J. P. Jenkins, and M. González-Alonso, “Semileptonic decays of light quarks beyond the Standard Model,” *Nucl. Phys. B*, vol. 830, pp.

95–115, 2010.

[16] V. Cirigliano, S. Gardner, and B. R. Holstein, “Beta decays and non-standard interactions in the LHC era,” *Prog. Part. Nucl. Phys.*, vol. 71, pp. 93–118, 2013.

[17] J. D. Jackson, S. B. Treiman, and H. W. Wyld, “Coulomb corrections in allowed beta transitions,” *Nucl. Phys.*, vol. 4, no. C, pp. 206–212, 1957.

[18] T. Bhattacharya *et al.*, “Probing novel scalar and tensor interactions from (ultra)cold neutrons to the LHC,” *Phys. Rev. D - Part. Fields, Gravit. Cosmol.*, vol. 85, no. 5, pp. 1–29, 2012.

[19] M. González-Alonso and O. Naviliat-Cuncic, “Kinematic sensitivity to the Fierz term of β -decay differential spectra,” *Phys. Rev. C*, vol. 94, no. 3, p. 035503, Sep. 2016.

[20] V. Cirigliano, A. Garcia, D. Gazit, O. Naviliat-Cuncic, G. Savard, and A. Young, “Precision beta decay as a probe of new physics,” *arXiv*, pp. 1–11, 2019.

[21] C. H. Johnson, F. Pleasonton, and T. A. Carlson, “Precision measurement of the recoil energy spectrum from the decay of 6He,” *Phys. Rev.*, vol. 132, no. 3, pp. 1149–1165, 1963.

[22] J. S. Allen, R. L. Burman, W. B. Herrmannsfeldt, P. Stähelin, and T. H. Braid, “Determination of the beta-decay interaction from electron-neutrino angular correlation measurements,” *Phys. Rev.*, vol. 116, no. 1, pp. 134–143, 1959.

[23] T. Eronen, A. Kankainen, and J. Äystö, “Ion traps in nuclear physics—Recent results and achievements,” *Prog. Part. Nucl. Phys.*, vol. 91, pp. 259–293, 2016.

[24] N. D. Scielzo *et al.*, “Detecting shake-off electron-ion coincidences to measure β-decay correlations in laser trapped 21Na,” *Nucl. Phys. A*, vol. 746, no. 1-4 SPEC.ISS., pp. 677–680, 2004.

[25] P. A. Vetter, J. R. Abo-Shaeer, S. J. Freedman, and R. Maruyama, “Measurement of the β-ν correlation of 21Na using shakeoff electrons,” *Phys. Rev. C - Nucl. Phys.*, vol. 77, no. 3, p. 35502, 2008.

[26] X. Fléchard *et al.*, “Measurement of the β-ν Correlation coefficient a βν in the β decay of trapped 6He+ ions,” *J. Phys. G Nucl. Part. Phys.*, vol. 38, no. 5, 2011.

[27] A. Gorelov *et al.*, “Scalar interaction limits from the β-ν correlation of trapped radioactive atoms,” *Phys. Rev. Lett.*, vol. 94, no. 14, 2005.

[28] P. Finlay *et al.*, “First high-statistics and high-resolution recoil-ion data from the WITCH retardation spectrometer,” *Eur. Phys. J. A*, vol. 52, no. 7, 2016.

[29] E. K. Warburton, D. E. Alburger, and D. H. Wilkinson, “Electron-neutrino correlation in the first-forbidden beta decay of 11Be,” *Phys. Rev. C*, vol. 26, no. 3, pp. 1186–1197, 1982.

[30] V. Egorov *et al.*, “Beta-neutrino angular correlation in the decay of 18Ne,” *Nucl. Phys. A*, vol. 621, no. 3, pp. 745–753, 1997.

[31] E. T. H. Clifford *et al.*, “Kinematic shifts in the β-delayed particle decay of Na20, and the β-ν angular correlation,” *Phys. Rev. Lett.*, vol. 50, no. 1, pp. 23–26, 1983.

[32] D. Schardt and K. Riisager, “Beta-neutrino recoil broadening in β-delayed proton emission of 32Ar and 33Ar,” *Zeitschrift für Phys. A Hadron. Nucl.*, vol. 345, no. 3, pp. 265–271, 1993.

[33] E. G. Adelberger *et al.*, “Positron-neutrino correlation in the 0+ → 0+ decay of 32Ar,” *Phys. Rev. Lett.*, vol. 83, no. 7, pp. 1299–1302, Aug. 1999.

[34] K. Blaum *et al.*, “Masses of 32Ar and 33Ar for fundamental tests,” *Phys. Rev. Lett.*, vol. 91, no. 26, 2003.

[35] V. Vorobel *et al.*, “Beta-neutrino angular correlation in the decay of 14O : Scalar coupling and interatomic interaction,” *Eur. Phys. J. A*, vol. 16, no. 1, pp. 139–147, 2003.

[36] M. G. Sternberg *et al.*, “Limit on Tensor Currents from 8Li β Decay,” *Phys. Rev. Lett.*, vol. 115, no. 18, pp. 1–6, 2015.

[37] V. Araujo-Escalona *et al.*, “WISARD: Weak-interaction studies with 32 Ar decay (LOI),” *CERN-INTC-2016-050/INTC-I-172*, 2016.

[38] N. Severijns and B. Blank, “Weak interaction physics at ISOLDE,” *J. Phys. G Nucl. Part. Phys.*, vol. 44, no. 7, p. 074002, Jul. 2017.

[39] A. Behr and A. Gorelov, “β-decay angular correlations with neutral atom traps,” *J. Phys. G Nucl. Part. Phys.*, vol. 41, no. 11, 2014.

[40] A. Leredde *et al.*, “Laser trapped 6He as a probe of the weak interaction and a test of the sudden approximation,” *J. Phys. Conf. Ser.*, vol. 635, no. 5, pp. 2–3, 2015.

[41] I. Mukul *et al.*, “A new scheme to measure the electron-neutrino correlation - The case of 6He,” *arXiv:1711.08299v1 [nucl-ex]*, 2017.

[42] M. T. Burkey *et al.*, “Precision $\beta - \nu$ correlation measurements with the Beta-decay Paul Trap,” *Hyperfine Interact.*, vol. 240, no. 1, 2019.

[43] E. Liénard *et al.*, “Precision measurements with LPCTrap at GANIL,” *Hyperfine Interact.*, vol. 236, no. 1–3, pp. 1–7, 2015.

[44] P. D. Shidling, V. S. Kolhinen, B. Schroeder, N. Morgan, A. Ozmetin, and D. Melconian, “TAMUTRAP facility: Penning trap facility for weak interaction studies,” *Hyperfine Interact.*, vol. 240, no. 1, pp. 1–10, 2019.

[45] B. Fenker *et al.*, “Precision Measurement of the β Asymmetry in Spin-Polarized 37K Decay,” *Phys. Rev. Lett.*, 2018.

[46] I. Mardor *et al.*, “The Soreq Applied Research Accelerator Facility (SARAF): Overview, research programs and future plans,” *Eur. Phys. J. A*, vol. 54, no. 5, 2018.

[47] A. S. Carnoy, J. Deutsch, T. A. Girard, and R. Prieels, “Limits on nonstandard weak currents from the polarization of 14O and 10C decay positrons,” *Phys. Rev. C*, vol. 43, no. 6, pp. 2825–2834, 1991.

[48] O. Naviliat-Cuncic and M. González-Alonso, “Prospects for precision measurements in nuclear β decay in the LHC era,” *Ann. Phys.*, vol. 525, no. 8–9, pp. 600–619, 2013.

[49] E. G. Adelberger *et al.*, “Positron-neutrino correlation in the 0+ → 0+ decay of 32Ar (erratum),” *Phys. Rev. Lett.*, vol. 83, no. 15, p. 3101, 1999.

[50] B. Blank *et al.*, “Detailed study of the decay of 32Ar,” *Eur. Phys. J. A*, vol. 57, no. 1, 2021.

[51] N. Adimi *et al.*, “Detailed β-decay study of 33Ar,” *Phys. Rev. C - Nucl. Phys.*, vol. 81, no. 2, p. 24311, 2010.

[52] S. Agostinelli *et al.*, “GEANT4 - A simulation toolkit,” *Nucl. Instruments Methods Phys. Res. Sect. A Accel. Spectrometers, Detect. Assoc. Equip.*, vol. 506, no. 3, pp. 250–303, 2003.

[53] M. Beck *et al.*, “WITCH: A recoil spectrometer for weak interaction and nuclear physics studies,” *Nucl. Instruments Methods Phys. Res. Sect. A Accel. Spectrometers, Detect. Assoc. Equip.*, vol. 503, no. 3, pp. 567–579, 2003.

[54] M. J. G. Borge and K. Blaum, “Focus on Exotic Beams at ISOLDE: A Laboratory Portrait,” *J. Phys. G Nucl. Part. Phys.*, vol. 45, no. 1, 2018.

[55] J. P. Ramos *et al.*, “Intense 31-35Ar beams produced with a nanostructured CaO target at ISOLDE,” *Nucl. Instruments Methods Phys. Res. Sect. B Beam Interact. with Mater. Atoms*, vol. 320, no. 2014, pp. 83–88, 2014.

[56] S. Coeck, “Search for non Standard Model physics in nuclear beta-decay with the WITCH experiment,” KU Leuven, 2007.

[57] (LPC/Caen), “Fast Acquisition System for Nuclear Research.” [Online]. Available: http://faster.in2p3.fr/.

[58] L. Moneta, I. Antcheva, and D. Gonzalez Maline, “Recent improvements of the ROOT fitting and minimization classes,” *PoS*, p. 075, 2008.

[59] M. J. Berger, J. S. Coursey, M. A. Zucker, and J. Chang, “ESTAR, PSTAR, and ASTAR: Computer Programs for Calculating Stopping-Power and Range Tables for Electrons, Protons, and Helium Ions (version 1.2.3),” *National Institute of Standards and Technology*, 2005. [Online]. Available:

http://www.nist.gov/pml/data/star/.

[60] L. Hayen, "CRADLE++," 2017. [Online]. Available: https://github.com/leenderthayen/CRADLE.

[61] V. Araujo-Escalona *et al.*, "Scalar current limit from the beta-neutrino correlation: The WISArD experiment," in *Journal of Physics: Conference Series*, 2019, vol. 1308, no. 1.

[62] J. C. Hardy and I. S. Towner, "Superallowed 0+→0+ nuclear β decays: 2014 critical survey, with precise results for Vud and CKM unitarity," *Phys. Rev. C - Nucl. Phys.*, vol. 91, no. 2, p. 025501, Feb. 2015.

FACULTY OF SCIENCE
DEPARTMENT OF PHYSICS AND ASTRONOMY
WEAK INTERACTIONS
Celestijnenlaan 200B
B-3001 Leuven
victoria.araujoescalona@kuleuven.be
https://fys.kuleuven.be/iks